Nano Research Energy

ISSN 2791-0091 CN 10-1944/O6
https://doi.org/10.26599/NRE.2026.9120268

Research Article

Symmetry-driven isotropic hydration suppresses degradation of anthraquinone positional isomers in aqueous organic flow batteries via dipole cancellation

Wentao Hao[1,3], Xiaoyu Zhi[1], Chunyan Zhang[2](✉), Guoying Zhang[1,3](✉)

[1] State Key Laboratory of Coal Conversion, Institute of Coal Chemistry Chinese Academy of Sciences, Taiyuan 030001, China

[2] School of Environmental and Engineering, Taiyuan University of Technology, Taiyuan 030001, China

[3] University of Chinese Academy of Sciences, Beijing 100049, China

Nano Research Energy, **Just Accepted Manuscript** • https://doi.org/10.26599/NRE.2026.9120268

https://www.sciopen.com/journal/2791-0091 on Sep. 4, 2026

Just Accepted

Table of contents

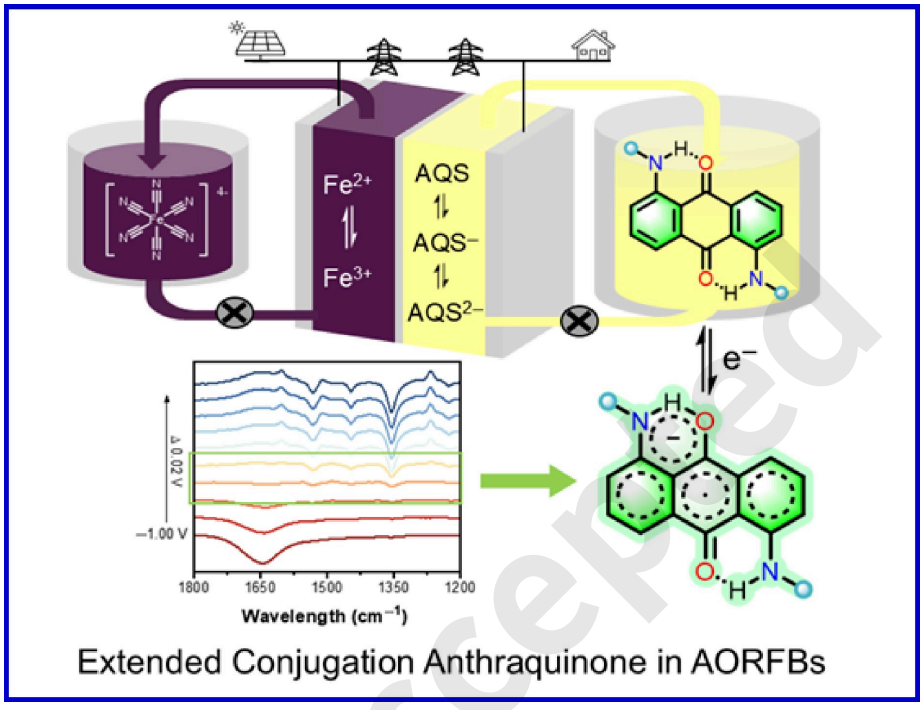

An anthraquinone architecture featuring extended polycyclic conjugation system delivers highly soluble, low-potential negolyte exhibiting excellent reversibility and exceptionally low-capacity decay rate in aqueous organic redox flow batteries.

Nano Research Energy

ISSN 2791-0091 (print); 2790-8119 (online)
https://doi.org/10.26599/NRE.2026.9120268

Research Article

Symmetry-driven isotropic hydration suppresses degradation of anthraquinone positional isomers in aqueous organic flow batteries via dipole cancellation

Wentao Hao[1,3], Xiaoyu Zhi[1], Chunyan Zhang[2] (✉), and Guoying Zhang[1,3] (✉)

[1] *State Key Laboratory of Coal Conversion, Institute of Coal Chemistry Chinese Academy of Sciences, Taiyuan 030001, China*
[2] *School of Environmental and Engineering, Taiyuan University of Technology, Taiyuan 030001, China*
[3] *University of Chinese Academy of Sciences, Beijing 100049, China*

Received: 15 June 2026 / **Revised:** 3 August 2026 / **Accepted:** 14 August 2026

ABSTRACT

Bimolecular degradation, *via* π-stacking, radical coupling, and desulfonation, severely limits the operational lifetime of anthraquinone-based anolytes in aqueous redox flow batteries. Molecular symmetry can promote protective, isotropic hydration around the electroactive core, yet this strategy remains underexplored. Herein, we establish a design principle: a symmetric, near-zero-dipole core nucleates a dense, uniformly bound hydration shell that sterically blocks bimolecular degradation. To test it, we synthesized anthraquinones with dipole moments from 25.4 to 0.0004 D. Only the perfectly symmetric 1,5-diaminoanthraquinone (**15AQS**) forms a complete, tightly packed hydration shell, stabilized by ~19 H-bonds per molecule, nearly double that of its analogue. Experimentally, **15AQS** shows outstanding stability: capacity fade is just 0.00018% per cycle, 100× lower than benchmark 1,4- 2,6- and 2,7-derivatives, and delivers a peak power density of 342 mW·cm^{-2} at 0.5 M. Multimodal characterization confirms the hydration shell immobilizes –NH protons and shields the electron-rich C3 site from dimerization. Collectively, this study establishes a predictive, computationally tractable design rule, from core symmetry to isotropic hydration and then to degradation blockade, for enhancing the intrinsic longevity of organic energy-storage molecules.

KEYWORDS

energy storage, aqueous organic redox flow batteries (AORFBs), anthraquinone, dipole cancellation, hydration structure

1 Introduction

Aqueous organic redox flow batteries (AORFBs) represent a promising platform for long-duration, grid-scale energy storage [1–3]. Among candidate anolytes, anthraquinone (AQ) derivatives are the most extensively studied class [4–7]. Although they exhibit reversible two-electron redox chemistry and synthetically tunable redox potentials, their practical utility is limited by progressive capacity decay under extended cycling [8–11]. Specifically, the primary degradation pathways, intermolecular π-stacking (leading to precipitation), irreversible coupling of semiquinone radicals, and gradual desulfonation, are chemically distinct but share a common mechanistic origin: all are bimolecular processes whose kinetics depend critically on local hydration structure, molecular collision geometry, and active-site accessibility [12–15].

Over the past decade, molecular design strategies for organic anolytes have focused almost exclusively on tuning redox potentials via electronic effects and enhancing aqueous solubility through the introduction of hydrophilic substituents [7, 16–20]. Although these efforts have substantially expanded the accessible chemical space, a critical structural dimension remains underexplored: the deliberate engineering of the interfacial hydration shell [21, 22]. Notably, each polar substituent appended to an AQ scaffold modulates the local hydration environment, including its density, spatial anisotropy, and hydrogen-bonding dynamics [23–27]. To date, however, the strategic design of this water layer as a physical barrier against bimolecular degradation pathways has not been systematically pursued. Therefore, engineering a hydration shell that fully encapsulates the aromatic core, rigidly immobilizes labile protons, and eliminates hydrophobic docking sites would, in principle, suppress the kinetics of major degradation pathways, irrespective of their thermodynamic driving forces [28]. We hypothesize that a molecular core exhibiting high symmetry and a near-zero dipole moment, when functionalized with symmetrically extended hydrophilic arms, will spontaneously nucleate an isotropic, tightly bound hydration shell. Furthermore, this dynamic chaperone physically shields the redox-active AQ framework from

Address correspondence to Chunyan Zhang, zhanggy527@163.com; Guoying Zhang, zhanggy@sxicc.ac.cn

bimolecular degradation pathways. To test this hypothesis, we introduced a library of four propyl sulfonate-functionalized AQs (Figs. 1(a) and 1(b)), in which the solubilizing propyl sulfonate chains are held constant while core symmetry is systematically varied: specifically, the 2,6-AQS and the 1,4- 1,5- and 2,7-isomers of the diamino anthraquinone series. Moreover, this controlled variation establishes a well-defined dipole-moment gradient, thereby coupling solvation-group contributions from intrinsic symmetry effects for the first time.

Herein, we present a complete prediction–validation –reverse-verification workflow. Specifically, density functional theory (DFT) and molecular dynamics (MD) simulations identify **15AQS** as the only isomer capable of forming a fully encapsulating hydration shell, approximately twice that of the 1,4- 2,6- and 2,7-isomers. Experimentally, **15AQS** achieves a capacity fade rate of 0.00018% per cycle in alkaline full-cell configurations, representing a two-order-of-magnitude improvement over the 1,4- 2,6- and 2,7-isomers, while delivering a peak power density of 342 mW·cm^{-2} at a 0.5 M electrolyte concentration. Furthermore, variable temperature NMR spectroscopy, operando UV–vis/EPR/IR measurements, and Fukui-function-guided analysis of trace degradation products collectively provide direct experimental evidence that the engineered hydration shell physically shields reactive sites from intermolecular degradation pathways. From this integrated dataset, we formulate a generalizable design strategy: from core symmetry to isotropic hydration, and thence to degradation blockade. Collectively, this principle enables computational prescreening and establishes a rational, longevity-by-design framework for next-generation organic energy-storage molecules.

2 Results and discussion

2.1 Molecular library design and hydration structure prediction

To systematically investigate how core symmetry governs hydration-shell architecture, we designed a four-compound library of AQs functionalized with identical propane-1-sulfonate arms (Fig. S1 in the Electronic Supplementary Material (ESM)).

The solubilizing chains are anchored *via* nitrogen linkages in four diamino-substituted isomers, namely, the **15AQS**, **14AQS**, **26AQS** and **27AQS**. This design establishes a dipole-moment gradient that is exclusively governed by core symmetry, while maintaining strict constancy in both the number and chemical identity of the hydrophilic substituents. DFT calculations reveal a pronounced variation in molecular dipole moments across the isomeric series (Figs. S2–S13 in the ESM) [29–33]. The asymmetric 1,4-isomer exhibits the largest dipole moment, whereas the 2,7- and 2,6-isomers display intermediate values of 9.0 and 5.9 D, respectively. In contrast, the highly symmetric 1,5-isomer achieves near-perfect cancellation of local bond dipoles, resulting in an exceptionally low dipole moment of only 0.003 D (Fig. 1(e)). Importantly, we explicitly distinguish gas-phase static dipole moments from solvated dipole moments derived from aqueous implicit-solvent simulations to eliminate conceptual ambiguity. Although solvated dipole moments in solution differ from static gas-phase values, the relative trend among these isomers is well preserved. Electrostatic potential (ESP) maps corroborate this trend: **15AQS** exhibits a nearly uniform surface charge distribution, while the other isomers feature clearly delineated electropositive and electronegative regions (Fig. 1(c)).

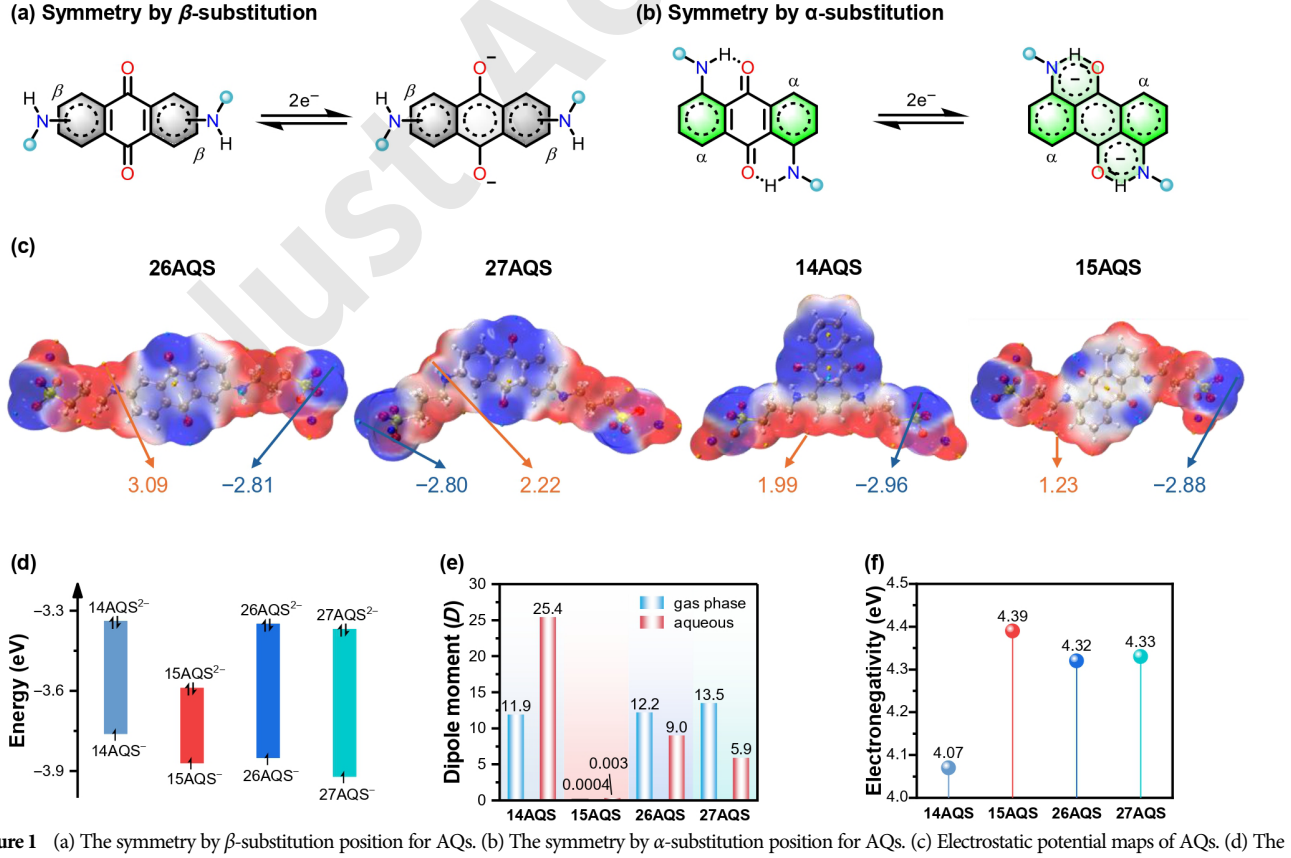

Figure 1 (a) The symmetry by *β*-substitution position for AQs. (b) The symmetry by *α*-substitution position for AQs. (c) Electrostatic potential maps of AQs. (d) The gap energy of SOMO and HOMO of AQs. (e) Dipole moment chart of AQs in the gas phase and aqueous solution. (f) Electronegativity graph of AQs.

Notably, for **15AQS**, ΔE_{2e} has been reduced to 0.28 eV, approximately half that of the others (Fig. 1(d)). Furthermore, computed electron affinities and electronegativities remain largely invariant across the series confirming that dipole magnitude, rather than redox or electronic character, is the dominant structural descriptor governing hydration-shell organization (Fig. 1(f)). Furthermore, the key quantum chemical parameters, including dipole moment, chemical hardness and softness, and electronegativity, were calculated for the **AQ**s (Table S1 in the ESM) [34]. Additionally, we hypothesized that the pronounced charge anisotropy across the isomeric series would critically govern the structural and energetic organization of the surrounding hydration shell. To test this, explicit-solvent MD simulations were conducted for the highly symmetric **15AQS** and extended the explicit-solvent MD simulations to other isomers (**14AQS**, **26AQS** and **27AQS**), with all results collected at a fixed AQs concentration of 0.5 M in 1 M NaOH aqueous solution (Fig. S14 in the ESM) [35]. As shown in Fig. 2, the results reveal a stark contrast in hydration behavior. **15AQS** induces a dense, spherically symmetric hydration layer that fully encapsulates the anthraquinone core, sustaining an average of 938 H-bonds (~19 hydrogen bonds per **15AQS** molecule) with water at a short, well-defined **15AQS**–water distance of 0.275 nm. Extending this comparison, **14AQS**—which exhibits the largest dipole moment among the four isomers—displays the most disrupted hydration shell, characterized by the fewest solute–water H-bonds and the longest average interaction distance. The other two isomers, **26AQS** and **27AQS**, whose dipole moment falls between those of **14AQS** and **15AQS**, exhibit similar hydration characteristics, with respective H-bond counts of 721 (~14 H-bonds per **26AQS** molecule) and 792 (~16 hydrogen bonds per **27AQS** molecule), reflecting their moderate molecular symmetry and dipole moments (Figs. 2(c) and 2(d), Figs. S15 and S16 in the ESM). Collectively, these simulations indicate that the near-zero dipole moment and high symmetry of **15AQS** encode a uniquely cohesive, isotropic water sheath, one that not only improves aqueous solubility but also creates a dynamic proton-conducting interface while sterically shielding the AQ core against bimolecular side reactions (Figs. 2(a) and 2(b)). These structure–hydration–function relationships are rigorously validated experimentally in subsequent sections.

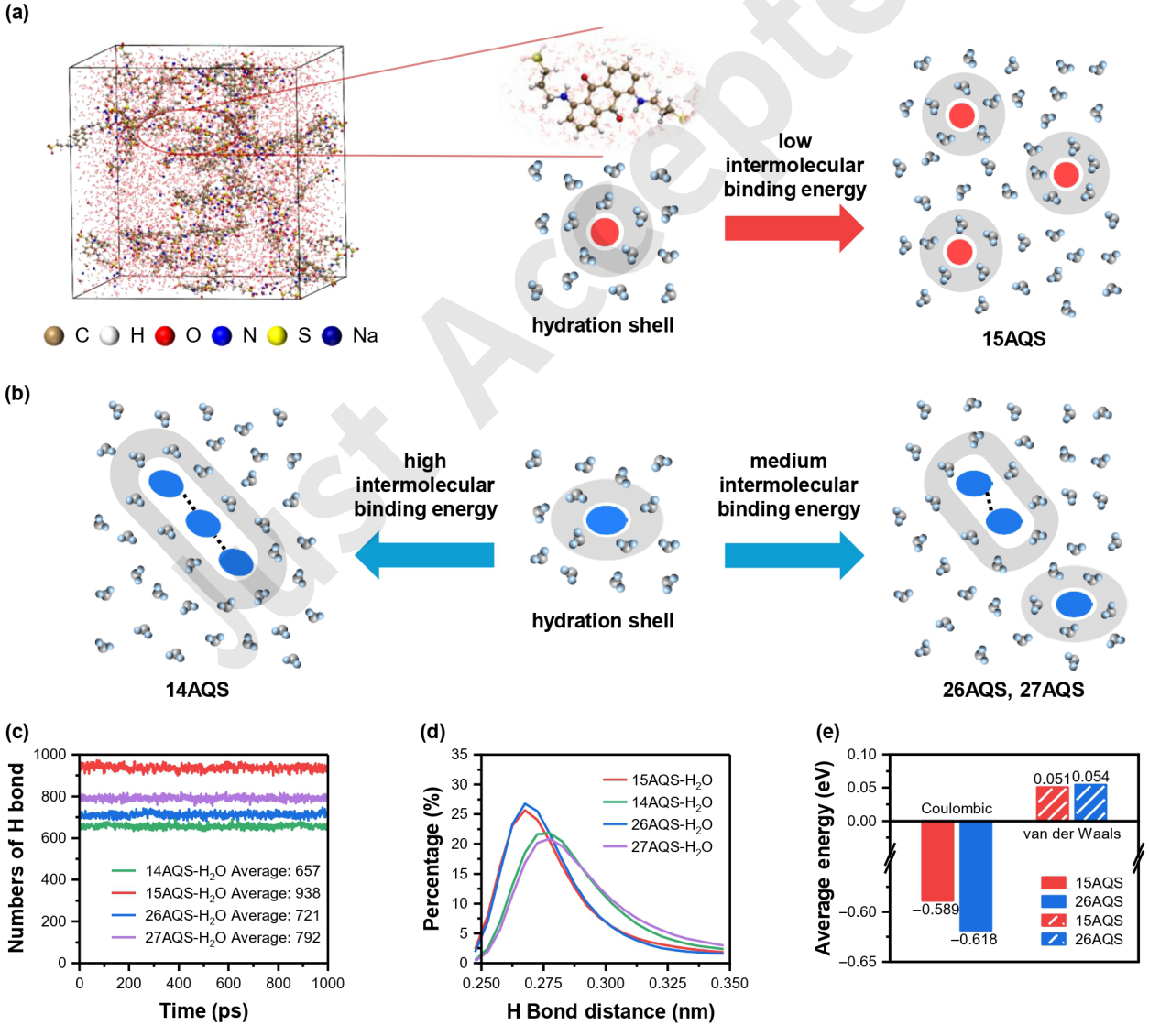

Figure 2 (a) MD simulation snapshots and the hydration schematic diagrams of 0.5 M 15AQS in H_2O. (b) The hydration schematic diagrams of 0.5 M 14AQS, 26AQS, 27AQS and in H_2O. The results of MD simulations include (c) the optimized number of H-bonding around AQs solvation structures, (d) the distribution of H-bonding distances, and (e) the intermolecular of AQs binding energy.

2.2 Synthesis and basic physicochemical properties

The target propyl sulfonate-functionalized AQs, namely **14AQS**, **15AQS**, **26AQS** and **27AQS**, were synthesized via nucleophilic substitution of the corresponding diamino-AQ precursors with 1,3-propanesultone. We further demonstrated kilogram-scale synthetic routes for the industrially promising molecules **15AQS** and **26AQS**. Synthetic efficiency varied significantly depending on the anchoring position: **26AQS** was isolated in moderate yield, whereas the amino-linked analogue **15AQS** was obtained in near-quantitative yield at the 1.03 kg scale. All compounds were rigorously characterized by NMR and HRMS (Figs. S17–S27 in the ESM). UV–vis spectroscopy of **15AQS** in aqueous solution reveals two characteristic absorption maxima at 350 and 550 nm; these bands remain invariant across pH 2–12, confirming the absence of acid–base equilibria, aggregation, or solvatochromic perturbations (Fig. 3(a), Fig. S28 in the ESM). Critically, **15AQS** achieves an exceptional aqueous solubility of 1.66 M, nearly double that of **26AQS**, and retains high solubility (0.99 M) even in 1 M NaOH (Figs. S29 and S30 in the ESM). Energy decomposition analysis further demonstrates that the enhanced hydration stability of **15AQS** arises predominantly from stronger electrostatic interactions, whereas Van der Waals force contributions are nearly identical (Fig. 2(e)). This marked solubility enhancement provides direct experimental validation of the MD-predicted role of the symmetric diamino core: its isotropic, tightly bound hydration shell effectively screens hydrophobic surface area and maximizes thermodynamic compatibility with water. Coupled with robust, scalable synthesis, these combined physicochemical advantages position **15AQS** as a uniquely suitable candidate for rigorous electrochemical characterization and functional evaluation in aqueous redox flow battery systems.

2.3 Electrochemical thermodynamics and pH-dependent behavior

Cyclic voltammetry of **15AQS** in aqueous solution shows a single, highly reversible two-electron redox wave at $E_{1/2}$ = −0.85 V, ~30 mV more negative than that of **26AQS**, consistent to the stronger conjugation effect resulting from the **15AQS**, where the amino groups are adjacent to the carbonyls and can form intramolecular hydrogen bonds (N–H···O=C), thereby making the reduction thermodynamically more difficult. In contrast, the **26AQS** exhibits a weaker conjugation effect due to the greater distance between the amino groups and the carbonyls (Fig. S31 in the ESM). The most significant electrochemical distinction lies in their pH-dependent redox behavior. **26AQS** follows classical Pourbaix behavior: its potential shifts linearly at −26 mV/pH below pKa_1 ≈ 12 and becomes pH-independent above this value (Fig. S32 in the ESM) [27, 36]. In contrast, **15AQS** exhibits a three-region Pourbaix diagram (Fig. 3(b), Fig. S33 in the ESM). Below pH 9, the slope is −62 mV/pH, characteristic of a concerted $2e^-/2H^+$ process. Between pH 9 and 12, the slope attenuates to −18 mV/pH, corresponding to less than one proton coupled with two-electron transfer. This behavior is attributed to intramolecular hydrogen bonding of **15AQS,** which interferes with proton transfer in the hydration. Above pH 12, the slope vanishes at 0 mV/pH, indicating electron transfer without proton involvement [25, 37, 38]. Similarly, the structural isomers **14AQS** and **27AQS** also display pH-dependent redox characteristics governed by sequential deprotonation of their reduced anthraquinone species. For **14AQS**, a single redox couple is observed across all measured pH conditions; its equilibrium potential linearly shifts negatively with a fitted apparent slope of −12 mV/pH in the moderate alkaline region (pH 6–13) (Fig. S34 in the ESM). This apparent slope deviates from the ideal process. Similar to **15AQS**, this phenomenon arises from intramolecular hydrogen bonding, which perturbs proton transfer dynamics during redox reactions and alters the effective stoichiometry of coupled proton transfer. When pH > 13, the reduced anthraquinone undergoes complete deprotonation, and the redox potential becomes pH-independent with a slope of 0 mV/pH. Distinctly, **27AQS** displays a single redox couple at pH > 13. Within this highly alkaline region, the reduced anthraquinone is fully deprotonated, and electron transfer proceeds without coupled proton participation, corresponding to a 0 mV/pH Pourbaix plateau. As pH decreases, the redox wave gradually splits into two separated redox couples in cyclic voltammetry (Fig. S35 in the ESM). When paired with a ferrocyanide catholyte, the open-circuit voltages (OCVs) of the four isomers follow the order: **14AQS** (1.14 V) > **15AQS** (1.12 V) > **26AQS** (1.09 V) > **27AQS** (0.93 V) (Figs. 3(c) and 3(d)). Notably, **15AQS** delivers 1.12 V, marginally higher than the 1.09 V of **26AQS**, whereas **14AQS** exhibits the highest value and **27AQS** the lowest. Collectively, its appropriately negative redox potential, tunable proton-coupled redox chemistry, and complete deprotonation under alkaline operating conditions render **15AQS** exceptionally well-suited for stable, high-efficiency cycling in alkaline redox flow batteries.

2.4 Mass transport and charge transfer kinetics

The observed linear relationship between the square root scan rate and peak redox currents indicates that the electrochemical kinetics of AQs on the electrode surface are predominantly governed by a diffusion-controlled mass transfer mechanism (Fig. 3(e), Fig. S36 in the ESM). The hydration-shell architecture predicted by MD simulations has direct consequences for solute diffusion and heterogeneous electron transfer kinetics at the electrode–electrolyte interface. Initially, rotating disk electrode (RDE) voltammetry (Fig. 3(f), Figs. S37 and S38 in the ESM) was employed to quantify the diffusion coefficient (D) and heterogeneous electron transfer rate constant (k_0) for **15AQS** and **26AQS**. Furthermore, **15AQS** exhibits a diffusion coefficient of D = 1.22 × 10^{-6} $cm^2 \cdot s^{-1}$, approximately 30% greater than that of **26AQS** (9.26 × 10^{-7} $cm^2 \cdot s^{-1}$). More strikingly, the heterogeneous electron transfer kinetics are markedly accelerated: k_0 for **15AQS** reaches 4.38 × 10^{-3} $cm \cdot s^{-1}$, representing a 3.3-fold increase over **26AQS** (1.33 × 10^{-3} $cm \cdot s^{-1}$). This counterintuitive enhancement is rationalized by the MD-derived structural insight: the compact, isotropic hydration shell reduces the effective hydrodynamic radius of the solute, thereby lowering drag and enhancing translational mobility [39, 40]. Therefore, we ascribe this kinetic advantage to the dense, pre-organized hydrogen-bond network within its hydration shell, which provides structurally ordered proton-relay pathways that lower the reorganization barrier for concerted proton-coupled electron transfer (PCET) [41]. Critically, the experimentally measured aqueous solubilities (1.66 M for **15AQS** vs. 0.86 M for **26AQS**) confirm that the enhanced hydration capacity directly translates into superior bulk-phase solvation. Together, these interrelated properties, accelerated mass transport, rapid interfacial charge transfer, and high solubility, constitute the fundamental kinetic and thermodynamic enablers of the high-current-density, high-concentration operation demonstrated in subsequent full-cell redox flow battery evaluations.

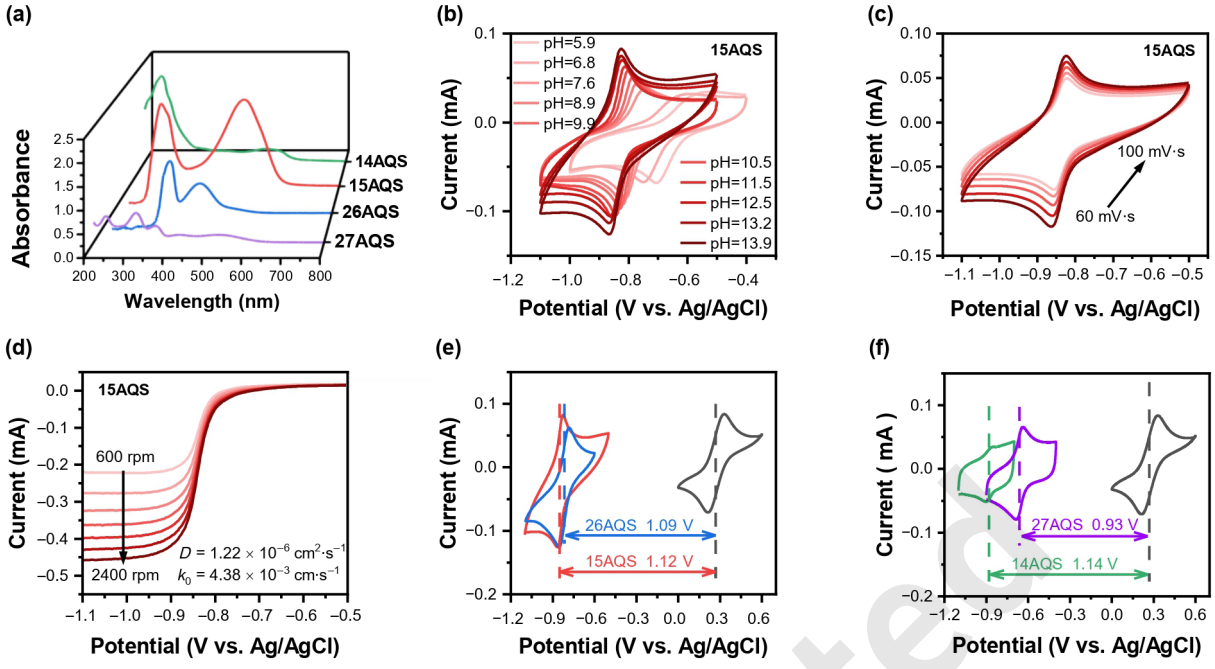

Figure 3 (a) UV–Vis absorption spectra of **AQS** solutions at different pH values; (b) CV curves of **15AQS** at various pH; (c) CV curves of **15AQS** at different scanning rates; (d) LSV of **15AQS** on a glassy carbon rotating disk electrode; (e) CV curves of the negative **15AQS** and **26AQS** (5 mM) and the positive $Na_4[Fe(CN)_6]$ (5 mM) in 1 M NaOH; (f) CV curves of the negative **14AQS** and **27AQS** (5 mM) and the positive $Na_4[Fe(CN)_6]$ (5 mM) in 1 M NaOH.

2.5 Full-cell cycling performance: 100× stability improvement

Furthermore, the combination of **15AQS** and $Na_4[Fe(CN)_6]$ delivers a cell voltage of 1.12 V, among the highest values documented for AORFBs (Table S6 in the ESM). The rate performance of AORFBs utilizing 0.05 M **15AQS** in the Vmembr-40, Nafion 212 and Thinkre N-212 membrane as the separator were evaluated (Fig. S39 in the ESM). The kinetic advantages conferred by the isotropic hydration shell directly enable superior rate capability and power output. At 0.1 M, capacity retention remains high, declining only to 71%, across a five-fold increase in current density (40 to 200 mA·cm^{-2}) (Fig. 4(a), Figs. S40–S42 in the ESM). The cells exhibited different rate-dependent behavior, with both energy density and capacity retention decreasing linearly with increasing current density, indicating of the consistent voltametric characteristics imparted by the membrane (Fig. S43 in the ESM). The peak power density reaches 222 mW·cm^{-2} at 100% SOC, which is higher than other AQ isomers under identical operating conditions (Fig. 4(b), Fig. S44 in the ESM). Moreover, the 180-day static crossover test yielded a permeability coefficient of only 5.31 × 10^{-13} cm^2·s^{-1} (Fig. 4(c)), demonstrating that membrane permeation of 15AQS is negligible, indicating no which exhibits competitive performance among similar electrolytes [42, 24, 37]. Collectively, these results demonstrate that the symmetry-engineered hydration shell achieves a multifunctional stabilization effect: it not only suppresses molecular degradation but also concurrently enhances mass transport, interfacial charge transfer kinetics, and power density, thereby providing holistic experimental validation of the molecular design principle, from isotropic hydration to degradation blockade.

To systematically validate the above theoretical predictions, we evaluated the full-cell cycling performance of all four AQ isomers (**14AQS**, **15AQS**, **26AQS**, and **27AQS**) paired with a ferrocyanide catholyte under strictly identical alkaline conditions (Fig. S45 in the ESM). As shown in Fig. 4(e), **26AQS** reveals a dramatic stability enhancement: exhibits a capacity fade rate of 0.02% per cycle over 1000 cycles, while **27AQS** shows a 0.009% per cycle degradation rate, consistent with their molecular dipole moments and hydration behaviors. In marked contrast, **14AQS**, which possesses the largest dipole moment and the most disrupted hydration shell, exhibits a distinctly different electrochemical behavior. Its accessible capacity is substantially limited, attaining only approximately 20% of the theoretical two-electron capacity. This significant capacity loss is attributable to the highly anisotropic charge distribution of **14AQS** (Fig. 1(c)). Such a disordered hydration environment not only facilitates intermolecular aggregation and irreversible adsorption onto the electrode surface, but also considerably impedes the interfacial charge-transfer kinetics, thereby suppressing the electron-transfer within the operational potential window. Encouragingly, **15AQS** retains exceptional capacity retention, with a fade rate of only 0.00018% per cycle (0.003% per day) over 2000 cycles, representing a 100-fold reduction in degradation kinetics compared to **26AQS**. The progressive performance gradient from **14AQS** (worst) through **26AQS**/**27AQS** (intermediate) to **15AQS** (best), provides compelling and systematic experimental validation of the computationally predicted dipole moment–hydration shell–stability coupling. This two-order-of-magnitude improvement provides compelling experimental validation of the computationally predicted protective hydration shell, which sterically and electrostatically suppresses bimolecular degradation pathways.

To assess practical feasibility, the electrochemical performance of **15AQS**||$Na_4[Fe(CN)_6]$ AORFBs was evaluated under high-concentration conditions using a 0.5 M negolyte (Fig. S46 in the ESM). Notably, at full charge, the system achieves a peak power density of 342 mW·cm^{-2}, reflecting competitive performance compared to previously reported quinone-based AORFBs. The enhanced power output under concentrated electrolyte conditions is primarily attributed to increased ionic conductivity, reducing

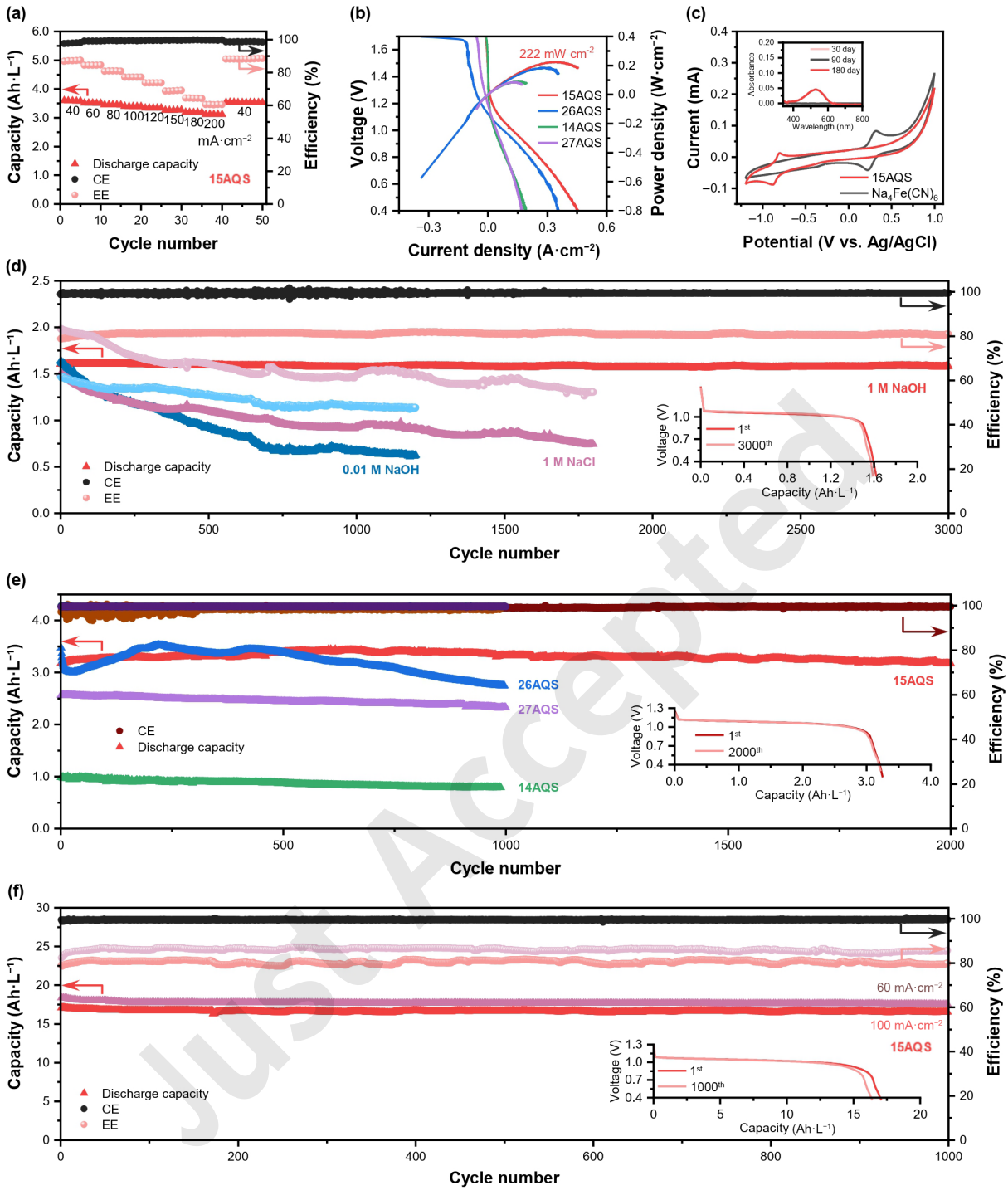

Figure 4 (a) Coulombic and energy efficiencies, discharge capacities of 0.1 M 15AQS||$Na_4[Fe(CN)_6]$ AORFB evaluated at various current densities. (b) Polarization and power density curves of 0.1 M AQs||$Na_4[Fe(CN)_6]$ AORFBs collected at SOCs of 100%. (c) CV analysis of post-cycling electrolyte of 0.1 M 15AQS and $Na_4[Fe(CN)_6]$. (d) Cycling performances of 0.05 M 15AQS||$Na_4[Fe(CN)_6]$ AORFBs at a current density of 60 mA·cm^{-2}. (e) Cycling performances of 0.1 M AQs||$Na_4[Fe(CN)_6]$ AORFBs at a current density of 100 mA·cm^{-2}. (f) Cycling performances of 0.5 M 15AQS||$Na_4[Fe(CN)_6]$ AORFBs at a current density of 60 and 100 mA·cm^{-2}.

ohmic losses, along with improved availability and more efficient utilization of electroactive species. In addition, as the current density was increased from 40 mA·cm^{-2} (20.5 Ah·L^{-1}) to 200 mA·cm^{-2} (13.9 Ah·L^{-1}), the discharge capacity retention remained at 68%. Furthermore, at the concentration of 0.5 M, it sustains a low fade rate of 0.002% per cycle over 1000 cycles at both 60 and 100 mA·cm^{-2} (Fig. 4(f)). After performance degradation, replacing the membrane separator restored both coulombic efficiency and battery capacity (Fig. S47 in the ESM), implying that membrane deterioration rather than irreversible active-material loss dominates the performance fade. Moreover, we also compared the ohmic resistance of Vmembr-40 and Nafion-212 before and after cycling in AORFBs by electrochemical impedance spectroscopy (EIS), revealing an increase in membrane resistance after cycling, correlating with the capacity decline and confirming membrane aging as a contributor

(Fig. S48 in the ESM). Additionally, the stability of **15AQS** is robust across a wide range of concentrations and current densities (Figs. S49 and S50 in the ESM). At 0.05 M, it retains >99.8% capacity after 3000 cycles (fade rate: 0.0006% per cycle) (Fig. 4(d)). Crucially, stability is maximized under strongly alkaline conditions: in 1 M NaOH (pH > 12), the fade rate drops to 0.00018% per cycle, over two orders of magnitude lower than in neutral 1 M NaCl (0.025% per cycle) and significantly lower than in dilute 0.01 M NaOH (0.049% per cycle).

To elucidate the molecular origins of this pH-dependent stabilization, we extended the explicit-solvent MD simulations of **15AQS** to the different pH environments (1 M NaOH, 1 M NaCl, and 0.01 M NaOH) under strictly unified simulation parameters (Figs. S51 and S52 in the ESM). Computational results reveal a pronounced pH-dependent behavior in the hydrogen-bond interactions between **15AQS** and water molecules under gradient pH conditions: as alkalinity increases, the number of hydrogen-bond rises significantly, while the hydrogen-bond contact distances shorten correspondingly. This overall trend is qualitatively consistent with the degradation rates observed under most experimental conditions, suggesting that a denser hydrogen-bond network with shorter contact distances effectively shields the anthraquinone core and reduces the likelihood of nucleophilic water attack. Conversely, under neutral or weakly alkaline conditions, the hydration shell becomes looser, exposing reactive sites and leading to markedly faster degradation.

However, the measured fade rate in 0.01 M NaOH is unexpectedly higher than that in 1 M NaCl, even though the former exhibits a greater number of hydrogen-bond with nearly identical contact distances. This contradiction is attributed to the insufficient supporting electrolyte concentration, which substantially increases the ionic transport resistance during charge/discharge processes and consequently causes a significant decline in energy efficiency [27]. These findings from MD simulations, together with the Pourbaix diagram (which confirms the absence of proton-coupled processes above pH 12), demonstrate that the alkaline-enhanced negative charge density drives the formation of a tightly bound, electrostatically reinforced isotropic hydration shell. This, in turn, validates the charge–hydration–stability paradigm across a wide pH range.

2.6 Mechanistic evidence for hydration-shell shielding

Subsequently, we sought direct spectroscopic and mass spectrometric evidence to validate the proposed physical shielding mechanism. Complementary *ex-situ* EPR spectroscopy (Fig. 5(a)) validates this behavior: a reversible radical signal centered at g=2.033 (3515 G) emerges during oxidation and fully disappears upon reduction, confirming that the semiquinone intermediate is kinetically competent, short-lived, and does not undergo irreversible disproportionation or coupling. Secondly, the full electrochemical reversibility of the redox process is confirmed by *in situ* UV–vis spectroscopy (Fig. 5(b)). During charging, the absorption band at 535 nm, assigned to the oxidized quinone species, decreases in intensity, while the bands at 440 and 490 nm, characteristic of the reduced hydroquinone form, increase concomitantly. Upon discharge, the spectra quantitatively revert to their initial baseline, with sharp, well-defined isosbestic points observed throughout the cycle, indicating a clean two-state interconversion. Critically, no new or evolving absorption features appear over repeated cycling, excluding the formation of spectroscopically detectable side products or degradation intermediates.

Variable temperature NMR spectroscopy of **15AQS** (Fig. 5(c), Fig. S53 in the ESM) shows that the -NH proton resonance shifts by only 0.04 ppm (from 9.68 to 9.64 ppm) upon heating from 20 to 60 °C. This exceptional thermal rigidity indicates that the amino protons are immobilized within a persistent, highly ordered H-bond network with surrounding water molecules, consistent with the 'chaperone-like' encapsulation predicted by molecular dynamics simulations. In contrast, a solvent-exposed –NH group undergoing rapid proton exchange would typically exhibit a temperature coefficient exceeding 0.1 ppm/°C. Therefore, the observed minimal shift therefore provides direct experimental confirmation that the hydration shell sterically and dynamically isolates the -NH sites, effectively preventing oxidative dimerization.

Furthermore, to directly correlate molecular structural evolution with charge injection under operational conditions, we performed *in situ* Fourier-transform infrared (FTIR) spectroscopy on electrolyte samples extracted at precisely controlled potentials along the charge–discharge profile. The resulting spectral series (Fig. 5(d)) provides a definitive vibrational fingerprint of the two-electron redox process. In the fully discharged state, the characteristic carbonyl stretching vibration ($\nu_{C=O}$) of the AQ core appears at 1659 cm^{-1}. Upon stepping the potential toward the first electron transfer region, this band progressively attenuates in intensity, while a new absorption emerges at 1603 cm^{-1}, assigned to semiquinone-specific ring deformation and C–O• radical stretching modes. Further potential increase into the second electron transfer region causes this intermediate feature to vanish and gives rise to a strong, broad absorption centered at 1269 cm^{-1}, corresponding to the C–O^- asymmetric stretch of the fully reduced hydroquinone dianion.

To identify the minimal degradation pathways operative under extended cycling, high-resolution mass spectrometry was performed on cycled electrolyte (Fig. 5(d), Fig. S54–S57 in the ESM) [43, 44]. Notably, only three trace-level degradation product classes were detected: i) a C–C coupled dimer linked at the C3 position of the AQ ring; ii) a sulfonate-reduced species, consistent with partial reduction to sulfinate, thiol, or alcohol functionalities; and iii) mono- or di-deaminated derivatives. Moreover, Fukui function analysis under implicit water solvation provides a quantitative rationale for this site selectivity: for neutral **15AQS**, the condensed Fukui indices for electrophilic and radical attack are maximized at C2-C4, with C3 (0.0173) exhibiting the highest reactivity. Notably, C3 remains the most nucleophilic/radical-prone site even in the two-electron-reduced hydroquinone state (0.0147), confirming its role as the thermodynamically favored locus for intermolecular C–C coupling (Fig. 5(e), Figs. S58 and S59 in the ESM).

To further probe the role of solvation, we extended the Fukui calculations to the gas phase (in vacuo), eliminating the effect of water. The condensed Fukui index at C3 in the gas phase is substantially higher than that obtained with implicit water solvation, indicating that the aqueous solvation shell significantly attenuates the intrinsic electrophilic/radical reactivity of this site. This attenuation arises from the electrostatic and hydrogen-bonding interactions between water molecules and the polar sulfonate/anthraquinone moieties, which effectively delocalize the electron density and raise the energetic barrier for radical coupling at C3. Such a solvation-induced suppression of C3 reactivity is fully consistent with our MD simulations. Collectively, the combined experimental and computational evidence—ranging from degradation product identification and solvated Fukui

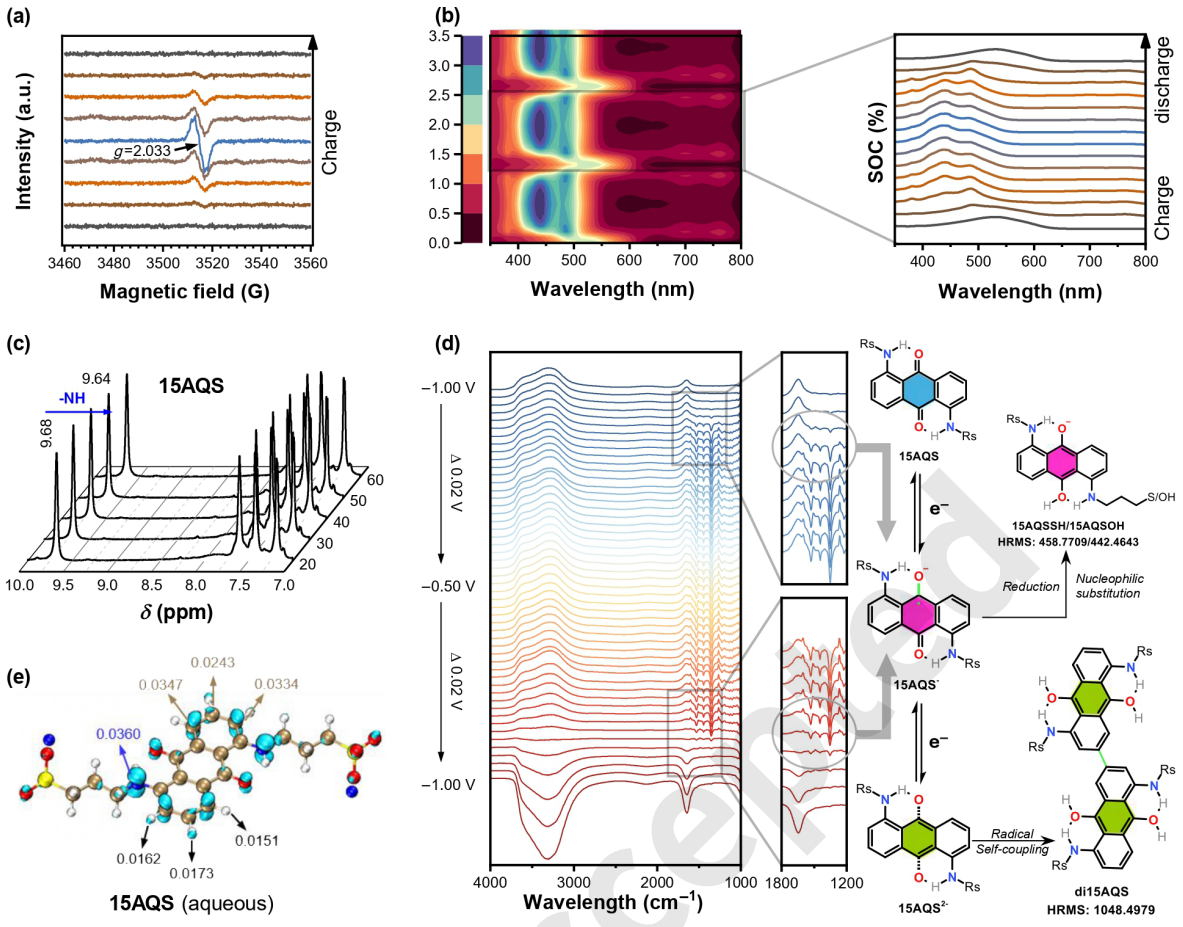

Figure 5 (a) EPR spectra of 15AQS negolyte under different SOCs. (b) Contour plot and *in-situ* UV–Vis spectra of 15AQS negolyte measured during charge-discharge cycles. (c) A variable-temperature H^1-NMR study on hydrogen bond migration. (d) *In-situ* FTIR measurements of 0.05 M 15AQS in an electrochemical cell and plausible reaction mechanism of 15AQS negolyte during charge-discharge cycles. (e) CFF calculations of 15AQS.

analysis to gas-phase comparisons and explicit-solvent MD—establishes that the water hydration shell plays a dual protective role: it not only hinders nucleophilic attack but also mitigates the intrinsic coupling propensity at the most reactive site, thereby contributing to the exceptionally high stability of **15AQS** under prolonged cycling. Critically, the entire transformation is fully reversible upon discharge, with all spectral features returning quantitatively to their initial positions and intensities. No extraneous or persistent peaks appear across the full electrochemical window, confirming the absence of spectroscopically detectable side products even under extreme oxidative or reductive polarization. This clean, stepwise vibrational progression confirms that the isotropic hydration shell enables unimpeded two-electron charge delivery while simultaneously suppressing bimolecular coupling of electrogenerated intermediates. Integrated with UV–vis and EPR, these FTIR results provide conclusive spectroscopic evidence for a redox-active core that is both perfectly shielded from parasitic reactions and fully accessible to electron transfer.

Moreover, the critical finding is that, despite this thermodynamic predisposition toward C3–C3 coupling, dimerization is kinetically suppressed to near-negligible levels. Collectively, the NMR, HRMS, *in situ* UV-vis, *ex situ* EPR and FTIR, and data converge to form a coherent mechanistic picture: the isotropic hydration shell physically encapsulates the anthraquinone core, immobilizes the -NH protons within a structurally rigid hydrogen-bond network, and sterically hinders the close approach of two molecules at their Fukui-activated C3 positions. The trace degradation products detected represent rare breach events, transient failures of this dynamic protective barrier, whereas the vast majority of active molecules remain fully shielded across hundreds of cycles, thereby enabling the two-orders-of-magnitude enhancement in operational stability.

Further investigation reveals that, following a period of operation in 0.5 M **15AQS**||$Na_4[Fe(CN)_6]$ AORFB, the introduction of air leads to a rapid decrease in both capacity and energy efficiency. However, upon nitrogen purging, the AORFB capacity is fully recoverable to its initial level (Fig. S60 in the ESM). This demonstrates that the **15AQS** species exhibits low air sensitivity, thereby substantially improving its feasibility for large-scale energy storage applications.

2.7 Derive a generalizable design rule

Collectively, the comprehensive dataset presented above converges on a unifying molecular design principle: from core symmetry and a near-zero dipole moment, to an isotropic hydration shell, to physical blockade of bimolecular degradation, and ultimately to ultra-low-capacity fade. Moreover, the decisive factor is not the chemical nature of the solubilizing substituents, but symmetry-enforced cancellation of local charge anisotropy. **15AQS** achieves this cancellation with exceptional fidelity (dipole = 0.003 D), thereby nucleating a highly ordered hydration shell that simultaneously encapsulates the π-surface, rigidifies the reactive -NH protons *via* a well-defined H-bond network, and sterically blocks approach between Fukui-activated C3 sites. In direct

contrast, the highly asymmetric **14AQS**, possessing the largest dipole moment, exhibits the most disrupted hydration shell and the poorest electrochemical behavior, attaining only ~20% of its theoretical two-electron capacity due to severe aggregation and retarded interfacial charge transfer. The moderately polar **27AQS** and **26AQS** fall in between, respectively, and corresponding capacity fade rates of 0.009% and 0.02% per cycle, both inferior to the 0.00018% per cycle achieved by **15AQS**. This progressive performance gradient across the four isomers provides compelling experimental validation that hydration-shell integrity, dictated by core dipole magnitude, directly governs molecular stability. While the present work systematically investigates how substituent position, electronic distribution, intramolecular hydrogen bonding, collectively modulate the molecular dipole moment and hydration architecture within the anthraquinone series, the proposed design principle may be extendable to other redox-active aromatic systems.

In principle, symmetric installation of hydrophilic substituents that effectively reduce molecular dipole could promote the formation of protective hydration shells in a broader range of frameworks. However, given that substituent position, steric hindrance, electronic distribution, conformational flexibility of the sulfonate arms, intramolecular hydrogen bonding, and local charge density all influence the net dipole moment and consequently the hydration shell structure, the applicability of this strategy to other molecular systems requires further validation. Importantly, because both dipole moments and hydration structures are computationally tractable using standard DFT and MD simulations, this strategy offers a promising route for a priori screening. Ongoing efforts in our group are dedicated to testing the generality of this hydration-shell engineering concept across diverse molecular scaffolds, and preliminary results are encouraging. Collectively, this work establishes a rational, longevity-by-design framework, from core symmetry to isotropic hydration and thence to degradation blockade, for developing durable organic energy-storage materials.

3 Conclusions

In summary, we have established and experimentally validated a molecular design principle, spanning core symmetry, isotropic hydration, and degradation blockade, for suppressing bimolecular degradation in aqueous organic flow battery anolytes. Notably, the perfectly symmetric 1,5-diaminoanthraquinone core eliminates the molecular dipole moment, thereby nucleating a dense, highly ordered hydration shell that i) immobilizes reactive –NH protons via a rigid hydrogen-bond network, ii) fully encapsulates the π-conjugated surface, and iii) sterically shields the Fukui-activated C3 sites against intermolecular coupling. As a result, **15AQS** delivers an ultra-low-capacity fade rate of 0.00018% per cycle, two orders of magnitude lower than that of the 1,4- 1,5- and 2,7-isomers, and achieves a peak power density of 342 $mW \cdot cm^{-2}$ at a concentration of 0.5 M. Thus, this symmetry-directed hydration-shell engineering strategy is quantitatively predictable using standard DFT and MD simulations, enabling rigorous a priori computational screening; it further provides a broadly generalizable framework for achieving molecular longevity through rational design in organic energy-storage materials.

Acknowledgements

The authors are grateful to the financial support of the Science and Technology Project of Shanxi Province of China (202303021221256, 202502060302014), the Research Project Supported by Shanxi Scholarship Council of China (2024-159), the International Cooperation Bureau CAS (040GJHZ2024013MI), the State Key Laboratory of Coal Conversion, Institute of Coal Chemistry CAS (2026BWZ003).

Declaration of conflicting interests

The authors declare no conflicting interests regarding the content of this article.

Data availability

All data needed to support the conclusions in the paper are presented in the manuscript and/or the Supplementary Materials. Additional data related to this paper may be requested from the corresponding author upon request.

Electronic Supplementary Material: Supplementary material (please send us a short summary regarding the Supporitng info, thanks) in the online version of this article at https://doi.org/10.26599/NRE.2026.9120268.

References

[1] Zhang, C. K.; Yuan, Z. Z.; Li, X. F. Designing better flow batteries: An overview on fifty years' research. *ACS Energy Lett.* **2024**, *9*, 3456–3473.

[2] Hou, Z. X.; Chen, X.; Liu, J.; Huang, Z. Y.; Chen, Y.; Zhou, M. Y.; Liu, W.; Zhou, H. H. Towards a high efficiency and low-cost aqueous redox flow battery: A short review. *J. Power Sources* **2024**, *601*, 234242.

[3] Brushett, F. R.; Aziz, M. J.; Rodby, K. E. On lifetime and cost of redox-active organics for aqueous flow batteries. *ACS Energy Lett.* **2020**, *5*, 879–884.

[4] Ding, Y.; Zhang, C. K.; Zhang, L. Y.; Zhou, Y. G.; Yu, G. H. Molecular engineering of organic electroactive materials for redox flow batteries. *Chem. Soc. Rev.* **2018**, *47*, 69–103.

[5] Huskinson, B.; Marshak, M. P.; Suh, C.; Er, S.; Gerhardt, M. R.; Galvin, C. J.; Chen, X. D.; Aspuru-Guzik, A.; Gordon, R. G.; Aziz, M. J. A metal-free organic-inorganic aqueous flow battery. *Nature* **2014**, *505*, 195–198.

[6] Lin, K. X.; Chen, Q.; Gerhardt, M. R.; Tong, L. C.; Kim, S. B.; Eisenach, L.; Valle, A. W.; Hardee, D.; Gordon, R. G.; Aziz, M. J. et al. Alkaline quinone flow battery. *Science* **2015**, *349*, 1529–1532.

[7] Zhang, P. B.; Wen, S.; Chen, Y. K.; Liu, Y. Z.; Wei, J.; Wu, Z. A.; Ding, G. C.; Song, X. M.; Dai, T. F.; You, Z. H. et al. Structurally asymmetric nonplanar π-conjugated naphthoquinone derivatives modified from natural lawsone for high-stability aqueous redox flow batteries. *Angew. Chem., Int. Ed.* **2026**, *65*, e19793.

[8] Gerhardt, M. R.; Tong, L. C.; Gómez-Bombarelli, R.; Chen, Q.; Marshak, M. P.; Galvin, C. J.; Aspuru-Guzik, A.; Gordon, R. G.; Aziz, M. J. Anthraquinone derivatives in aqueous flow batteries. *Adv. Energy Mater.* **2017**, *7*, 1601488.

[9] Peng, K.; Tang, G. G.; Zhang, C.; Yang, X.; Zuo, P. P.; Xiang, Z. F.; Yao, Z.; Yang, Z. J.; Xu, T. W. Progress and prospects of pH-neutral aqueous organic redox flow batteries: Electrolytes and membranes. *J. Energy Chem.* **2024**, *96*, 89–109.

[10] Kwabi, D. G.; Ji, Y. L.; Aziz, M. J. Electrolyte lifetime in aqueous organic redox flow batteries: A critical review. *Chem. Rev.* **2020**, *120*, 6467–6489.

[11] Yang, B.; Hoober-Burkhardt, L.; Wang, F.; Prakash, G. K. S.; Narayanan, S. R. An inexpensive aqueous flow battery for large-scale electrical energy storage based on water-soluble organic redox couples. *J. Electrochem. Soc.* **2014**, *161*, A1371–A1380.

[12] Fang, M. L.; Cheng, J. Y.; Li, X. F.; Zhang, C. K. Degradation mechanisms of redox-active molecules toward long-cycle aqueous

organic flow batteries. *ACS Appl. Energy Mater.* **2025**, *8*, 14001–14013.
[13] Wiberg, C.; Carney, T. J.; Brushett, F.; Ahlberg, E.; Wang, E. G. Dimerization of 9,10-anthraquinone-2,7-disulfonic acid (AQDS). *Electrochim. Acta* **2019**, *317*, 478–485.
[14] Carney, T. J.; Collins, S. J.; Moore, J. S.; Brushett, F. R. Concentration-dependent dimerization of anthraquinone disulfonic acid and its impact on charge storage. *Chem. Mater.* **2017**, *29*, 4801–4810.
[15] Wang, X.; Gautam, R. K.; Jiang, J. Strategies for improving solubility of redox-active organic species in aqueous redox flow batteries: A review. *Batteries Supercaps* **2022**, *5*, e202200298.
[16] Wang, P. Molecular design and redox chemistries for aqueous organic redox flow batteries (AORFBs). *Angew. Chem., Int. Ed.* **2025**, *64*, e202515639.
[17] Ruan, W. Q.; Mao, J. T.; Chen, Q. Redox flow batteries toward more soluble anthraquinone derivatives. *Curr. Opin. Electrochem.* **2021**, *29*, 100748.
[18] Li, D. J.; Lan, J. J.; Ge, X. Y.; Cui, L. P.; Han, Y. H.; Li, K.; Feng, L. B.; Yang, L.; Lin, H. Y.; Chen, J. J. Designs and applications of organic redox couples in aqueous flow batteries. *Chem. -Asian J.* **2025**, *20*, e202500020.
[19] Ding, G. C.; Shen, T. Y.; Zhang, P. B.; Wu, Z. A.; Yu, Q. C.; Liu, Y. Z.; Wen, S.; Wei, J.; Tie, Z.; Yan, Y. C. et al. Nature-inspired glycosylation strategy enabled hydrosoluble polyhydric thioalkylated ferrocene derivatives for pH-neutral aqueous redox flow batteries. *J. Am. Chem. Soc.* **2025**, *147*, 38435–38442.
[20] Liu, Y. Z.; Wu, Z. A.; Zhang, P. B.; Wei, J.; Li, J. J.; Wang, H. Z.; Wen, S.; Liang, J. C.; Chen, Y. K.; Dai, T. F. et al. Artificial α-amino acid based on cysteine grafted natural aloe-emodin for aqueous organic redox flow batteries. *Nat. Commun.* **2025**, *16*, 2965.
[21] Fornari, R. P.; De Silva, P. Molecular modeling of organic redox-active battery materials. *WIREs Comput. Mol. Sci.* **2021**, *11*, e1495.
[22] Zhang, P. B.; Liu, Y. Z.; Wei, J.; Wu, Z. A.; Song, X. M.; Ding, G. C.; Wang, H. Z.; Liang, J. C.; Tie, Z.; Jin, Z. An amphoteric and hydrogen-bond-rich artificial α-amino acid for highly durable aqueous redox flow batteries. *Nat. Commun.* **2025**, *16*, 4727.
[23] Maleki, M.; Goulet, M. A. Enhanced solubility and stability of active species in flow battery electrolytes via suppressed anthraquinone aggregation. *J. Mater. Chem. A* **2025**, *13*, 38858–38865.
[24] Xu, L.; Wang, Q. W.; Guo, D. F.; Xu, J.; Cao, J. Y. A quaternized anthraquinone derivative for pH-neutral aqueous organic redox flow batteries. *New J. Chem.* **2023**, *47*, 11216–11221.
[25] Xia, L. X.; Zhang, Y. J.; Wang, F. Z.; Chu, F. M.; Yang, Y.; Li, H.; Tan, Z. A low-potential and stable bis-dimethylamino-substituted anthraquinone for pH-neutral aqueous redox flow batteries. *ChemElectroChem* **2022**, *9*, e202200224.
[26] Wu, M.; Bahari, M.; Jing, Y.; Amini, K.; Fell, E. M.; George, T. Y.; Gordon, R. G.; Aziz, M. J. Highly stable, low redox potential quinone for aqueous flow batteries. *Batteries Supercaps* **2022**, *5*, e202200009.
[27] Wang, C. X.; Yu, B.; Liu, Y. Z.; Wang, H. Z.; Zhang, Z. W.; Xie, C. X.; Li, X. F.; Zhang, H. M.; Jin, Z. N-alkyl-carboxylate-functionalized anthraquinone for long-cycling aqueous redox flow batteries. *Energy Storage Mater.* **2021**, *36*, 417–426.
[28] Yang, W. H.; Du, X. F.; Zhao, J. W.; Chen, Z.; Li, J. J.; Xie, J.; Zhang, Y. J.; Cui, Z. L.; Kong, Q. Y.; Zhao, Z. M. et al. Hydrated eutectic electrolytes with ligand-oriented solvation shells for long-cycling zinc-organic batteries. *Joule* **2020**, *4*, 1557–1574.
[29] Lu, T.; Chen, F. W. Quantitative analysis of molecular surface based on improved marching tetrahedra algorithm. *J. Mol. Graphics Modell.* **2012**, *38*, 314–323.
[30] Zhang, J.; Lu, T. Efficient evaluation of electrostatic potential with computerized optimized code. *Phys. Chem. Chem. Phys.* **2021**, *23*, 20323–20328.
[31] Lu, T. A comprehensive electron wavefunction analysis toolbox for chemists, Multiwfn. *J. Chem. Phys.* **2024**, *161*, 082503.
[32] Lu, T.; Chen, F. W. Multiwfn: A multifunctional wavefunction analyzer. *J. Comput. Chem.* **2012**, *33*, 580–592.
[33] Humphrey, W.; Dalke, A.; Schulten, K. VMD: Visual molecular dynamics. *J. Mol. Graphics* **1996**, *14*, 33–38.
[34] Geerlings, P.; De Proft, F.; Langenaeker, W. Conceptual density functional theory. *Chem. Rev.* **2003**, *103*, 1793–1874.
[35] Abraham, M. J.; Murtola, T.; Schulz, R.; Páll, S.; Smith, J. C.; Hess, B.; Lindahl, E. GROMACS: High performance molecular simulations through multi-level parallelism from laptops to supercomputers. *SoftwareX* **2015**, *1–2*, 19–25.
[36] Maleki, M.; Imhanria, S.; Duguet, L.; Goulet, M. A. Stability of alizarin as a low-cost anthraquinone for aqueous redox flow batteries. *J. Electrochem. Soc.* **2024**, *171*, 120537.
[37] Xia, L. X.; Huo, W. B.; Gao, H. Z.; Zhang, H.; Chu, F. M.; Liu, H.; Tan, Z. Intramolecular hydrogen bonds induced high solubility for efficient and stable anthraquinone based neutral aqueous organic redox flow batteries. *J. Power Sources* **2021**, *498*, 229896.
[38] Kerr, E. F.; Tang, Z. J.; George, T. Y.; Jin, S. J.; Fell, E. M.; Amini, K.; Jing, Y.; Wu, M.; Gordon, R. G.; Aziz, M. J. High energy density aqueous flow battery utilizing extremely stable, branching-induced high-solubility anthraquinone near neutral pH. *ACS Energy Lett.* **2023**, *8*, 600–607.
[39] Liu, X.; Bao, C. Y.; Wang, Z. R.; Liu, C. J.; Zhang, X. R.; Yang, S. R.; Li, Y. K.; Hou, G. L.; Yan, N.; He, G. *Meta*-substituted thienoviologen with enhanced radical stability via π-π interaction modulation for neutral aqueous organic flow batteries. *Energy Storage Mater.* **2024**, *73*, 103824.
[40] Sharma, K.; Sankarasubramanian, S.; Parrondo, J.; Ramani, V. Electrochemical implications of modulating the solvation shell around redox active organic species in aqueous organic redox flow batteries. *Proc. Natl. Acad. Sci. USA* **2021**, *118*, e2105889118.
[41] Bonin, J.; Costentin, C.; Robert, M.; Savéant, J. M.; Tard, C. Hydrogen-bond relays in concerted proton-electron transfers. *Acc. Chem. Res.* **2012**, *45*, 372–381.
[42] Kwabi, D. G.; Lin, K. X.; Ji, Y. L.; Kerr, E. F.; Goulet, M. A.; De Porcellinis, D.; Tabor, D. P.; Pollack, D. A.; Aspuru-Guzik, A.; Gordon, R. G. et al. Alkaline quinone flow battery with long lifetime at pH 12. *Joule* **2018**, *2*, 1894–1906.
[43] Jin, S. J.; Jing, Y.; Kwabi, D. G.; Ji, Y. L.; Tong, L. C.; De Porcellinis, D.; Goulet, M. A.; Pollack, D. A.; Gordon, R. G.; Aziz, M. J. A water-miscible Quinone flow battery with high volumetric capacity and energy density. *ACS Energy Lett.* **2019**, *4*, 1342–1348.
[44] Ji, Y. L.; Goulet, M. A.; Pollack, D. A.; Kwabi, D. G.; Jin, S. J.; De Porcellinis, D.; Kerr, E. F.; Gordon, R. G.; Aziz, M. J. A phosphonate-functionalized Quinone redox flow battery at near-neutral pH with record capacity retention rate. *Adv. Energy Mater.* **2019**, *9*, 1900039.

Wentao Hao received his B.S. degree in 2022 from Anhui University of Science and Technology. He is currently a PhD student in the research group of Prof. Guoying Zhang at the State Key Laboratory of Coal Conversion, Institute of Coal Chemistry Chinese Academy of Sciences. His research focuses on the preparation and performance investigation of organic electrolytes for aqueous organic flow batteries.

Chunyan Zhang is currently a lecturer at the College of Environment and Ecology, Taiyuan University of Technology. She obtained her Bachelor's, Master's and Doctoral degrees successively from University of Jinan, Zhejiang Normal University and Lanzhou Institute of Chemical Physics Chinese Academy of Sciences. She carried out postdoctoral research at the State Key Laboratory of Coal Conversion, Institute of Coal Chemistry, Chinese Academy of Sciences from 2021 to 2022. She also had short-term academic visits to the University of Bayreuth, Germany, in the summers of 2017 and 2018. Her research interests include synthetic methodology, catalysis, and sustainable energy storage.

Guoying Zhang is a research professor and doctoral supervisor at the Institute of Coal Chemistry Chinese Academy of Sciences. He obtained his Bachelor's, Master's and Doctoral degrees successively from University of Jinan, Wenzhou University and Lanzhou Institute of Chemical Physics Chinese Academy of Sciences. He carried out postdoctoral research as an Alexander von Humboldt Foundation at the University of Bayreuth from 2017 to 2019. Recruited by the CAS Hundred Talents Program in 2021, he now leads a research group engaged in coal low-carbon utilization and green energy storage. His research spans organic, catalysis and aqueous organic flow batteries.

Electronic Supplementary Material

Symmetry-driven isotropic hydration suppresses degradation of anthraquinone positional isomers in aqueous organic flow batteries via dipole cancellation

Wentao Hao[1,3], Xiaoyu Zhi[1], Chunyan Zhang[2] (✉), and Guoying Zhang[1,3] (✉)

[1] *State Key Laboratory of Coal Conversion, Institute of Coal Chemistry Chinese Academy of Sciences, Taiyuan 030001, China*
[2] *School of Environmental and Engineering, Taiyuan University of Technology, Taiyuan 030001, China*
[3] *University of Chinese Academy of Sciences, Beijing 100049, China*

Supporting information to https://doi.org/10.26599/NRE.2026.9120268

Address correspondence to Chunyan Zhang, zhanggy527@163.com; Guoying Zhang, zhanggy@sxicc.ac.cn

General

Experimental: All chemicals were purchased from Adamas and used without further purification. Graphite felts were obtained from Liaoning Jingu Carbon Materials Co., Ltd., China. Graphite electrodes were obtained from Dongguan Juxi Trading Co.Ltd., China. The pre-cut graphite felt electrodes (4 mm thick, 2 cm × 2 cm) were thermally treated at 400 °C for 12 h. Nafion-212 membranes were purchased from DuPont Corp., USA. Vmembr-40 membranes were purchased from Suzhou Tuoji New Material Technology Co., Ltd., China. Thinkre N-212 membranes were purchased from THINKRE Group., China. The copper plates (99.98%, 3 mm thickness) were purchased from Dongguan Huatai Metal Materails Co., Ltd. Electrolyte circulation was maintained using a peristaltic pump (NKCP, Kamoer, China) at a flow rate of 65 mL min^{-1}. All reactions and electrochemical tests were conducted under a nitrogen atmosphere. Redox flow batteries were operated using a 5V/6A battery test station (Wuhan Land Instruments, China) and the pH values were measured using a pH meter (pHS-3C, INESA, China) calibrated with standard buffer solutions at pH 4.00 and pH 6.86. All electrochemical tests were conducted with a Gamry 5000E electrochemical test system (Gamry Instruments, America) or a CHI 660E electrochemical workstation (Chen Hua Instruments, China). All NMR spectra were collected with a Bruker 400 MHz spectrometer at 25 °C. The EPR spectra were collected with a Bruker EMXPLUS10/12. The ultraviolet-visible (UV–Vis) and *in-situ* UV-Vis absorption spectra of the samples at different concentrations were measured using a UV–Vis spectrometer (756N, INESA Co. Ltd). High resolution mass spectra (HRMS) were recorded on Bruker MicroTOF-QII mass (ESI).

Synthesis *N,N*-bis(propane-1-sulfonate)-1,4-diaminoanthraquinone (14AQS)

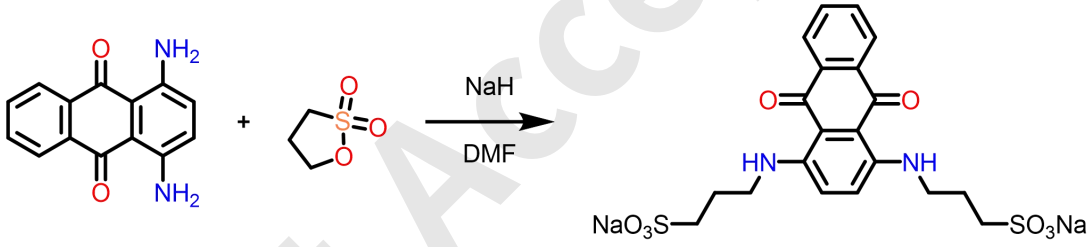

14AQ **14AQS**, 93%

First, 4.8 g (20.0 mmol) of 1,4-diaminoanthraquinone (**14AQ**) was added to 100 mL of DMSO, followed by the addition of 1.8 g (60%, 44.0 mmol) of NaH under vigorous stirring. The mixture was stirred for 1 hour until gas evolution ceased and the solution turned dark green. Subsequently, 3.9 mL (44.0 mmol) of 1,3-propanesultone was added dropwise, and the reaction was allowed to proceed for 5 hours, during which the solution color changed to black. Upon completion of the reaction, the mixture was poured into a large volume of ethyl acetate (EA), resulting in the precipitation of a black solid. The precipitate was collected by suction filtration and washed thoroughly with ethyl acetate until the filtrate became colorless. After drying under vacuum, the product of black solid was obtained with a yield of 93% (9.8 g).

^{1}H NMR (400 MHz, DMSO-d_6) 8.27 – 8.12 (m, 2H), 7.74 – 7.80 (m, 2H), 7.44 – 7.53 (m, 2H), 4.23 – 3.82 (m, 4H), 2.79 – 2.66 (m, 4H), 2.39 – 2.20 (m, 4H).

HRMS (ESI) calcd. for $Na_2C_{20}H_{21}O_8N_2S_2$ $[M+H]^+$: 527.0534, found: 527.0536.

Elemental Analysis calcd for $Na_2C_{20}H_{20}O_8N_2S_2$: C, 45.63; H, 3.83; N, 5.32; Na, 8.73; O, 24.31; S, 12.18; found: C, 45.59; H, 3.85; N, 5.34

Synthesis *N,N*-bis(propane-1-sulfonate)-1,5-diaminoanthraquinone (15AQS)

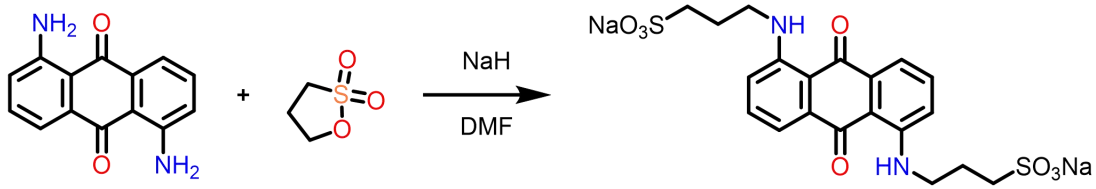

15AQ **15AQS**, 97%

First, 119.3 g (0.5 mol) of 1,5-diaminoanthraquinone (**15AQ**) was added to 2.0 L of DMSO, followed by the addition of 44.0 g (60%, 1.1 mol) of NaH under vigorous stirring. The mixture was stirred for 1 hour until gas evolution ceased and the solution turned dark green. Subsequently, 110 mL (1.1 mol) of 1,3-propanesultone was added dropwise, and the reaction was allowed to proceed for 5 hours, during which the solution color changed to reddish-purple. Upon completion of the reaction, the mixture was poured into a large volume of EA, resulting in the precipitation of a purple solid. The precipitate was collected by suction filtration and washed thoroughly with ethyl acetate until the filtrate became colorless. After drying under vacuum, the product of deep purple solid was obtained with a yield of 96% (0.25 kg).

^{1}H NMR (400 MHz, DMSO-d_6) δ 9.68 (t, J = 5.6 Hz, 2H), 7.61 (t, J = 8.0 Hz, 2H), 7.43 (d, J = 7.2 Hz, 2H), 7.19 (d, J = 8.4 Hz, 2H), 3.46 (q, J = 6.4, 6.0 Hz, 4H), 2.56 (t, J = 7.6 Hz, 4H), 1.98 - 1.90 (m, 4H).

^{13}C NMR (100 MHz, DMSO-d_6) δ 184.3, 151.2, 135.59, 135.55, 117.2, 114.3, 111.9, 48.7, 41.2, 25.1.

HRMS (ESI) calcd. for $Na_2C_{20}H_{21}O_8N_2S_2$ $[M+H]^+$: 527.0534, found: 527.0540.

Synthesis *N,N*-bis(propane-1-sulfonate)-2,6-diaminoanthraquinone (26AQS)

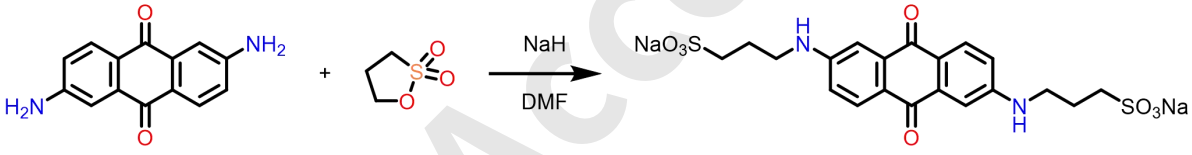

26AQ **26AQS**, 72%

First, 47.7 g (0.2 mol) of 2,6-diaminoanthraquinone (**26AQ**) was added to 1 L of DMSO, followed by the addition of 20 g (0.5 mol) of NaH under vigorous stirring. The mixture was stirred for 1 hour until gas evolution ceased and the solution turned dark green. Subsequently, 50 mL (0.5 mol) of 1,3-propanesultone was added dropwise, and the reaction was allowed to proceed for 5 hours, during which the solution color changed to dark brown. Upon completion of the reaction, the mixture was poured into a large volume of EA, resulting in the precipitation of a yellowish-brown solid. The precipitate was collected by suction filtration and washed thoroughly with ethyl acetate until the filtrate became colorless. After drying under vacuum, the product of yellowish-brown solid was obtained with a yield of 72% (76.0 g).

^{1}H NMR (400 MHz, D_2O) δ 7.67 (d, J = 8.8 Hz, 2H), 7.02 (s, 2H), 6.79 (d, J = 9.2 Hz, 2H), 3.51 (t, J = 7.6 Hz, 4H), 3.00 (t, J = 7.6 Hz, 4H), 2.10 – 2.01 (m, 4H).

^{13}C NMR (100 MHz, D_2O) δ 183.0, 152.2, 135.4, 130.0, 120.6, 114.9, 108.2, 48.3, 38.7, 22.3.

HRMS (ESI) calcd. for $Na_2C_{20}H_{21}O_8N_2S_2$ $[M+H]^+$: 527.0534, found: 527.0548.

Synthesis 2,7-diaminoanthraquinone (27AQ)

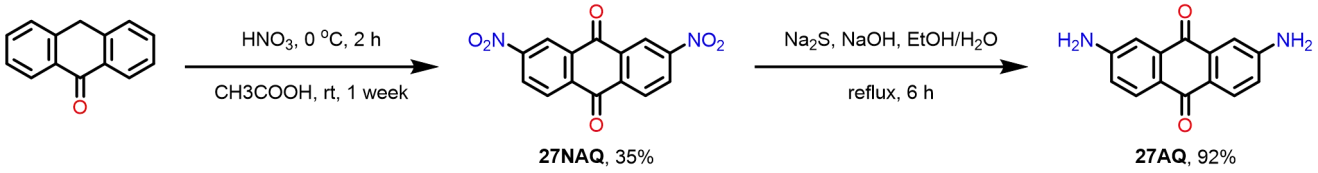

First, 19.4 g (0.1 mol) of anthrone was added to 100 mL of fuming nitric acid under stirring in 2 h at 0 °C. Until the addition was completed, and then the reaction mixture was poured into 500 mL of ice-cooled glacial acetic acid. Subsequently, allowed to warm up to room temperature and allowed to stand at room temperature for 1 week, resulting in the gradual precipitation of a yellow solid. Upon completion of the standing process, the precipitate was collected by filtration and washed sequentially with glacial acetic acid and ethyl ether. After drying under vacuum, a yellow solid was obtained with a yield of 35% (10.4 g). The crude product was used directly in the next reaction without further purification.

Then, 10.4 g (34.9 mmol) of **27NAQ** was added to 350 mL of ethanol under stirring, followed by the addition of an aqueous solution containing 39.0 g (162 mmol) of $Na_2S{\cdot}9H_2O$ and 15.4 g (384 mmol) of NaOH dissolved in 600 mL of water. The mixture was heated under reflux for 6 h and then left to stand overnight. Subsequently, ethanol was removed under reduced pressure, and the remaining residue was cooled to 0 °C. The precipitate was collected by filtration, washed with water, and dried under vacuum. After recrystallization from ethanol/water (3:1 v/v), the final product was obtained as an orange-red solid with a yield of 92% (7.35 g).[1]

^{1}H NMR (400 MHz, DMSO-d_6) δ 7.84 (d, J = 8.4 Hz, 2H), 7.22 (d, J = 2.4 Hz, 2H), 6.89 (dd, J = 8.4, 2.4 Hz, 2H), 6.40 (s, 4H).

^{13}C NMR (100 MHz, DMSO-d_6) δ 184.3, 179.4, 153.8, 134.9, 129.0, 122.0, 118.0, 109.7.

Synthesis *N,N*-bis(propane-1-sulfonate)-2,7-diaminoanthraquinone (27AQS)

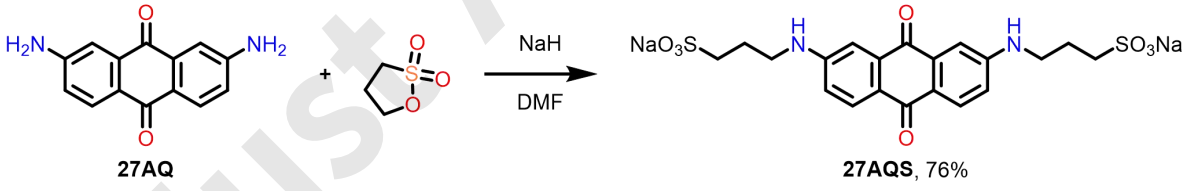

First, 4.8 g (20.0 mmol) of 2,7-diaminoanthraquinone (**27AQ**) was added to 100 mL of DMSO, followed by the addition of 1.8 g (60%, 44.0 mmol) of NaH under vigorous stirring. The mixture was stirred for 1 hour until gas evolution ceased and the solution turned dark green. Subsequently, 3.9 mL (44.0 mmol) of 1,3-propanesultone was added dropwise, and the reaction was allowed to proceed for 5 hours, during which the solution color changed to black. Upon completion of the reaction, the mixture was poured into a large volume of EA, resulting in the precipitation of a black solid. The precipitate was collected by suction filtration and washed thoroughly with ethyl acetate until the filtrate became colorless. After drying under vacuum, the product of black solid was obtained with a yield of 76% (8.0 g).

^{1}H NMR (400 MHz, D_2O) δ 7.05 – 7.29 (m, 2H), 6.74 – 6.12 (m, 4H), 3.04 – 3.19 (m, 3H), 2.93 – 2.87 (m, 1H), 2.79 – 2.75 (m, 4H), 1.81 – 1.74 (m, 4H).

^{13}C NMR (100 MHz, D_2O) δ 185.1, 181.3, 152.5, 152.3, 151.2, 151.1, 134.1, 133.9, 129.2, 128.9, 121.7, 121.5, 121.0, 120.9, 115.7, 115.6, 108.2, 108.0, 49.1, 48.8, 48.4, 48.0, 23.9, 22.4.

HRMS (ESI) calcd. for $Na_2C_{20}H_{21}O_8N_2S_2$ $[M+H]^+$: 527.0534, found: 527.0548.

Electrochemical characterizations

Cyclic voltammetry (CV) measurements were performed using a Gamry 5000E electrochemical test system (Gamry Instruments, USA) in a three-electrode setup. The working electrode was a glassy carbon electrode (GC 130, 3 mm diameter), polished with ~50 nm alumina particles prior to use. A gauze-platinum electrode (0.75 cm × 0.75 cm) and an Ag/AgCl reference electrode (0.197 V vs. SHE), pre-soaked in saturated KCl solution, were used as the counter and reference electrodes, respectively. CV curves were recorded between –1.1 V and –0.5 V at a scan rate of 100 mV·s^{-1} for a series of 5 mM solutions of **15AQS** or **26AQS** at various pH values. Solution pH was measured with a pH meter (pHS-3C, INESA, China) calibrated using standard buffers at pH 4.00, 6.86, and 8.16.

Rotating disk electrode (RDE) experiments were carried out on a PINE system with a 5 mm glassy carbon working electrode, a gauze-platinum counter electrode (0.75 cm × 0.75 cm), and an Ag/AgCl reference electrode (pre-soaked in saturated KCl). The working electrode was rotated at speeds ranging from 600 to 2400 rpm. Linear sweep voltammetry (LSV) was conducted on the Gamry 5000E system at a scan rate of 50 mV·s^{-1} over the potential range of –1.1 V to –0.5 V vs. Ag/AgCl.

The diffusion coefficient (D) was calculated from the slope of the Levich equation:

$$i = 0.620nFAD^{\frac{2}{3}}\omega^{1/2}\nu^{-\frac{1}{6}}c \quad (1)$$

using n = 2, Faraday's constant F = 96485 C·mol^{-1}, electrode area A = 0.196 cm^2, analyte concentration c = 5 × 10^{-6} mol·cm^{-3}, and kinetic viscosity ν = 0.01 cm^2·s^{-1}.

The rate constant (k_0) for 1,5-DHAQ and Cys-DHAQ was derived from the Koutecky–Levich equation:

$$\log i_k = \log(nFcAk_0) + \frac{\alpha nF\eta}{2.303RT} \quad (1)$$

with n = 2, gas constant R = 8.314 J·K^{-1}·mol^{-1}, and temperature T = 293.15 K.

Electrochemical impedance spectroscopy (EIS) of the AORFBs was performed before and after cycling tests using a sinusoidal voltage amplitude of 5 mV over a frequency range of 100 kHz to 0.1 Hz.

All electrochemical tests were performed in a double-jacketed electrolytic cell. The solutions were purged with nitrogen prior to measurements, and the temperature was held constant at 25°C using a circulating water bath.

Permeability measurements

The permeability of **15AQS** across Vmeber-40 membranes was determined using a two-compartment diffusion cell coupled using a UV–Vis spectrometer (756N, INESA Co. Ltd). The left compartment was charged with 0.5 M **15AQS** in 1.0 M NaOH, while the right compartment contained an equal volume of 1.0 M NaOH as the receiving solution. Both compartments were continuously stirred throughout the experiment.

The concentration of **15AQS** in the receiving compartment was monitored at designated time intervals by measuring its UV-Vis absorbance, which was converted to concentration using a pre-established absorbance–concentration calibration curve. The permeability coefficient (P) of **15AQS** was then calculated based on Fick's diffusion law according to the following equation:

$$P = -\frac{\ln\left(1 - \frac{2C_t}{C_0}\right)\left(\frac{V_0 l}{2A}\right)}{t} \quad (1)$$

Here, P is the permeability (cm^2·s^{-1}), A is the effective membrane area (0.75 cm^2), c_t is the concentration in the receiving

compartment at time t (mol·L^{-1}), c_0 is the initial concentration in the source compartment (0.5 mol·L^{-1}), V_0 is the volume of each reservoir (25 cm^3), l is the membrane thickness (41.5 μm for Vmembr-40).

Redox flow battery tests

Polarization curves were obtained at different states of charge (SOC) by linear sweep voltammetry (LSV) at a scan rate of 50 mV s^{-1} from 1.7 V to 0.4 V using a Gamry 5000E electrochemical workstation. Before the test, the cell was charged to the desired SOC. The fully charged state at 1.7 V was defined as 100% SOC.

Cycling tests were performed under the following electrolyte configurations:

- For 0.05 M **15AQS**, the negolyte consisted of 10 mL of 0.05 M **15AQS** in 1 M NaCl, 0.01 M NaCl, and 1 M NaOH, while the posolyte was 100 mL of 0.075 M $Na_4[Fe(CN)_6]$ in the same supporting electrolyte.
- For 0.1 M **15AQS** or **26AQS**, the negolyte was 10 mL of 0.1 M active material in 1 M NaOH, and the posolyte was 100 mL of 0.15 M $Na_4[Fe(CN)_6]$ in 1 M NaOH.
- For 0.5 M **15AQS**, the negolyte was 10 mL of 0.5 M **15AQS** in 1 M NaOH, and the posolyte was 100 mL of 0.5 M $Na_4[Fe(CN)_6]$ in 1 M NaOH.

All galvanostatic cycling was carried out using a 5V/6A battery test station (Wuhan Land Instruments, China) between cutoff voltages of 1.7 V and 0.4 V. Current densities were set at 60 mA·cm^{-2} for the 0.05 M **15AQS** system and 100 mA·cm^{-2} for the 0.1 M and 0.5 M systems for long cycle test.

Unless otherwise specified, all AORFB tests were conducted in a nitrogen-filled glove box at room temperature (~25 °C).

Computational details

All calculations in this work were performed using Gaussian 16 program package[2]. Full geometry optimizations were performed to locate all the stationary points, using the B3LYP[3] with the 6-311+G(d,p)[4-5]. Dispersion corrections were computed with Grimme's D3(BJ) method in optimization[6-8]. The self-consistent reaction field (SCRF) method based on the universal solvation model SMD[9] was adopted to evaluate the effect of solvent. Frequency analysis was carried out to verify the optimized geometry to be a minimum or transition structure and to obtain the thermal corrections for the Gibbs free energy. Single-point energy calculations were obtained at the B3LYP-D3 with 6-311+G(d,p). Harmonic vibrational frequency was performed at the same level to guarantee that there is no imaginary frequency in the molecules, i.e. they locate on the minima of potential energy surface. Convergence parameters of the default threshold were retained (maximum force within 4.5×10^{-4} Hartrees/Bohr and root mean square (RMS) force within 3.0×10^{-4} Hartrees/Radian) to obtain the optimized structure. The optimal structure was identified given that all calculations for structural optimization were successfully converged within the convergence threshold of no imaginary frequency, during the process of vibration analysis.

Classic molecular dynamics simulations were carried out to investigate the mixed solution from the atomic level. Two Bulk cases (System1, System2) were built for Molecular Dynamic simulations.

Case System1 contains 50 **15AQS**, 100 NaOH, 5560 H_2O molecules. Case System2 contains 50 **26AQS**, 100 NaOH, 5560 H_2O molecules. The initial configurations systems were constructed through the software of PACKMOL[10], all the molecules were randomly inserted in a cubic simulation box.

The OPLSAA force field[11-13] was employed to describe the molecules. CM5 charge integrated in AuToFF web server[14]. The molecular force field is consisted of nonbonded and bonded interaction. The nonbonded interaction contains van deer Waals and electrostatic interaction, which is described by the Equation 1 and Equation 2, respectively.

$$E_{Lj}(r_{ij}) = 4\varepsilon_{ij}\left(\left(\frac{\sigma_{ij}}{r_{ij}}\right)^{12} - \left(\frac{\sigma_{ij}}{r_{ij}}\right)^{6}\right) \quad (1)$$

$$E_c(r_{ij}) = \frac{q_i q_j}{4\pi\varepsilon_0\varepsilon_r r_{ij}} \quad (1)$$

In the equation, q_i、q_j are atomic charge, r_{ij} is the distance between atoms, σ is the atomic diameter, ε is the atomic energy parameter.

For different kinds of atoms, the geometric mix rules were adopted for vdW interactions, which is following the Equation 3. The cutoff distance of vdW and electronic interactions was set to 1.2 nm, and the PME method was employed to calculate long-range electrostatic interactions.

$$\sigma_{ij} = (\sigma_{ii} * \sigma_{jj})^{\frac{1}{2}}; \varepsilon_{ij} = (\varepsilon_{ii} * \varepsilon_{jj})^{\frac{1}{2}} \quad (1)$$

For the simulation, an energy minimization was firstly employed to relax the simulation box. Then, an isothermal-isobaric (NPT) ensemble with a 1.0 fs time step is employed to optimized the simulation box, where the temperature is set to 298.15 K and the pressure is set to 1.0 atm. The temperature and pressure are kept via the Nose-Hoover thermostat and Parrinello-Rahman barostat, respectively. The NPT optimization time was set to 12.0 ns, which is enough long to obtain a stable box size. Then, an other NPT with a 1.0 fs time step and time was set to 1.0 ns, to record the trajectory for subsequent analysis. The atomic trajectories every 1000 femtoseconds. where the temperature is set to 298.15 K.

In all the MD simulation, the motion of atoms was described by classical Newton's equation, which was solved using the velocity-Verlet algorithm. And all the Molecular Dynamic simulations were performed by using GROMACS 2022.2 package[15]. The results were analyzed using Gromacs tool-suites, the Visual Molecular Dynamic program (VMD)[16], and additional scripts written by the researchers.

The calculation of H-bond is based on the geometrical configuration that the distance of two O is <3.5 Å and the angle of O-H···O is <30°.

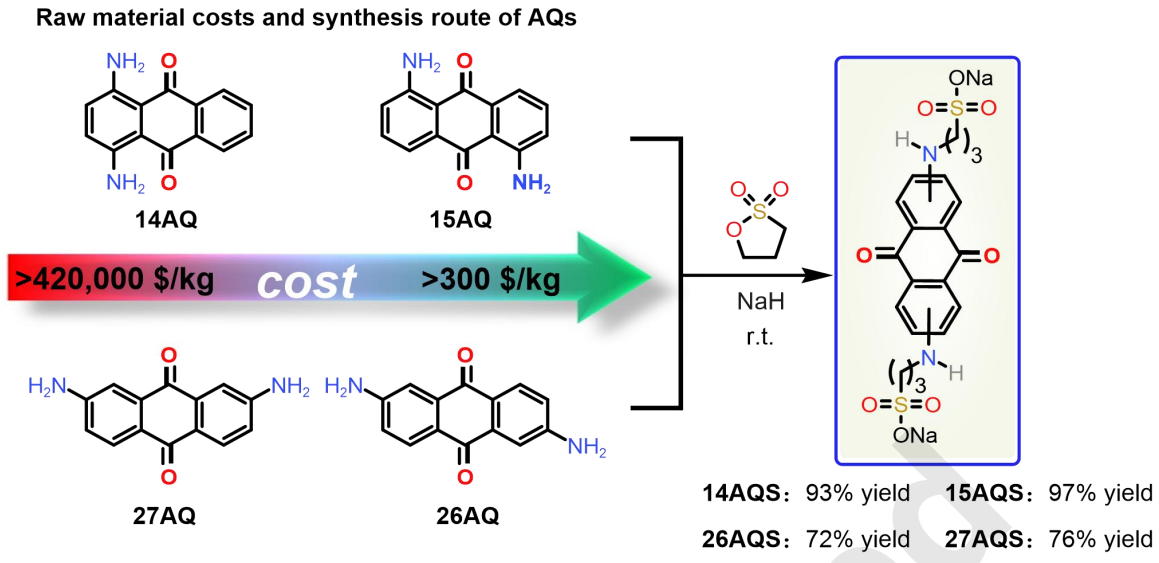

Figure S1 Raw material costs and synthesis route of AQs

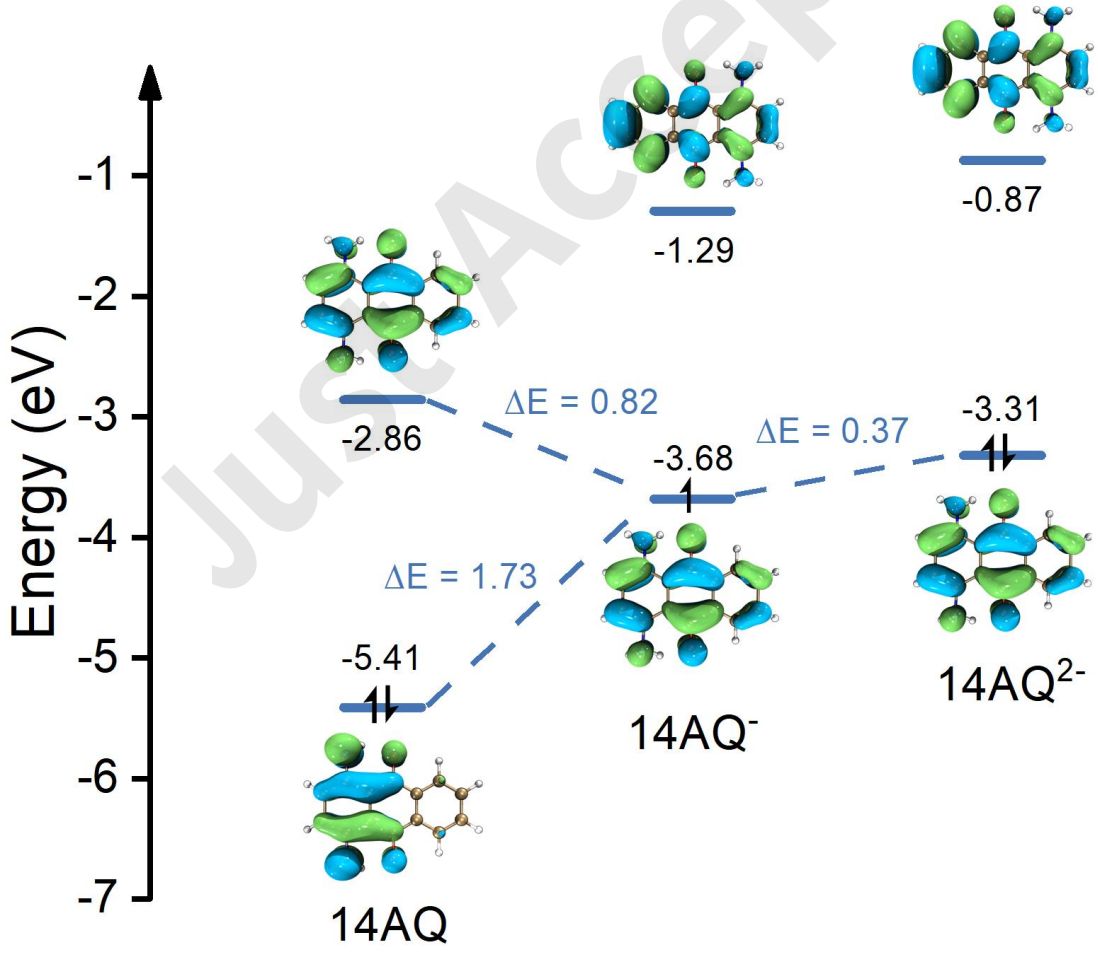

Figure S2 HOMO/LUMO energy level distributions of **14AQ**, **14AQ**$^{-}$ and **14AQ**$^{2-}$

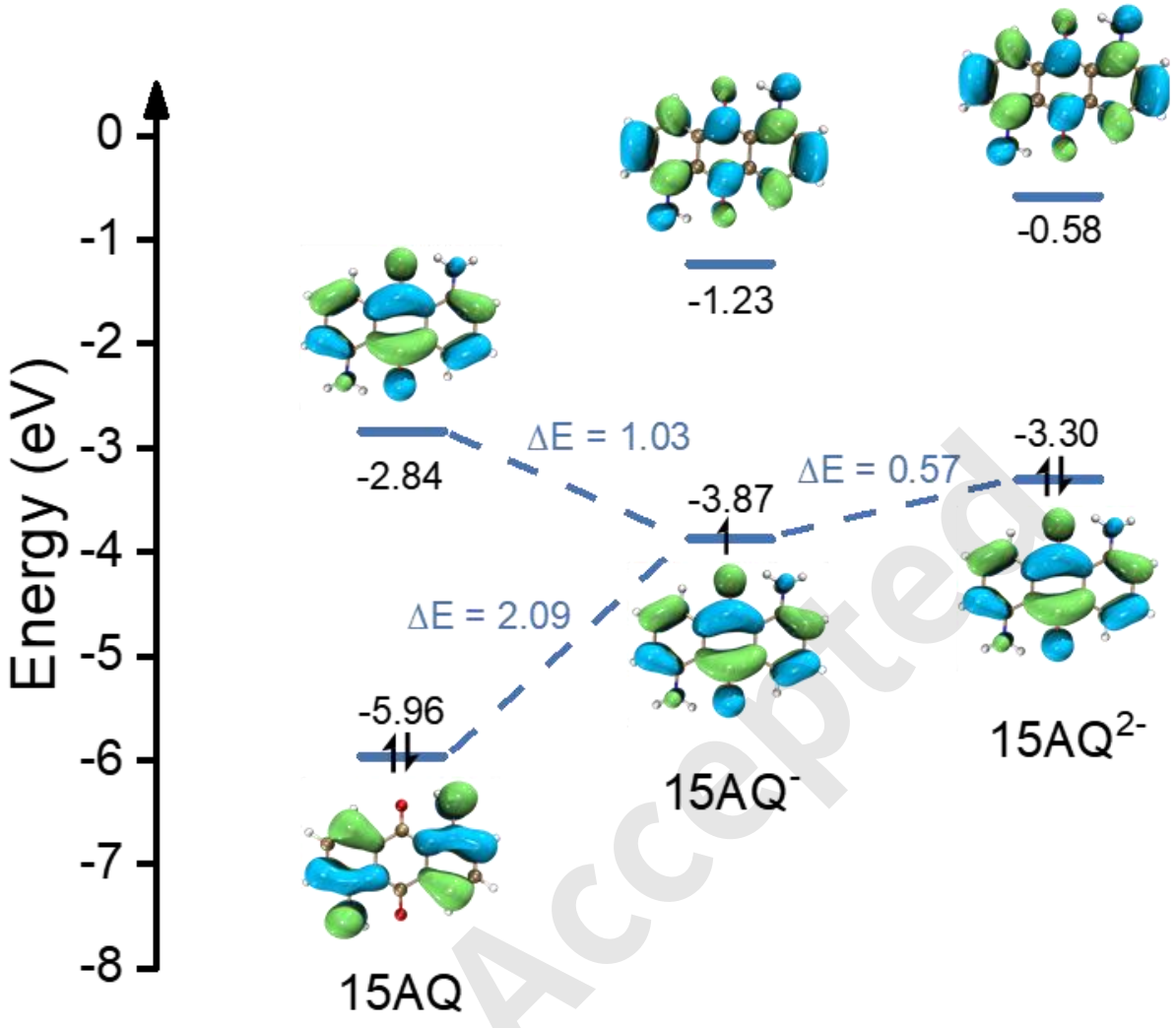

Figure S3 HOMO/LUMO energy level distributions of **15AQ**, **15AQ**$^{-}$ and **15AQ**$^{2-}$

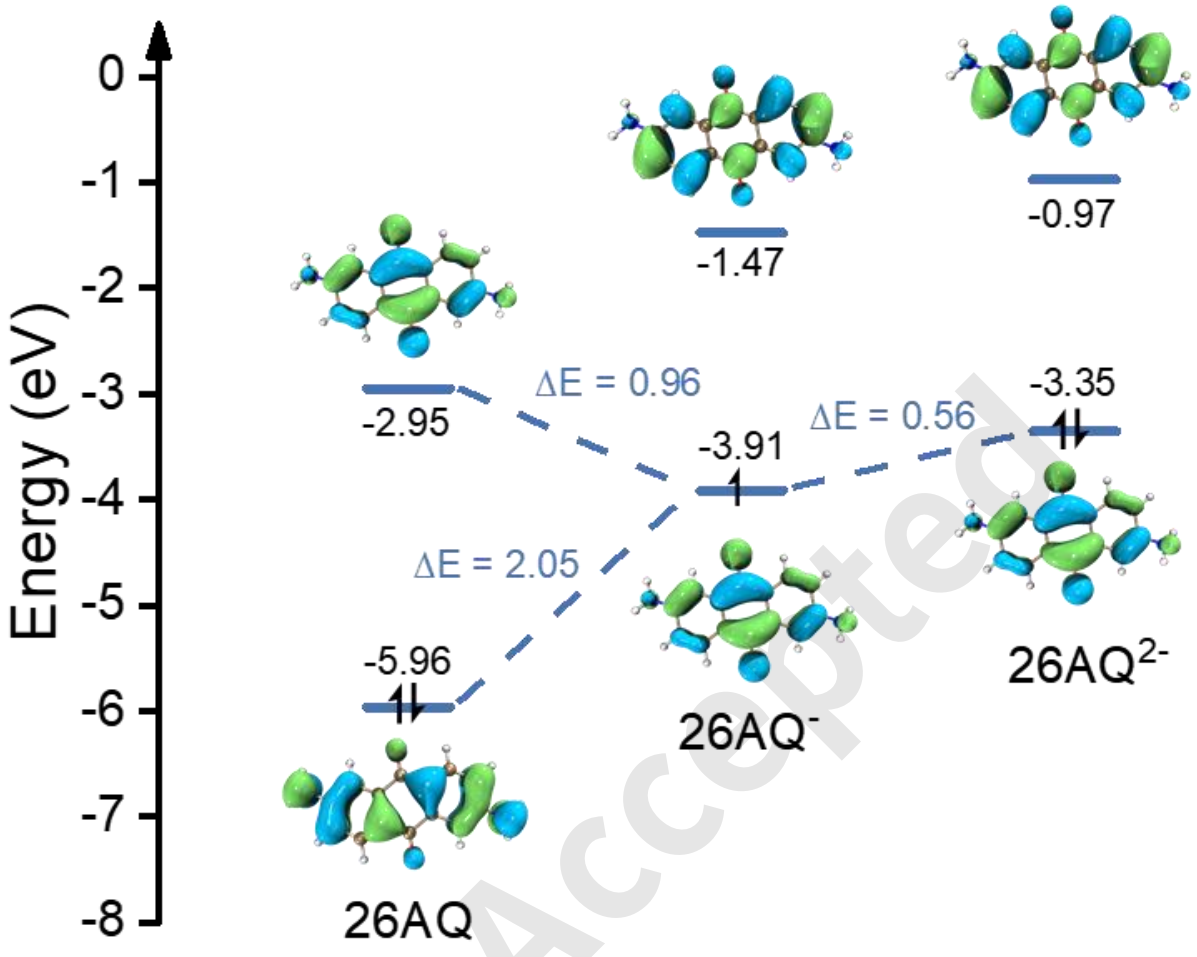

Figure S4 HOMO/LUMO energy level distributions of **26AQ**, **26AQ**$^{-}$ and **26AQ**$^{2-}$

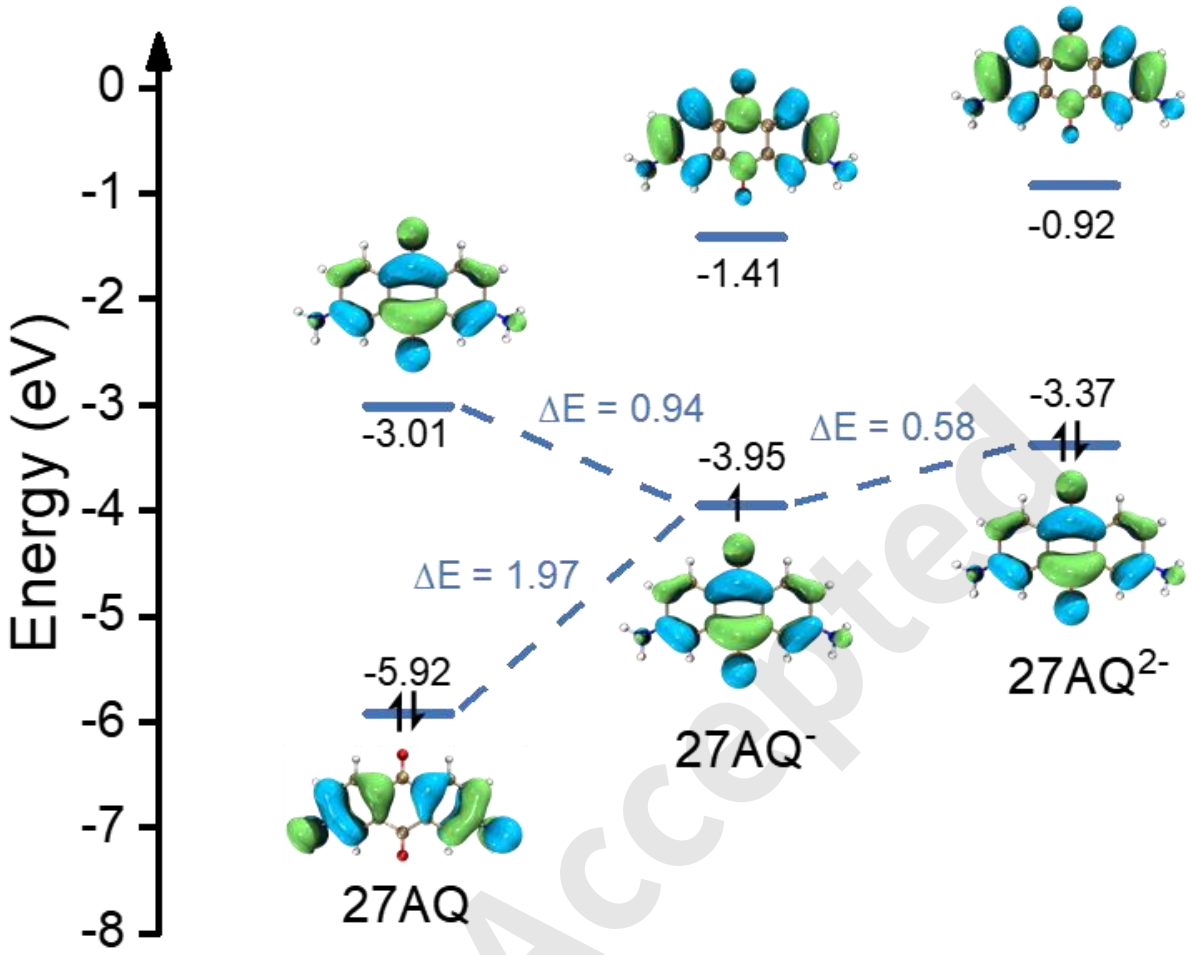

Figure S5 HOMO/LUMO energy level distributions of **27AQ**, **27AQ**$^{-}$ and **27AQ**$^{2-}$

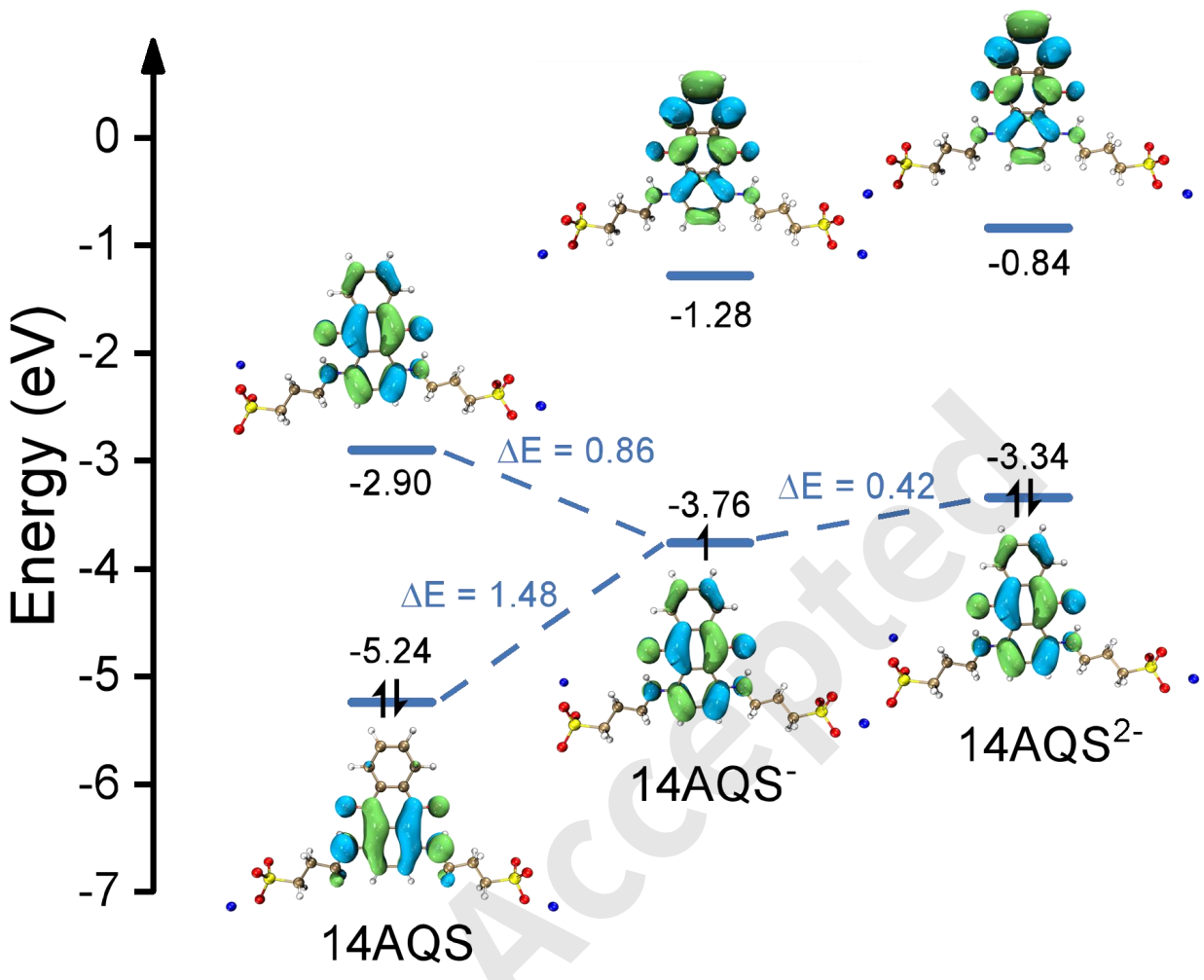

Figure S6 HOMO/LUMO energy level distributions of **14AQS**, **14AQS**$^{-}$ and **14AQS**$^{2-}$

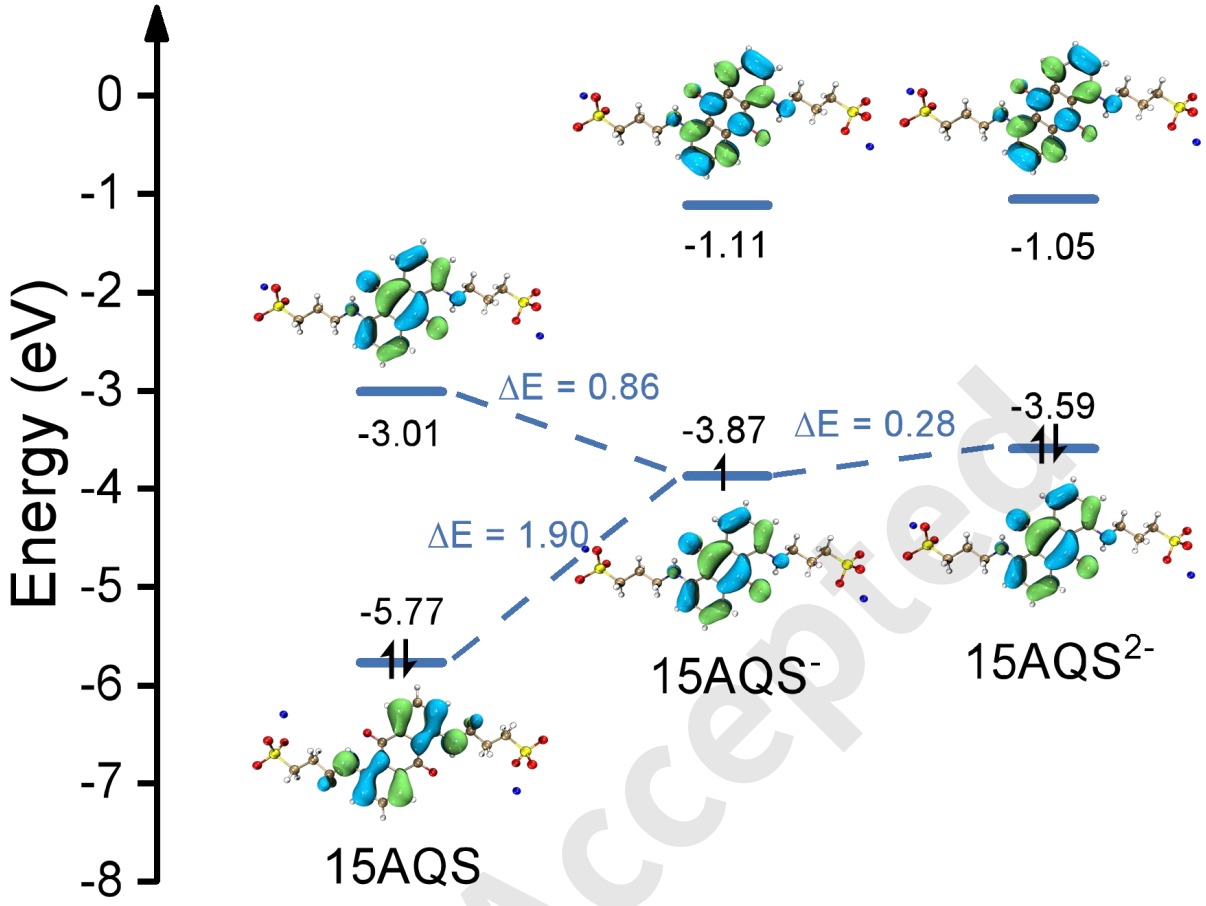

Figure S7 HOMO/LUMO energy level distributions of **15AQS**, **15AQS**$^{-}$ and **15AQS**$^{2-}$

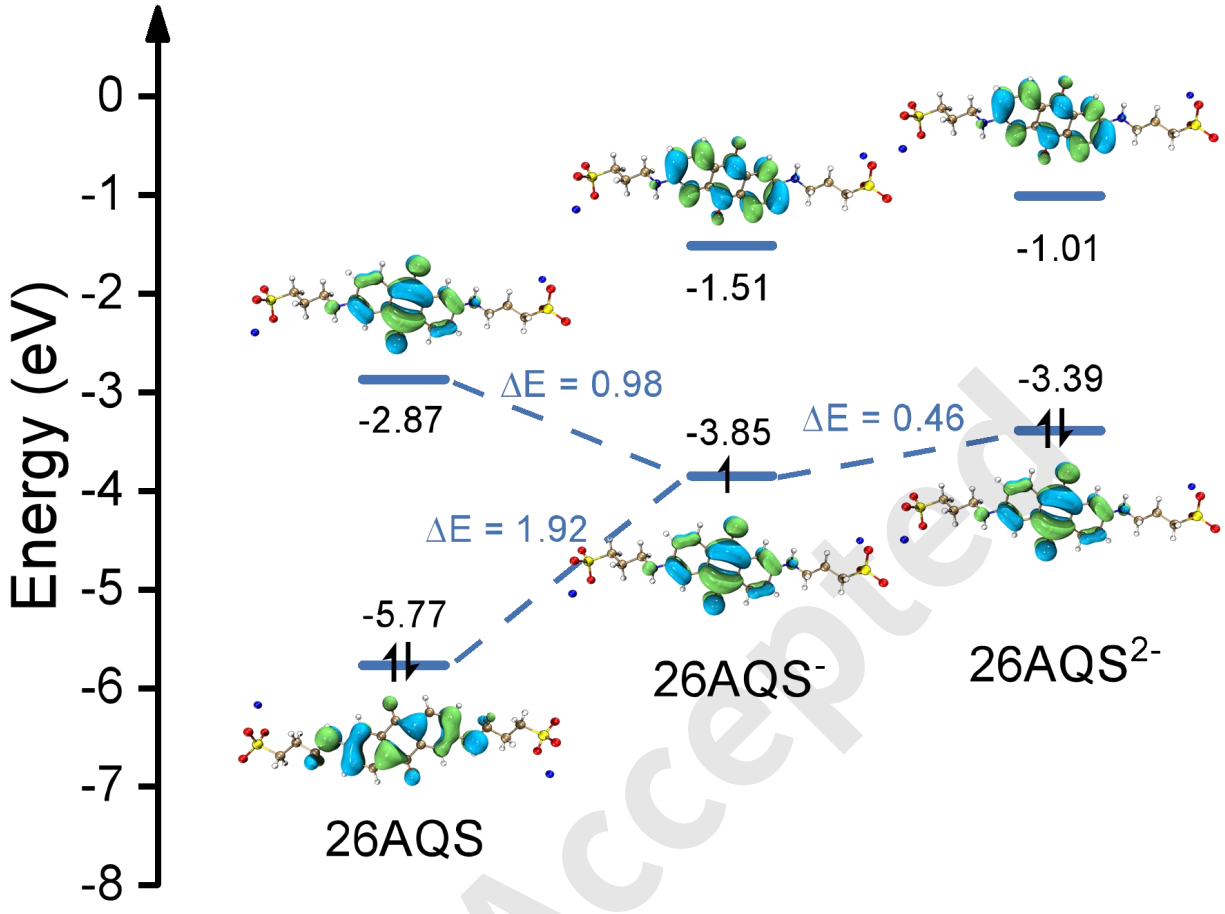

Figure S8 HOMO/LUMO energy level distributions of **26AQS**, **26AQS**$^{-}$ and **26AQS**$^{2-}$

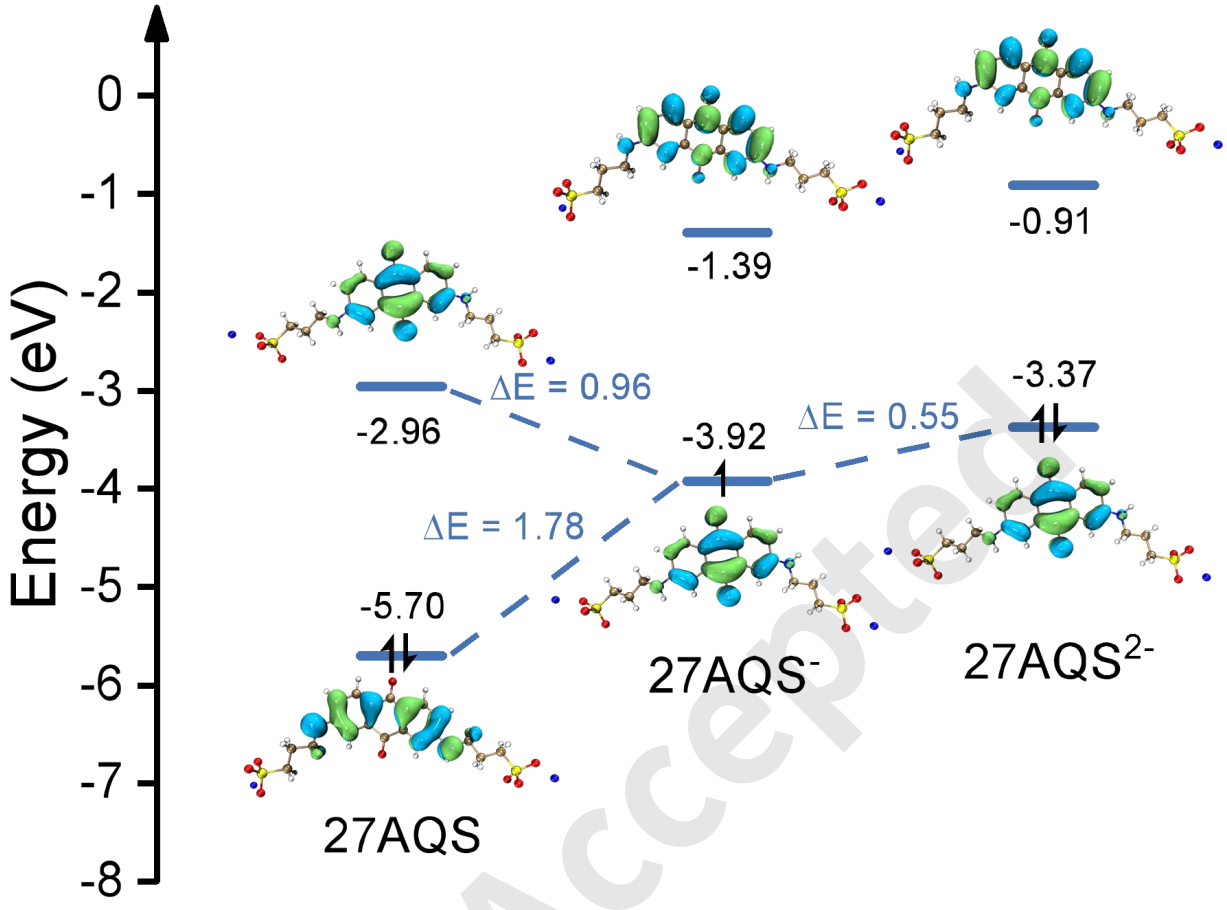

Figure S9 HOMO/LUMO energy level distributions of **27AQS**, **27AQS**$^{-}$ and **27AQS**$^{2-}$

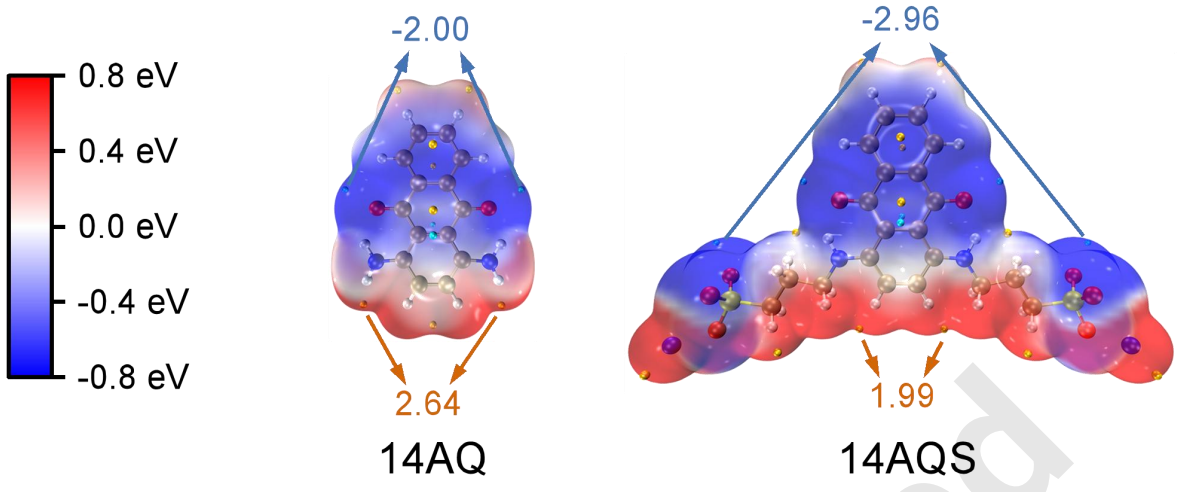

Figure S10 Electrostatic potential maps (ESP) of **14AQ** and **14AQS.** The local minima and maxima of the electrostatic potential (ESP) on the surface are respectively marked by cyan and orange spheres.

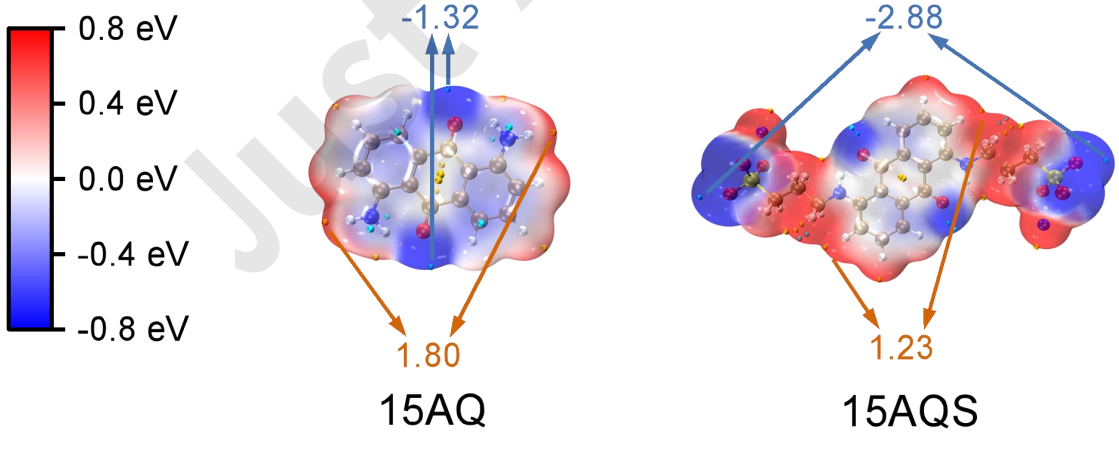

Figure S11 Electrostatic potential maps (ESP) of **15AQ** and **15AQS.** The local minima and maxima of the electrostatic potential (ESP) on the surface are respectively marked by cyan and orange spheres.

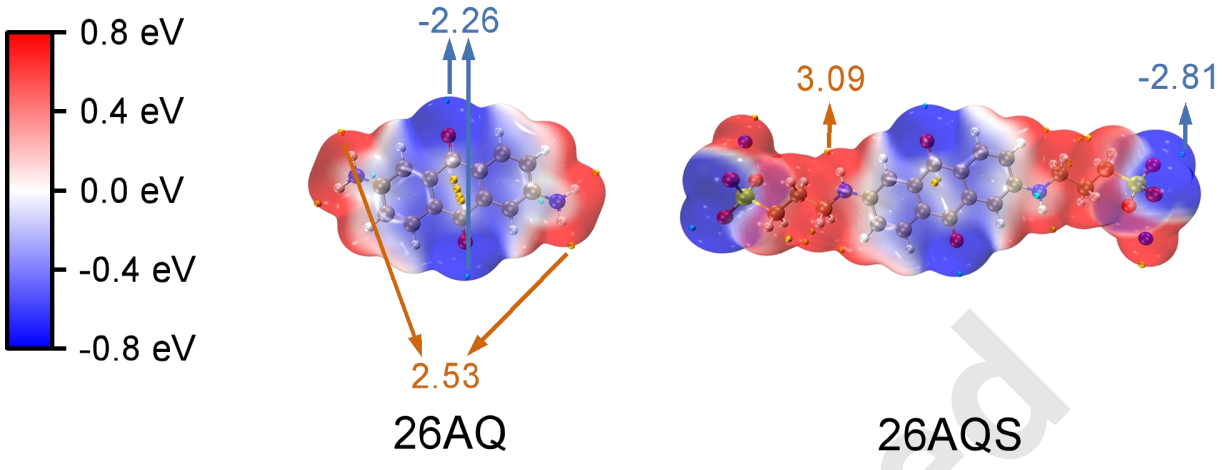

Figure S12 Electrostatic potential maps (ESP) of **26AQ** and **26AQS.** The local minima and maxima of the electrostatic potential (ESP) on the surface are respectively marked by cyan and orange spheres.

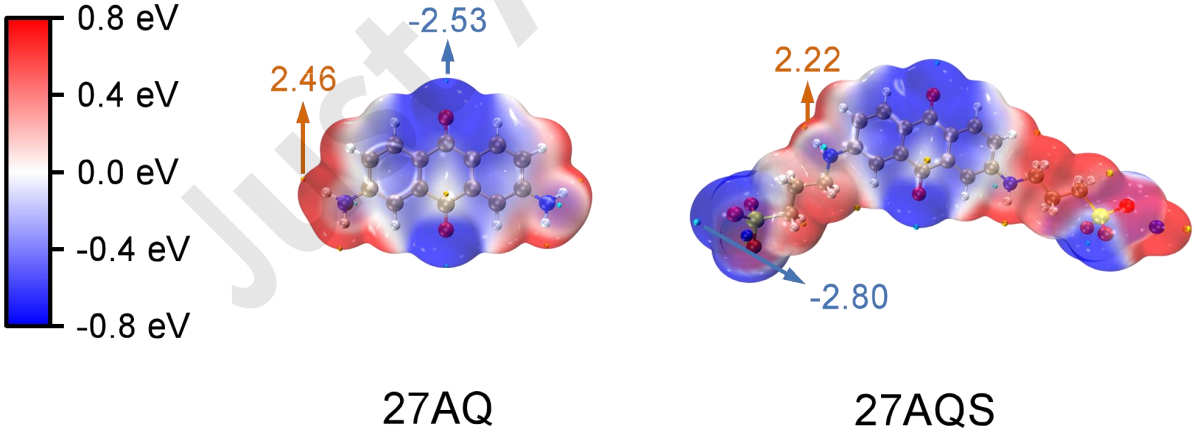

Figure S13 Electrostatic potential maps (ESP) of **27AQ** and **27AQS.** The local minima and maxima of the electrostatic potential (ESP) on the surface are respectively marked by cyan and orange spheres.

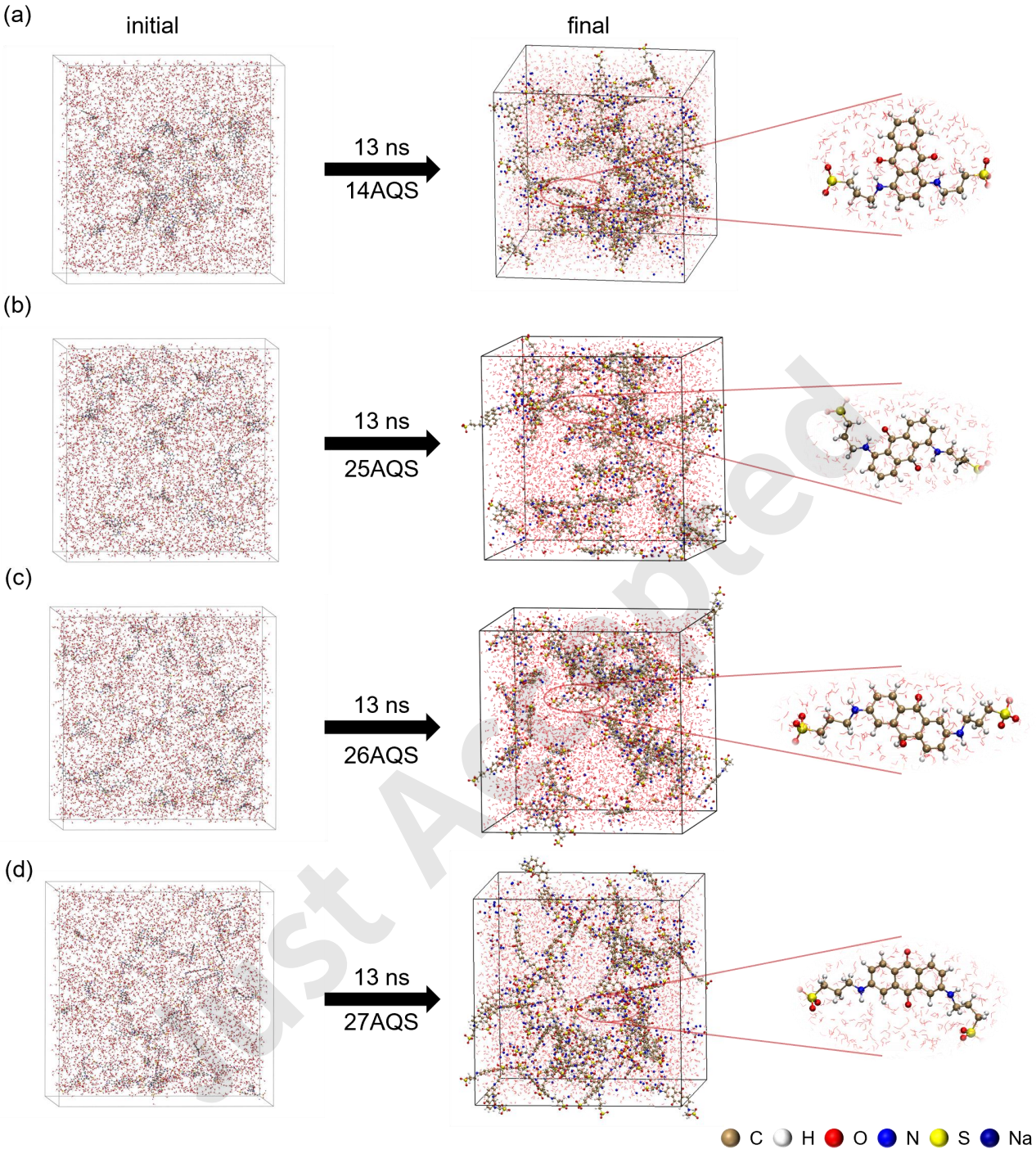

Figure S14 MD simulation snapshots and the hydration schematic diagrams of AQs. (a)**14AQS**; (b)**15AQS**;(c)**26AQS** and (d)**27AQS**.

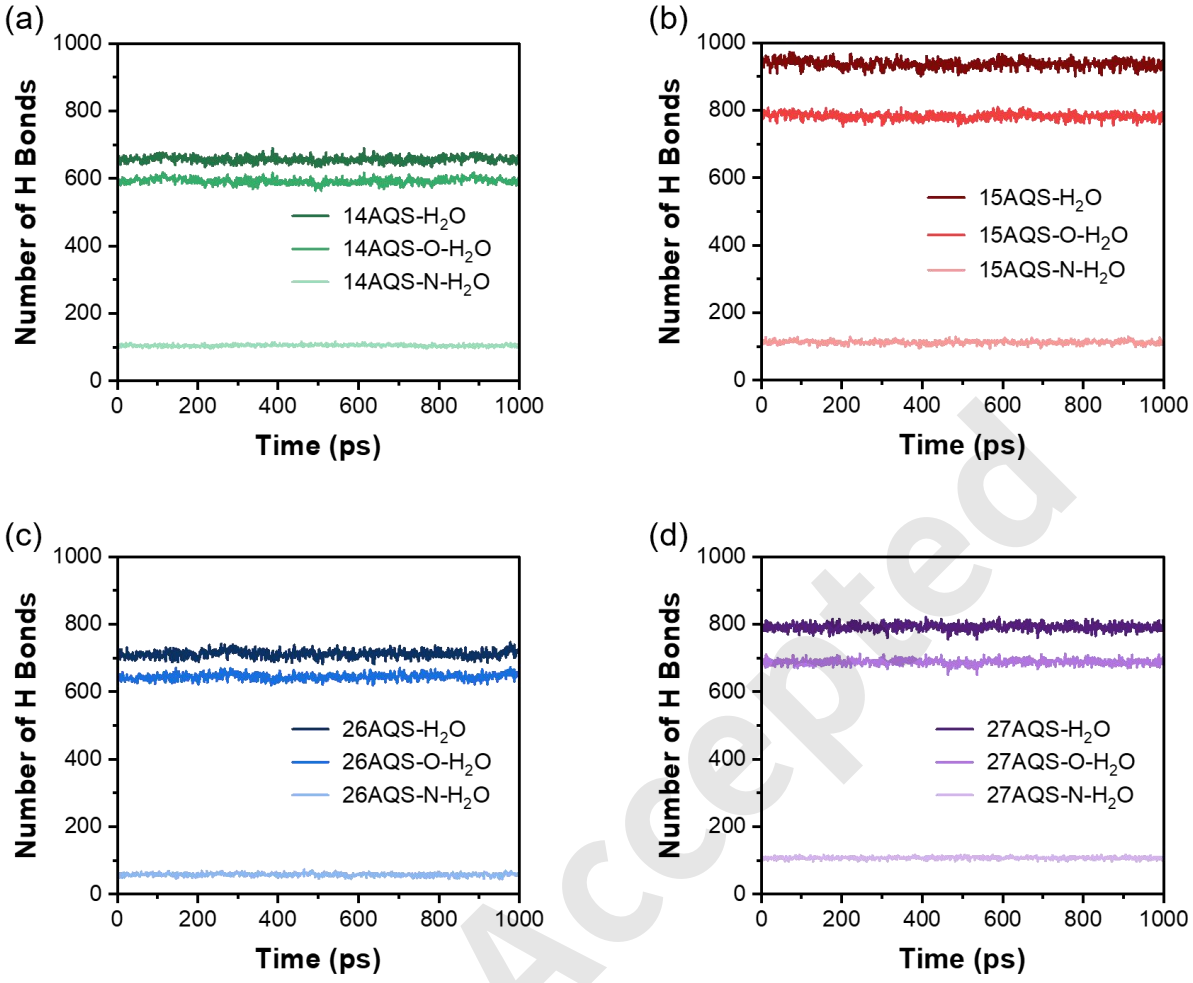

Figure S15 Results from MD simulations show the time evolution and optimized count of hydrogen bonds formed around the (a)**14AQS**; (b)**15AQS;**(c)**26AQS** and (d)**27AQS**.

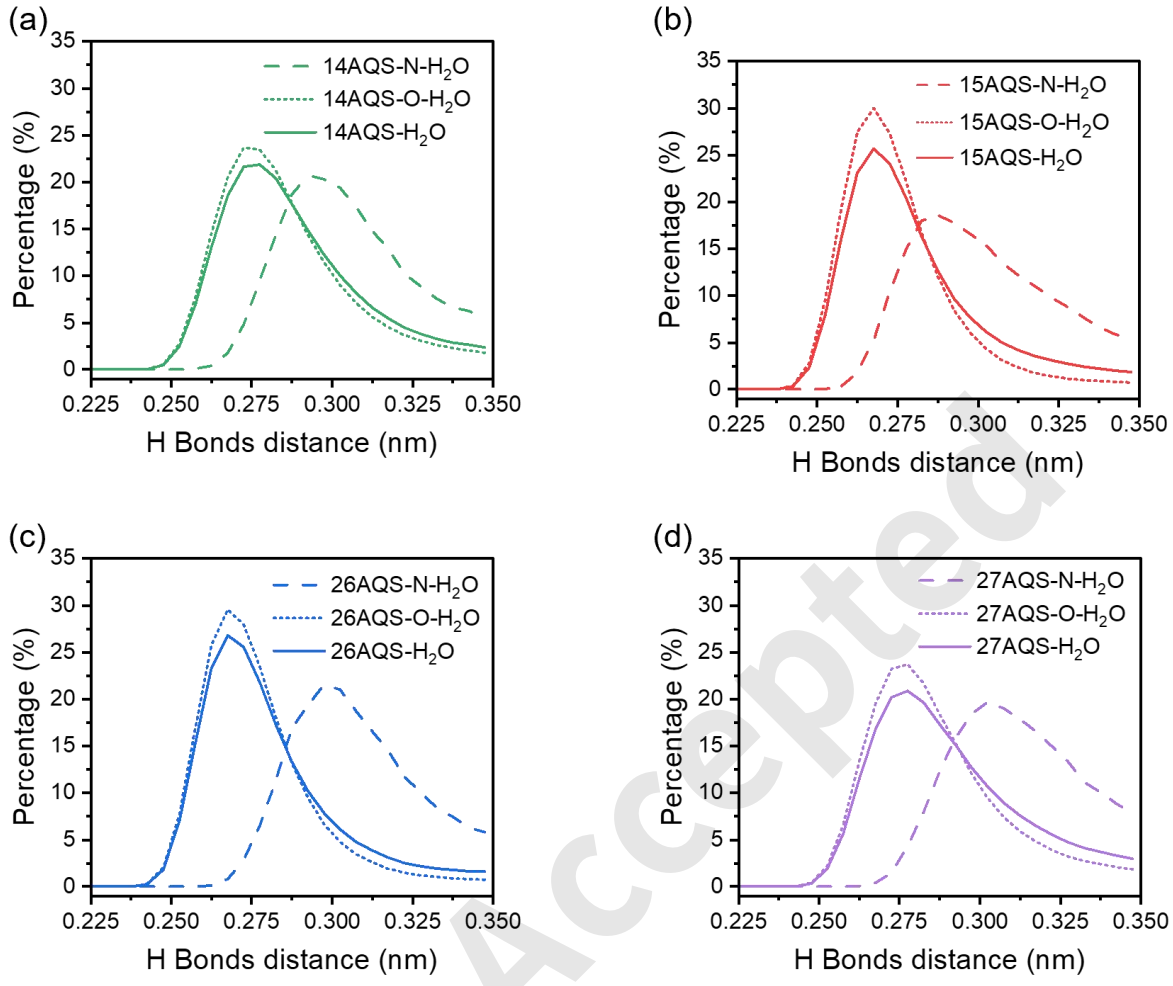

Figure S16 Results from MD simulations show the time evolution and the distribution of H-bonding distances. (a)**14AQS**; (b)**15AQS;**(c)**26AQS** and (d)**27AQS**.

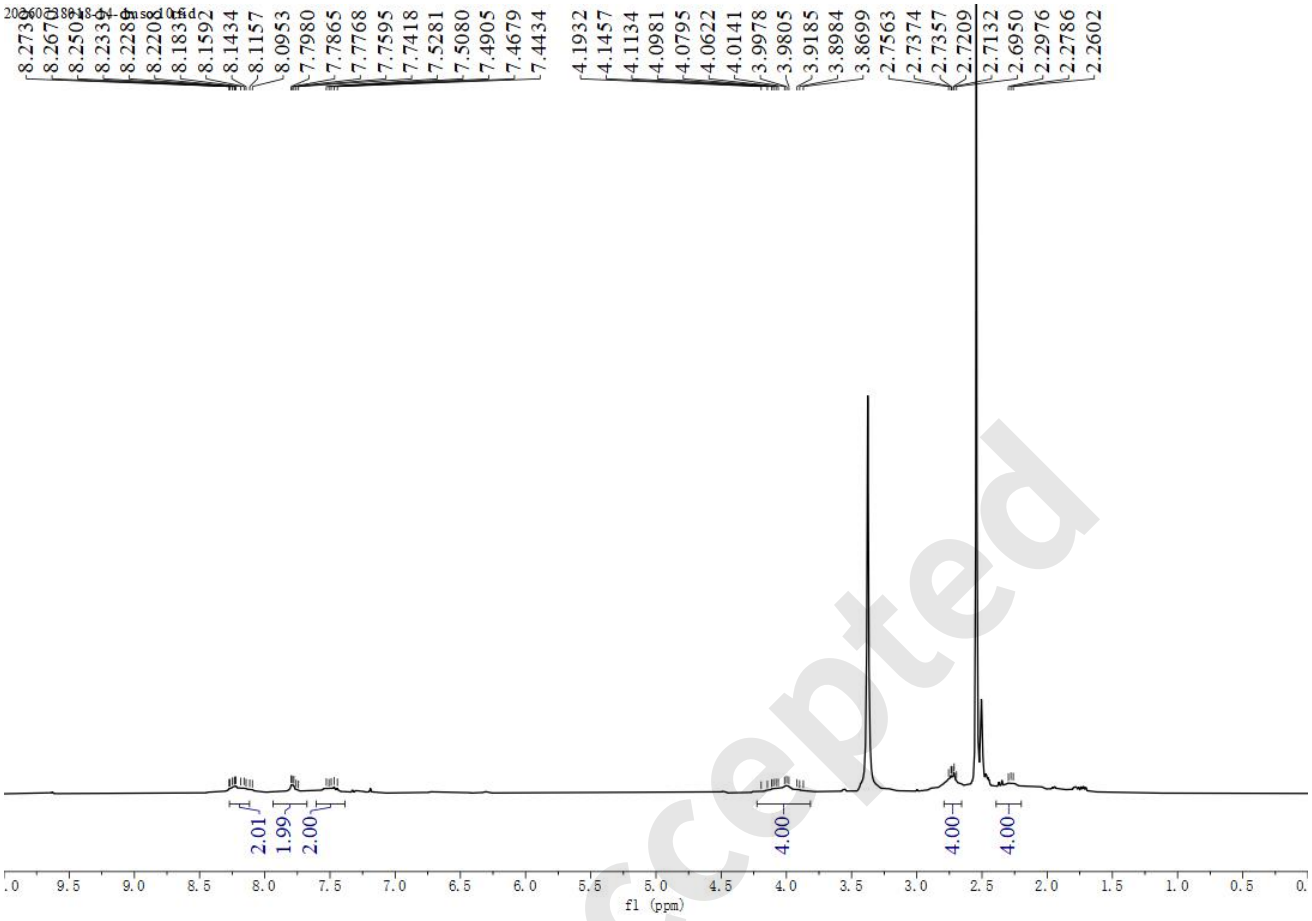

Figure S17 ^{1}H NMR (400 MHz, DMSO-d_6) spectrum of **14AQS**

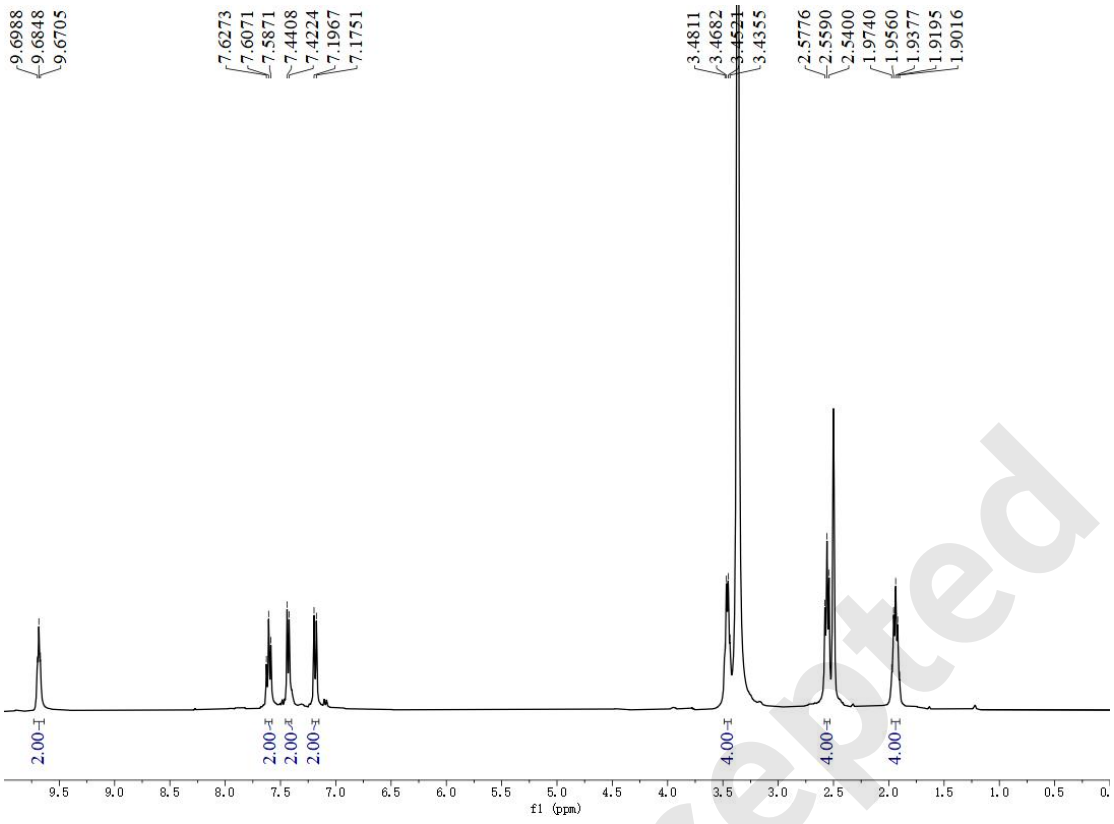

Figure S18 ^{1}H NMR (400 MHz, DMSO-d_6) spectrum of **15AQS**

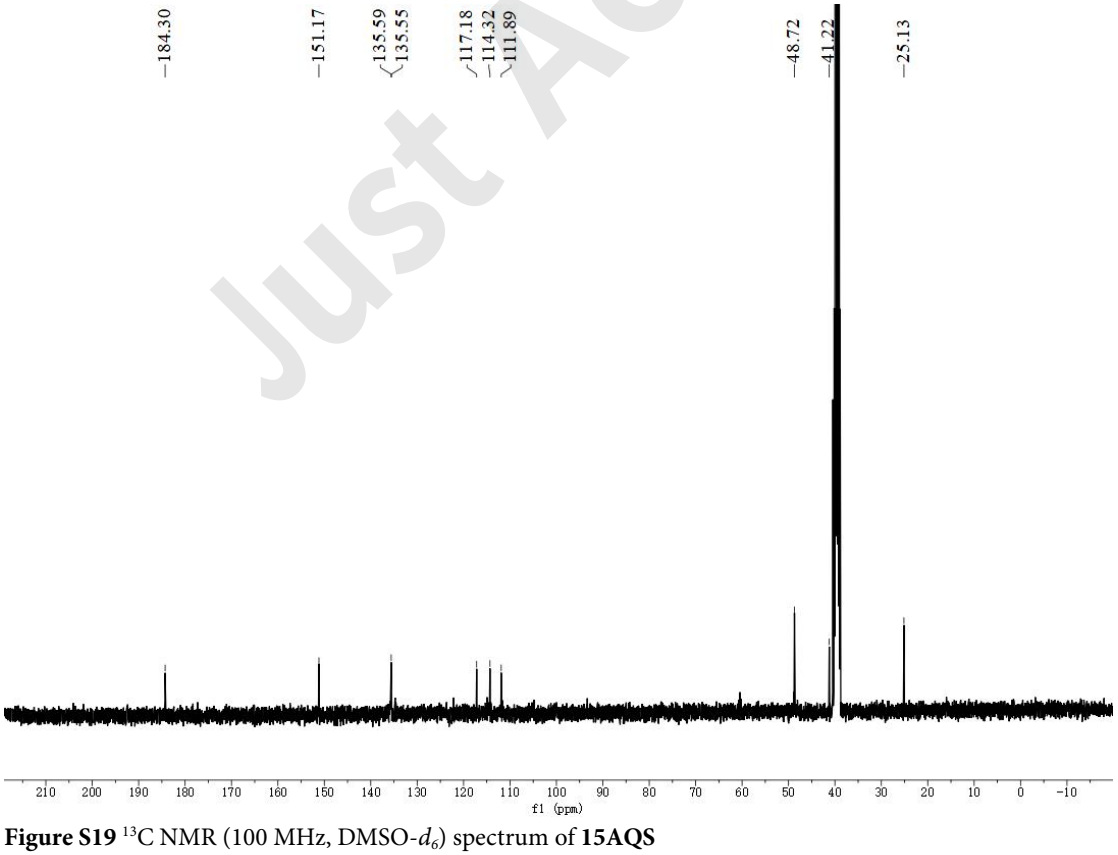

Figure S19 ^{13}C NMR (100 MHz, DMSO-d_6) spectrum of **15AQS**

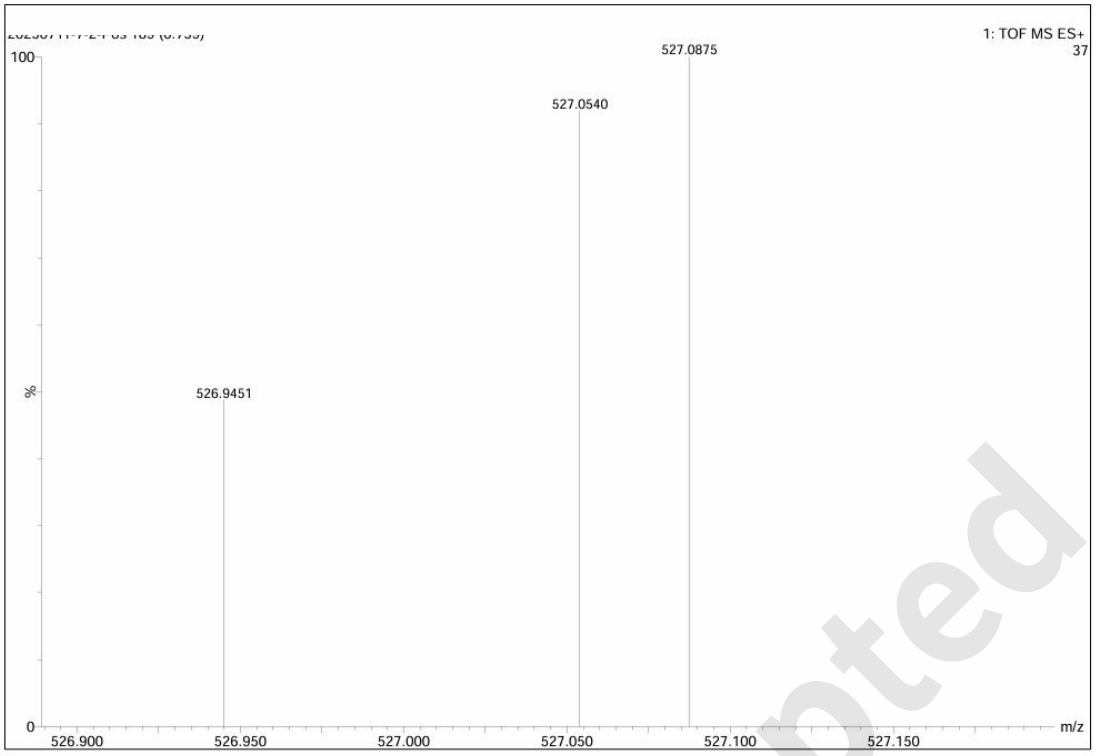

Figure S20 HRMS spectrum of **15AQS**

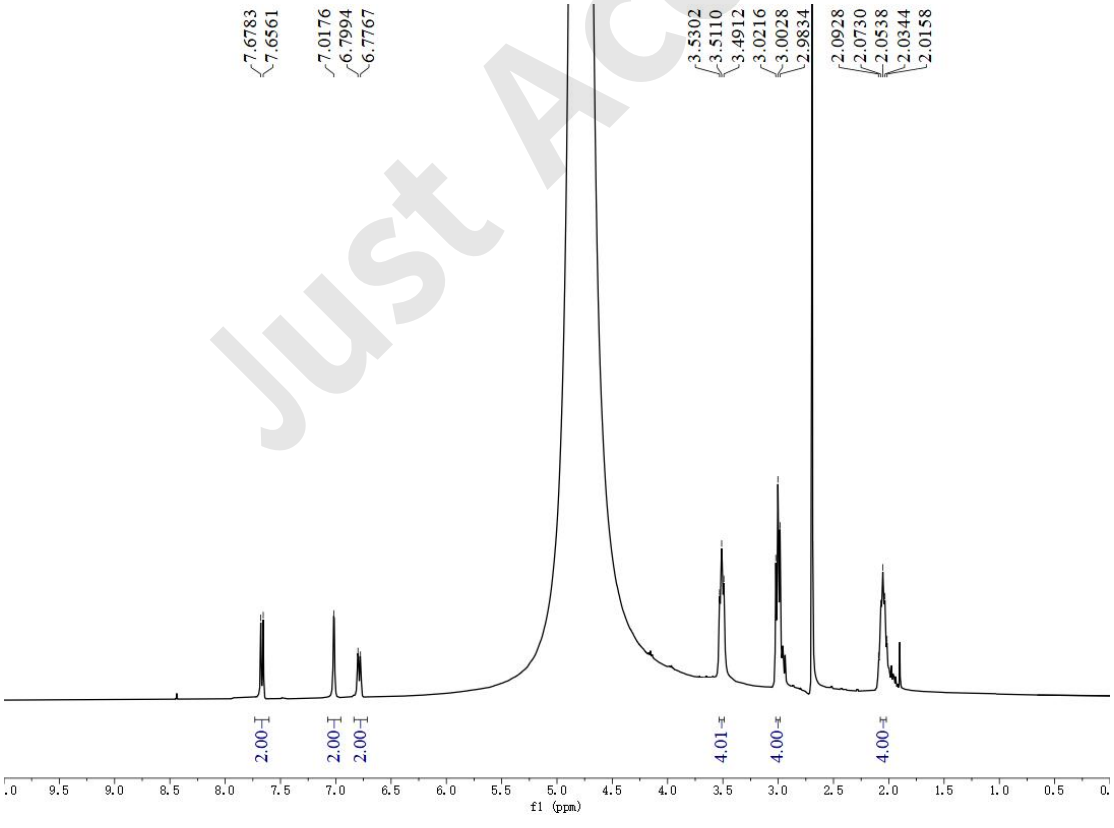

Figure S21 ^{1}H NMR (400 MHz, D_2O) spectrum of **26AQS**

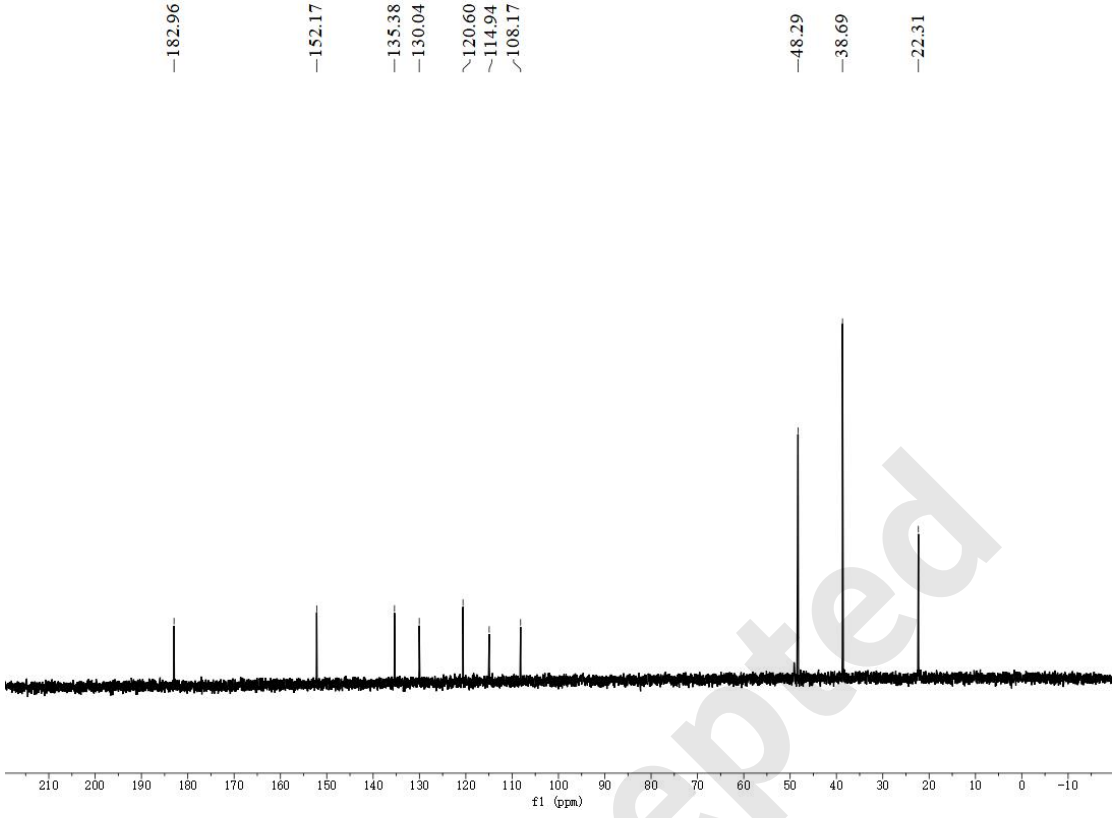

Figure S22 ^{13}C NMR (100 MHz, D_2O) spectrum of **26AQS**

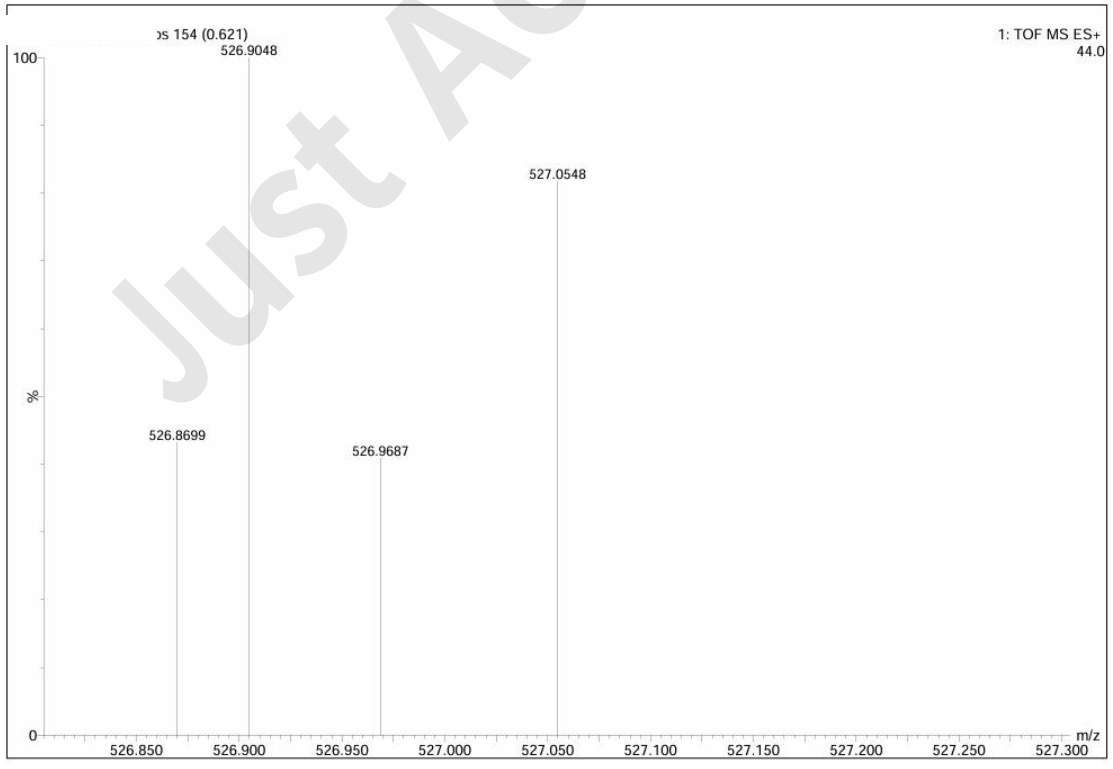

Figure S23 HRMS spectrum of **26AQS**

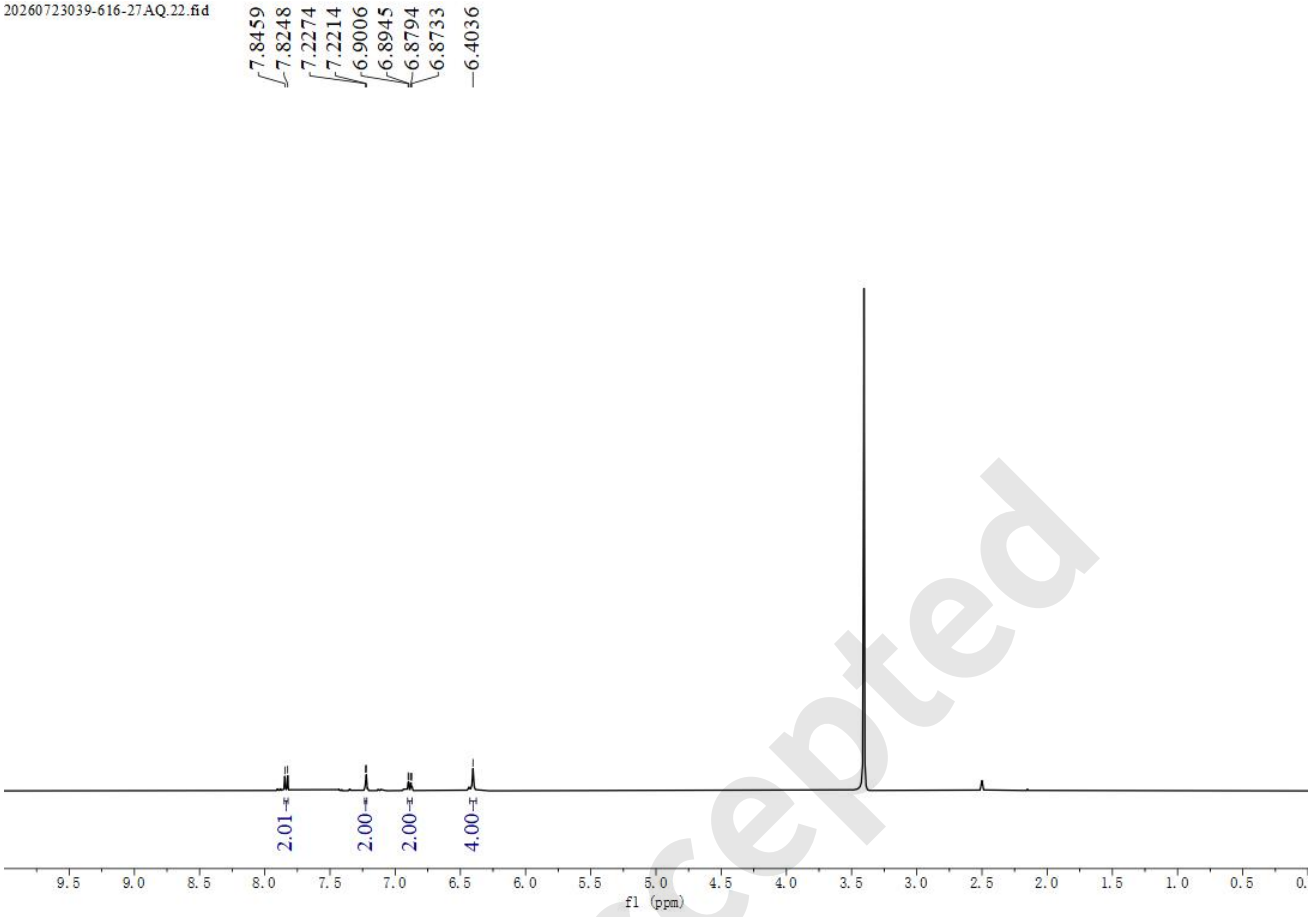

Figure S24 ^{1}H NMR (400 MHz, DMSO-d_6) spectrum of **27AQ**.

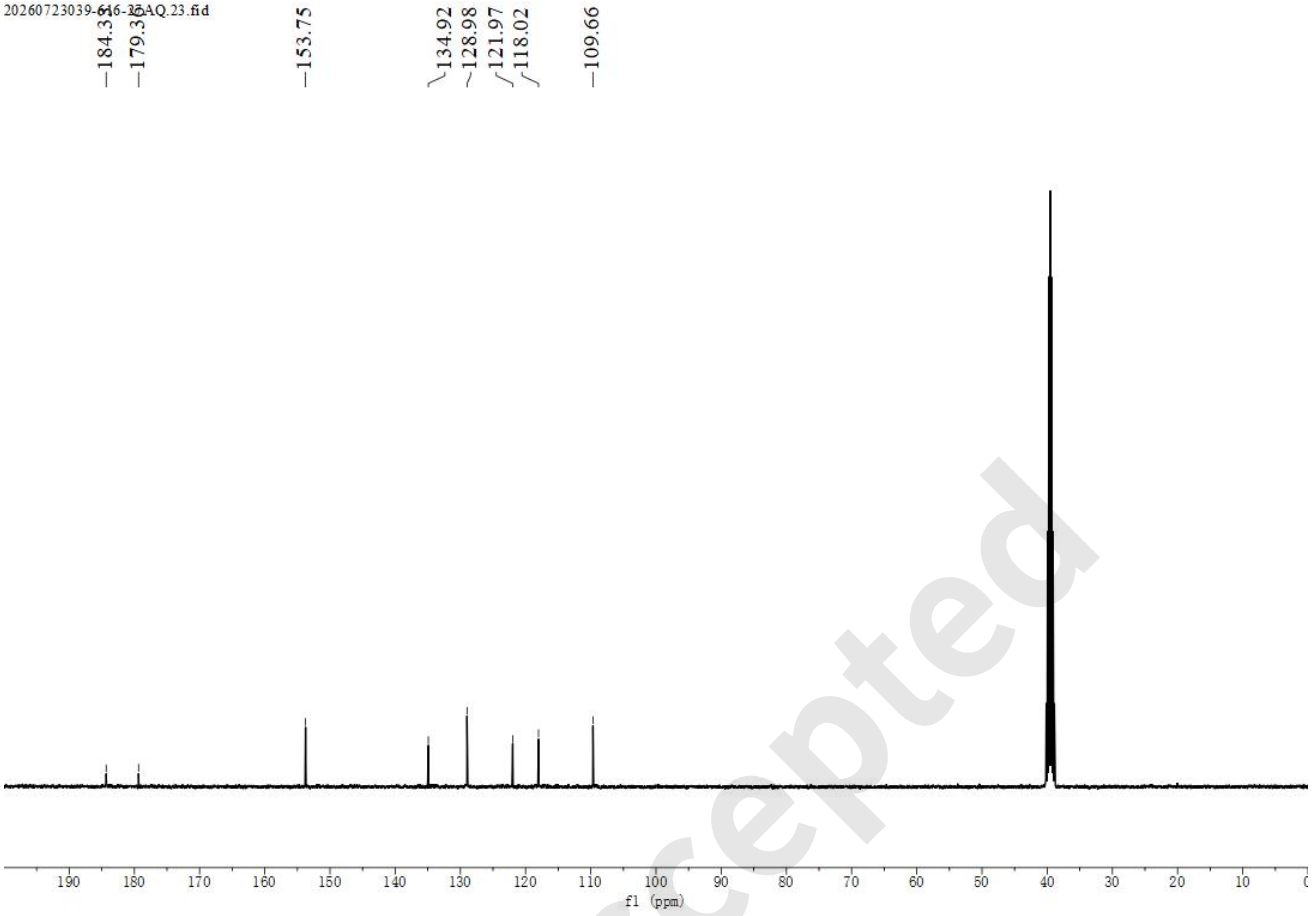

Figure S25 ^{13}C NMR (100 MHz, DMSO-d_6) spectrum of **27AQ**.

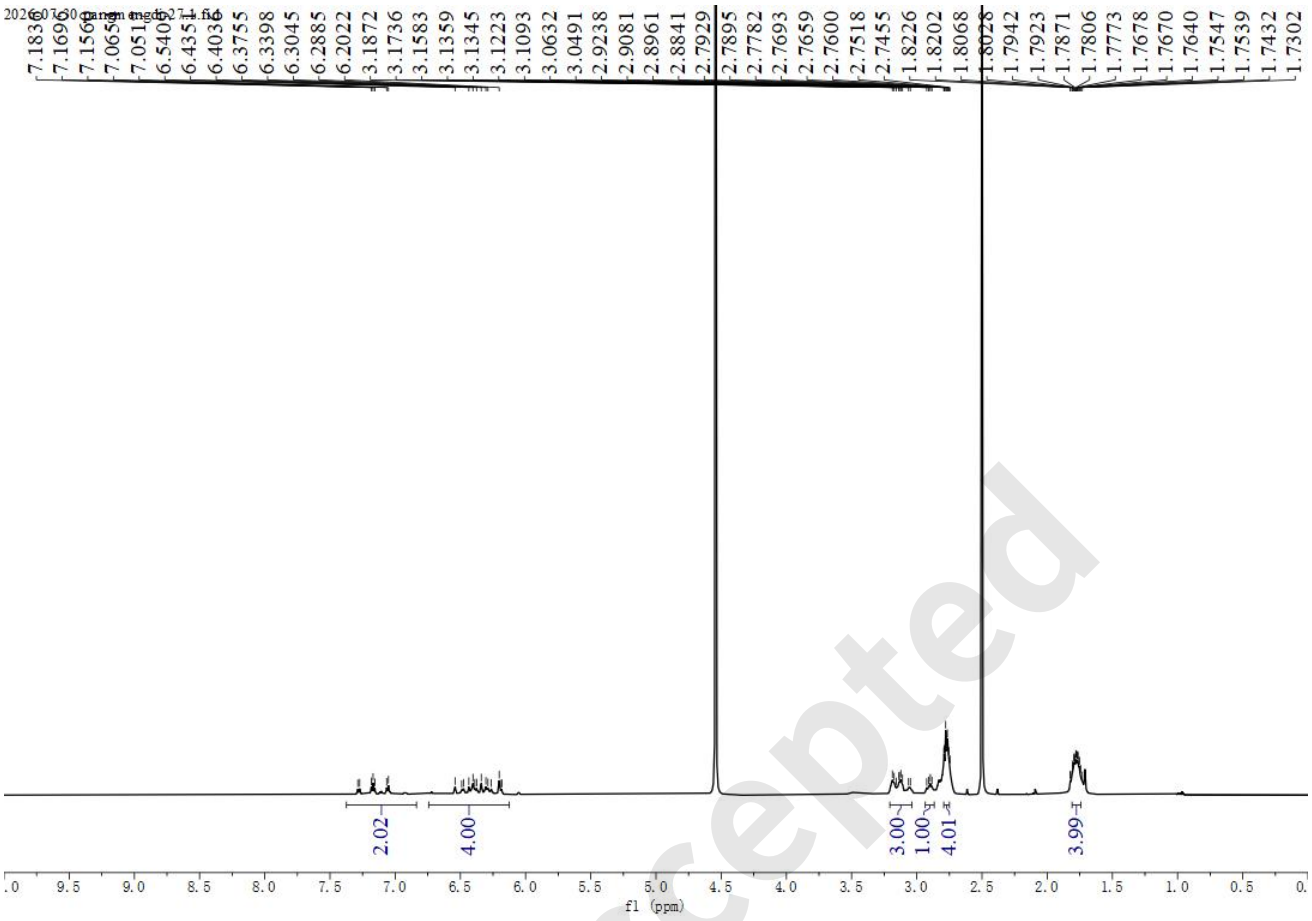

Figure S26 ^{1}H NMR (400 MHz, D_2O) spectrum of **27AQS**

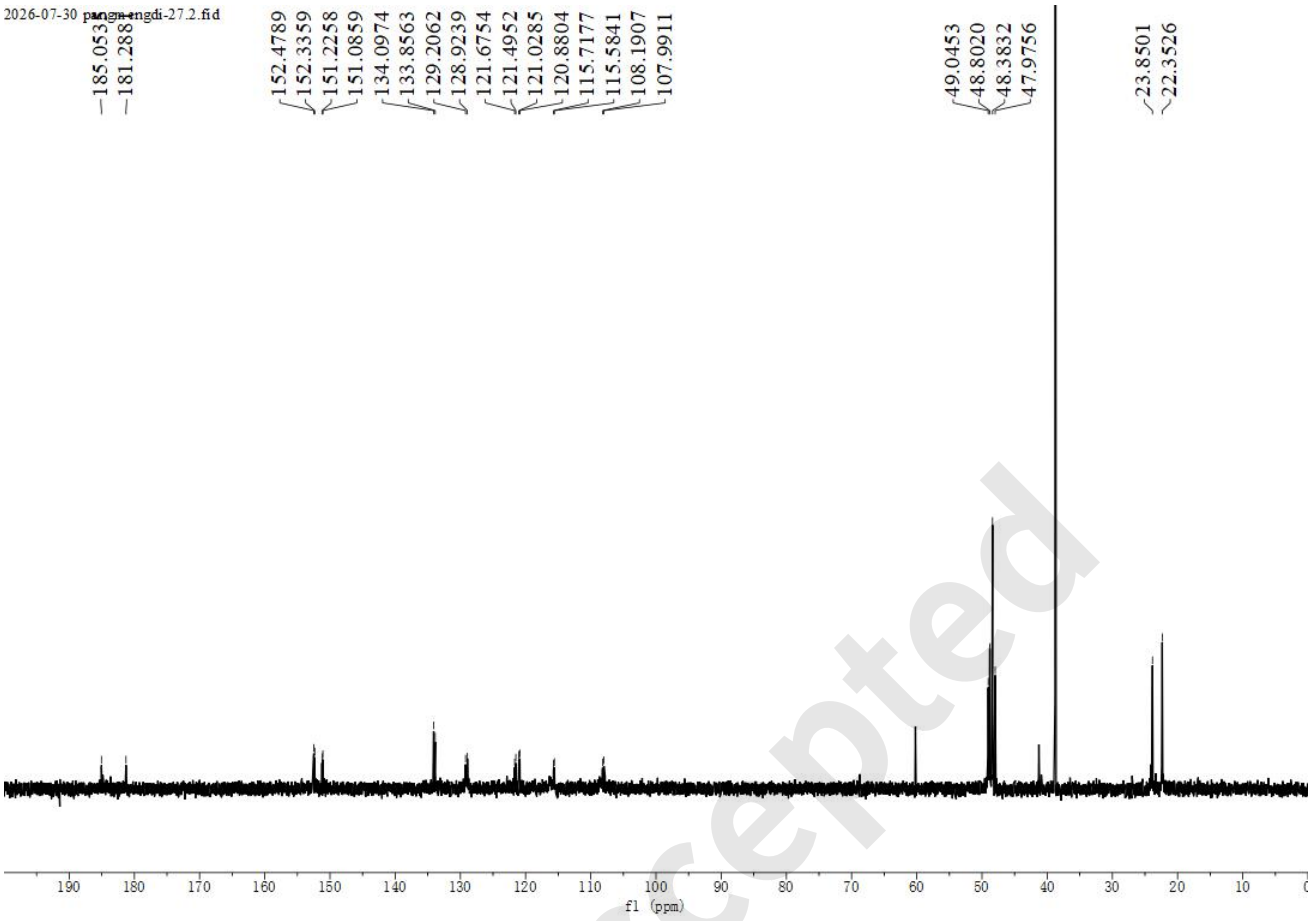

Figure S27 ^{13}C NMR (100 MHz, D_2O) spectrum of **27AQS.**

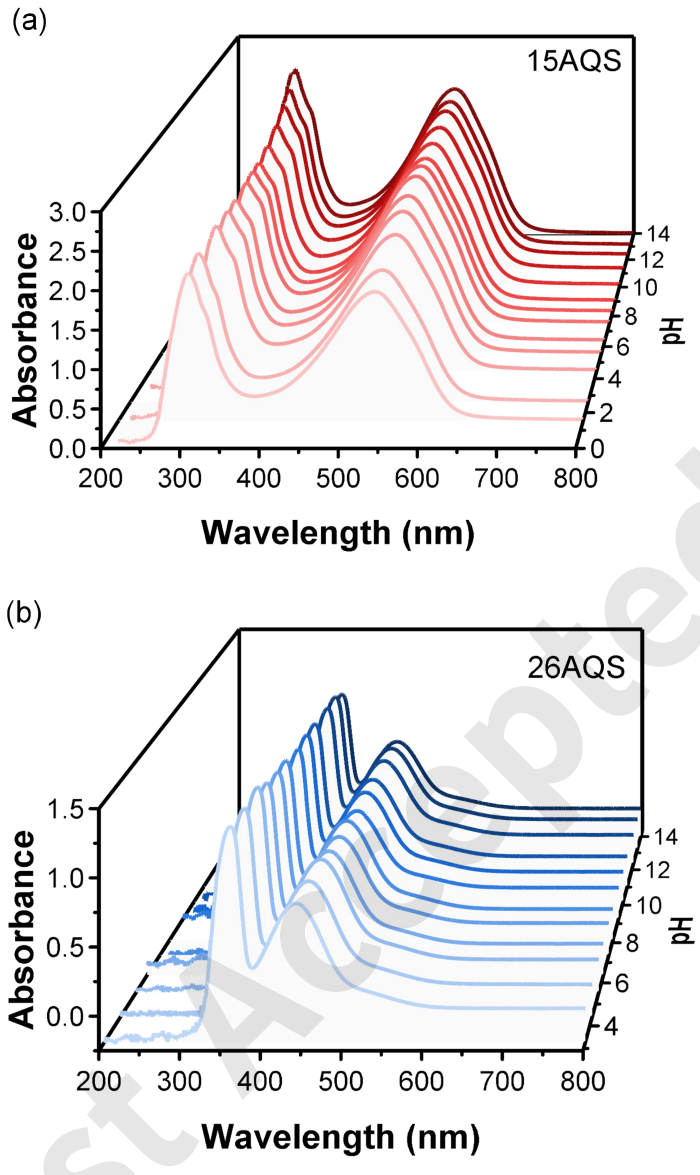

Figure S28 UV-Vis absorption spectra of **15AQS** (a) and **26AQS** (b) solutions at different pH values

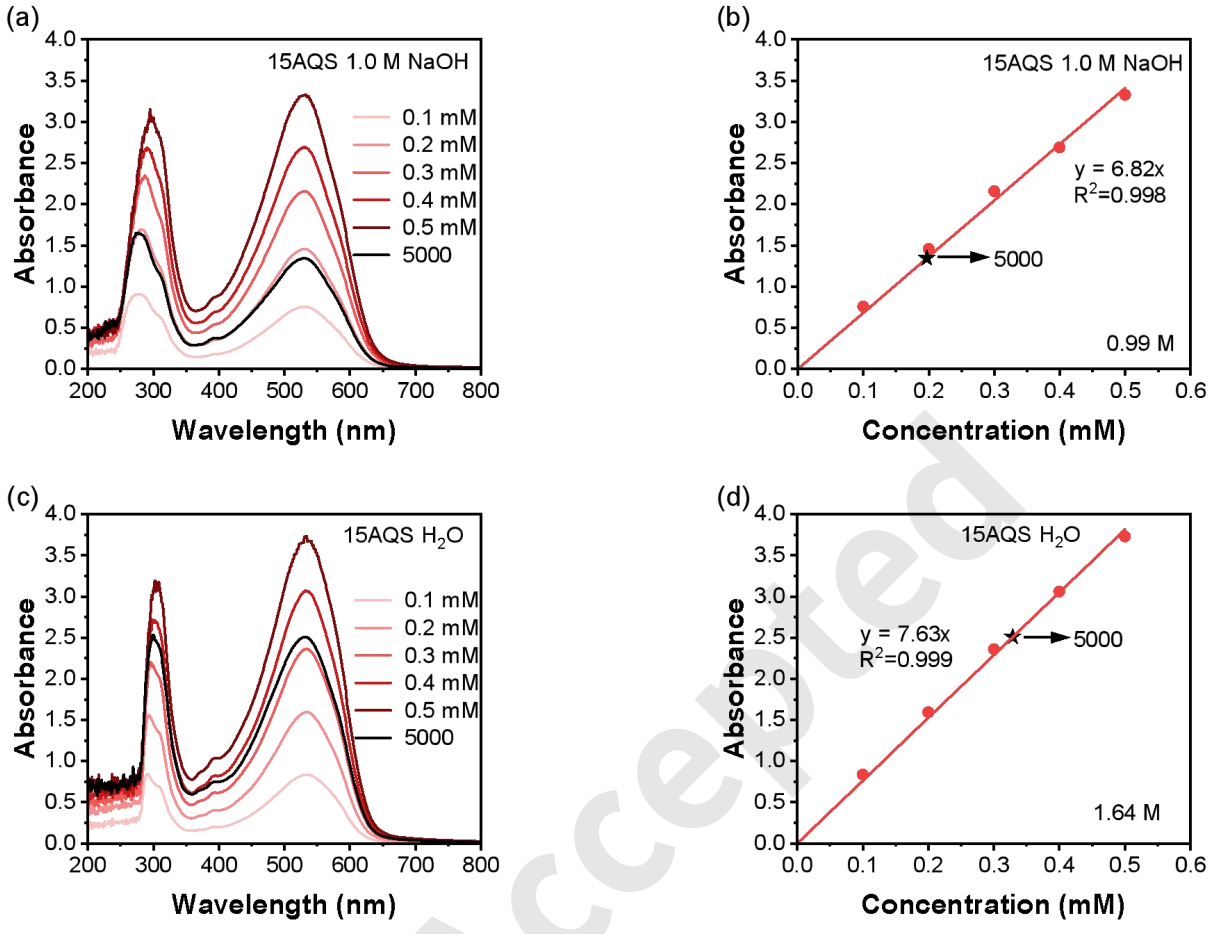

Figure S29 Solubility assessment of **15AQS**. UV-Vis spectra of **15AQS** at varying concentrations in 1.0 M NaOH (a) and H_2O solution (c), with "5000" indicating a 5000-fold dilution from the saturated solution. Fitted plot of absorbance at 535 nm as a function of **15AQS** concentration in 1.0 M NaOH (b) and H_2O solution (d).

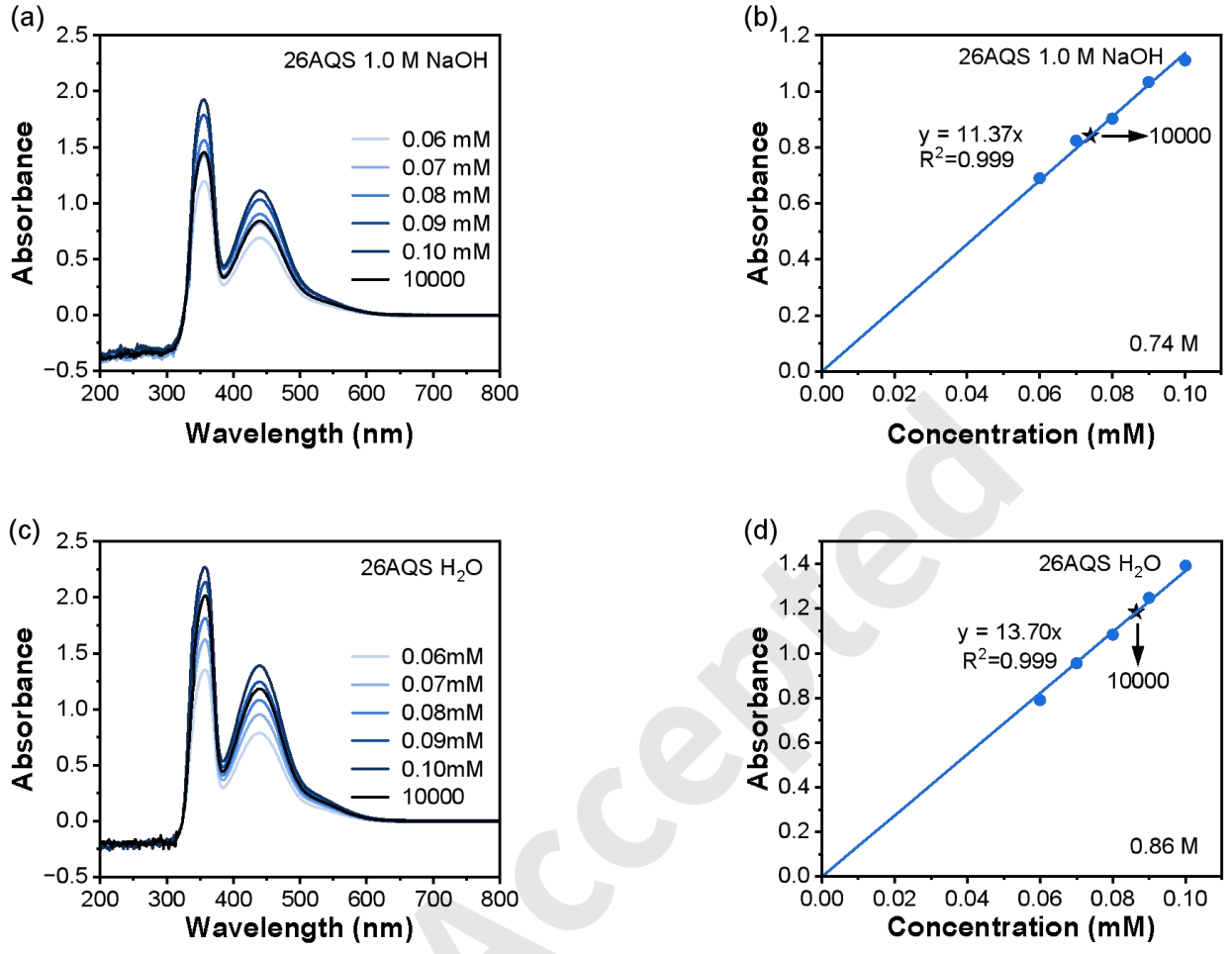

Figure S30 Solubility assessment of **26AQS**. UV-Vis spectra of **26AQS** at varying concentrations in 1.0 M NaOH (a) and H_2O solution (c), with "10000" indicating a 10000-fold dilution from the saturated solution. Fitted plot of absorbance at 440 nm as a function of **26AQS** concentration in 1.0 M NaOH (b) and H_2O solution (d).

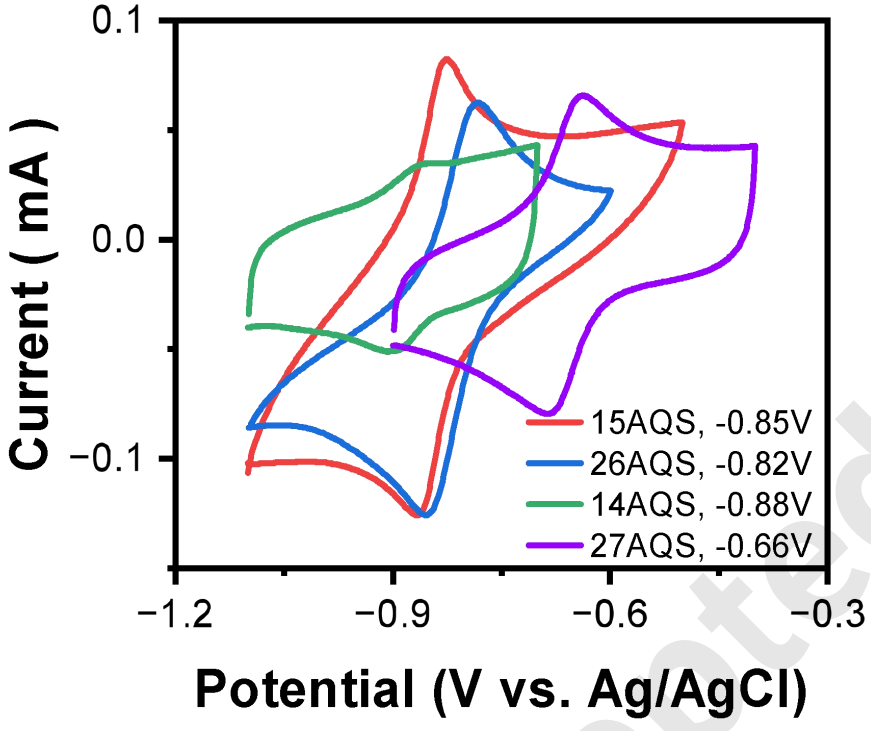

Figure S31 CV study of 5mM **14AQS**, **15AQS**, **26AQS and 27AQS** in 1.0 M NaOH solutions at scan rate of 100 mV s^{-1}.

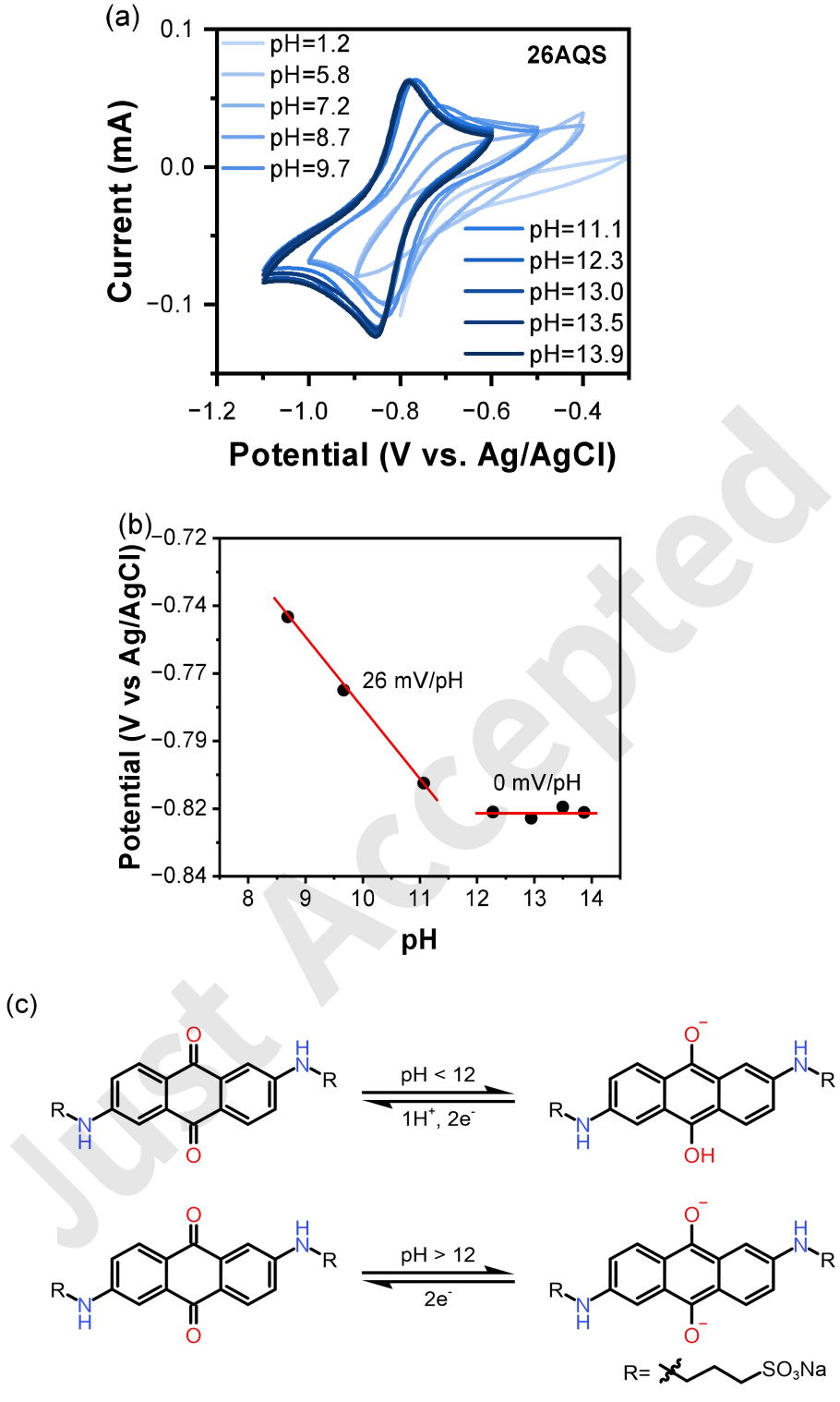

Figure S32 (a) CV curves of **26AQS** at various pH; (b) Pourbaix diagram of **26AQS**; (c) The ionization process of **26AQS** and its reduced forms.

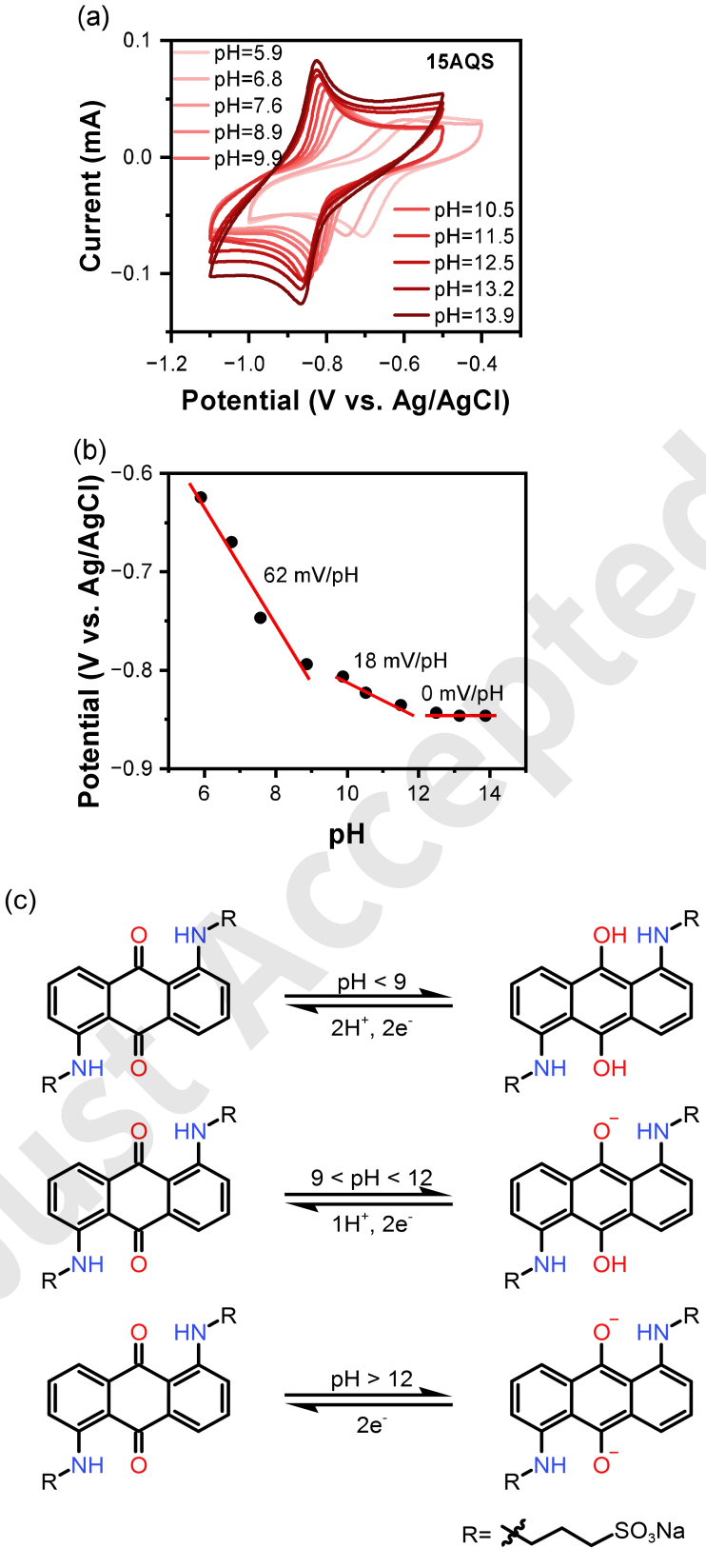

Figure S33 (a) CV curves of **15AQS** at various pH; (b) Pourbaix diagram of **15AQS**; (c) The ionization process of **15AQS** and its reduced forms.

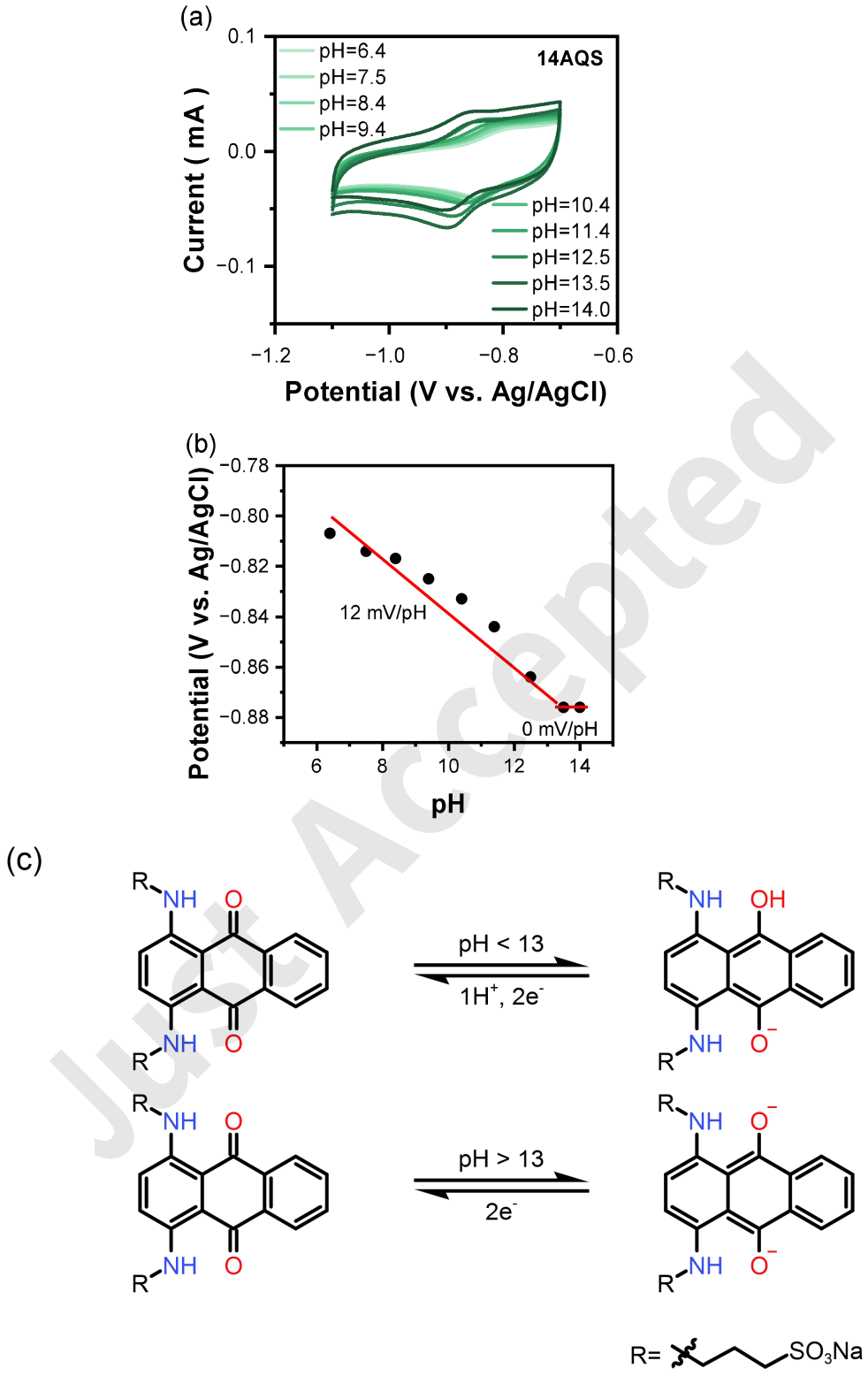

Figure S34 (a) CV curves of **14AQS** at various pH; (b) Pourbaix diagram of **14AQS**; (c) The ionization process of **14AQS** and its reduced forms.

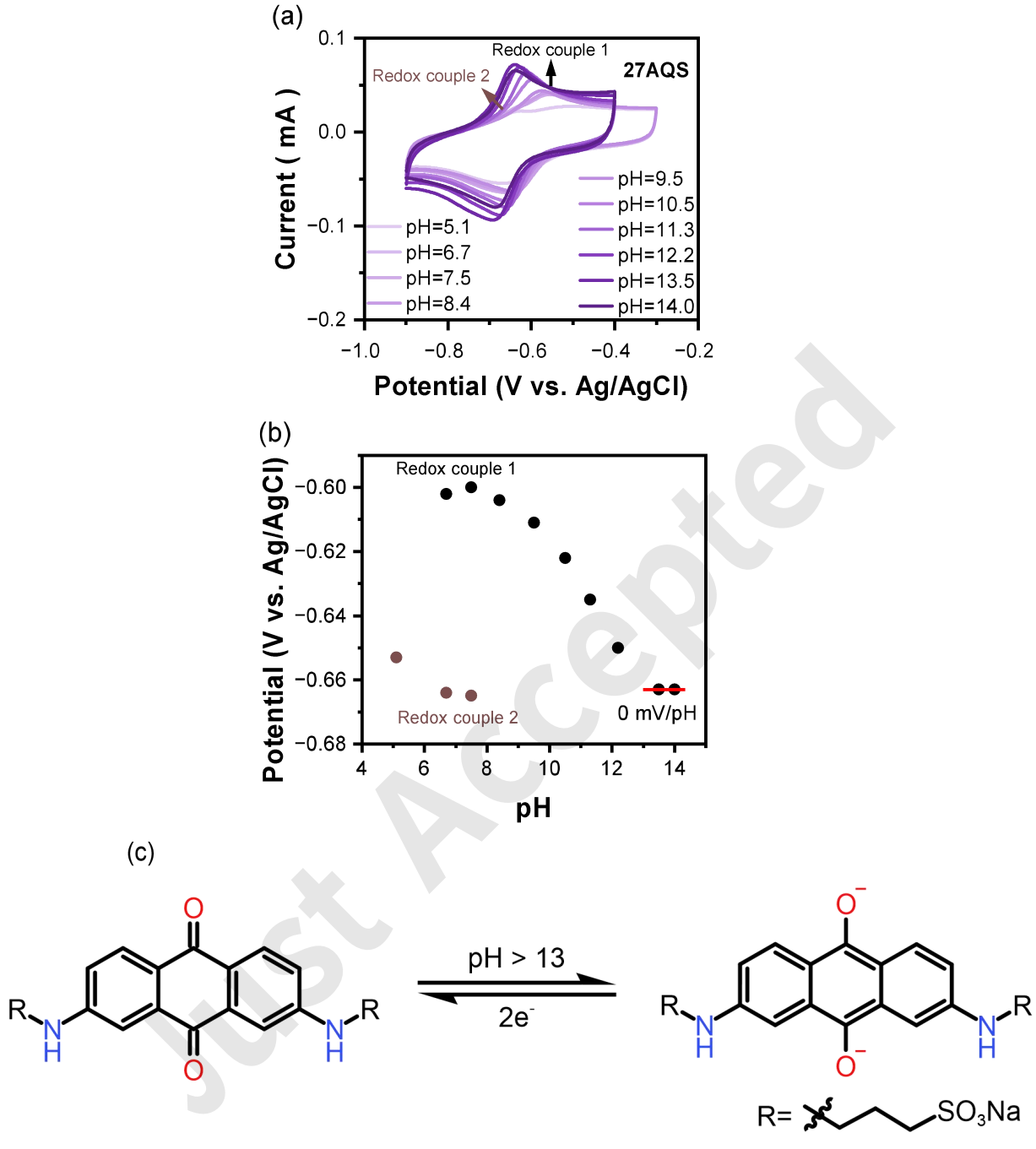

Figure S35 (a) CV curves of **27AQS** at various pH; (b) Pourbaix diagram of **27AQS**; (c) The ionization process of **27AQS** and its reduced forms.

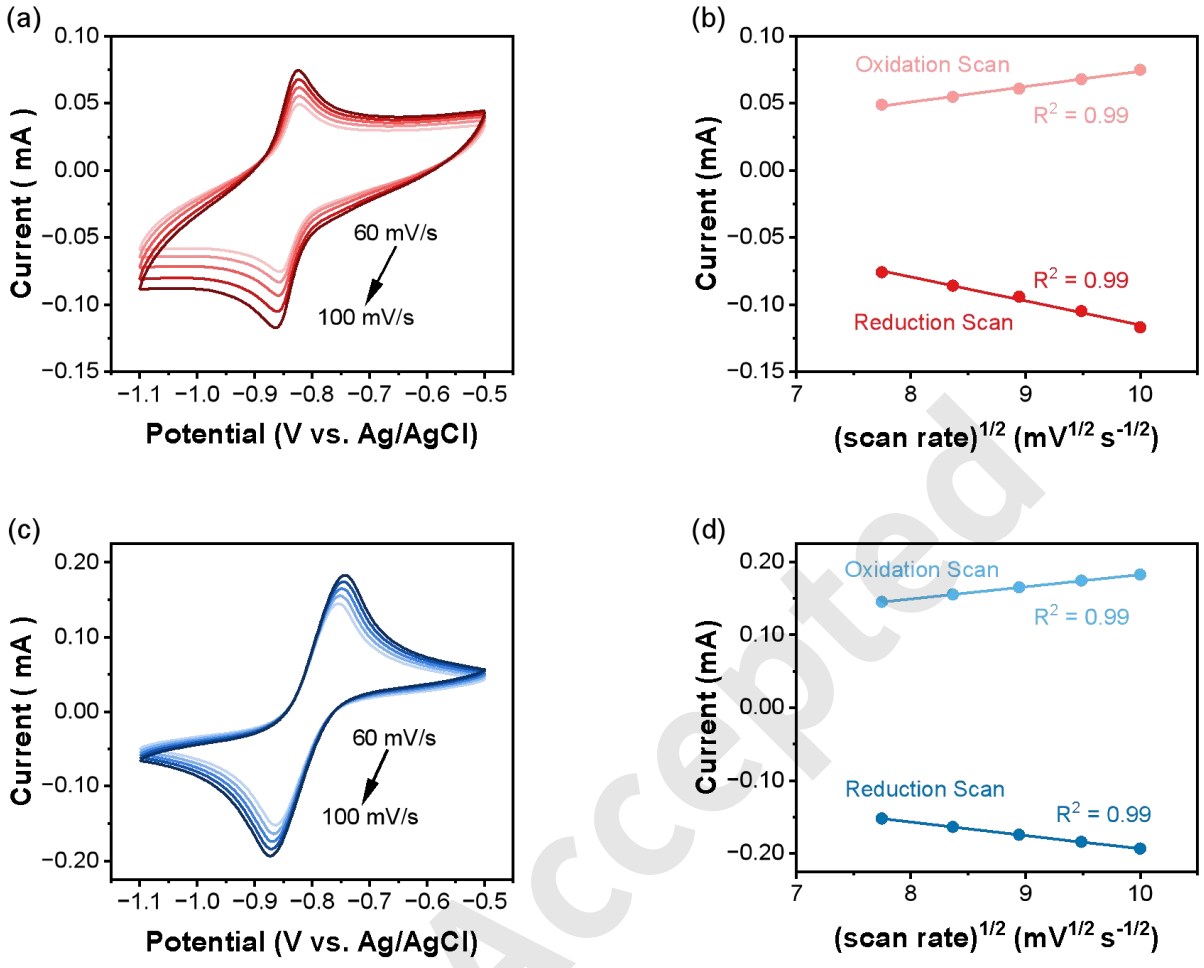

Figure S36 CV study of 5mM **15AQS** (a) and **26AQS** (c) in 1.0 M NaOH solutions at different scan rate from 60 to 100 mV s^{-1}. Corresponding oxidation and reduction peak currents of **15AQS** (b) and **26AQS** (d).

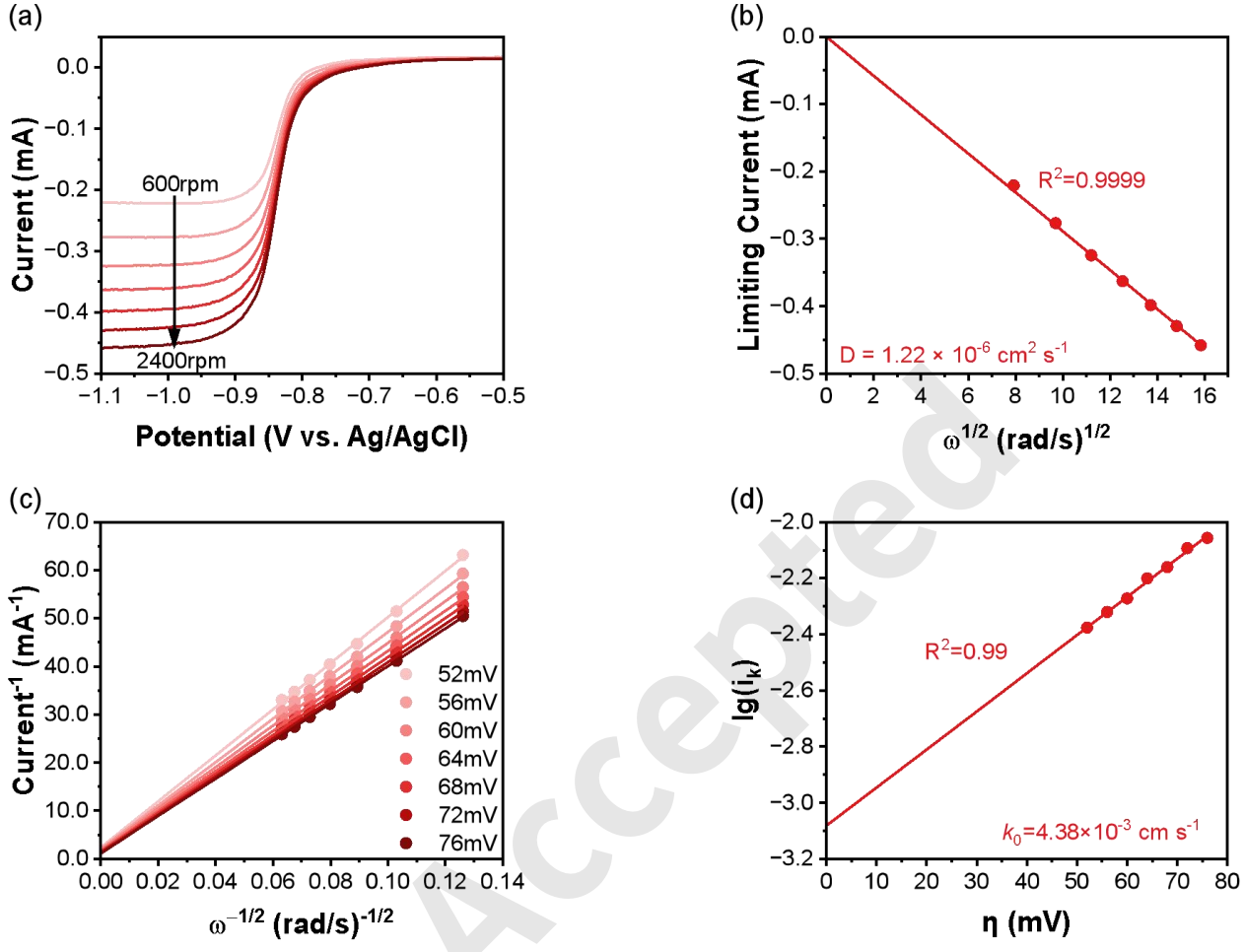

Figure S37 Electrochemical analysis of **15AQS** reduction kinetics via RDE. (a) LSVs recorded in 1 M NaOH at rotation rates between 600 and 2400 rpm. (b) Levich plot represented the limiting current as a function of the square root of rotation rate. (c) Koutecky-Levich plots depicting the reciprocal current against the inverse square root of rotation rate. (d) Tafel plot constructed from the kinetic data.

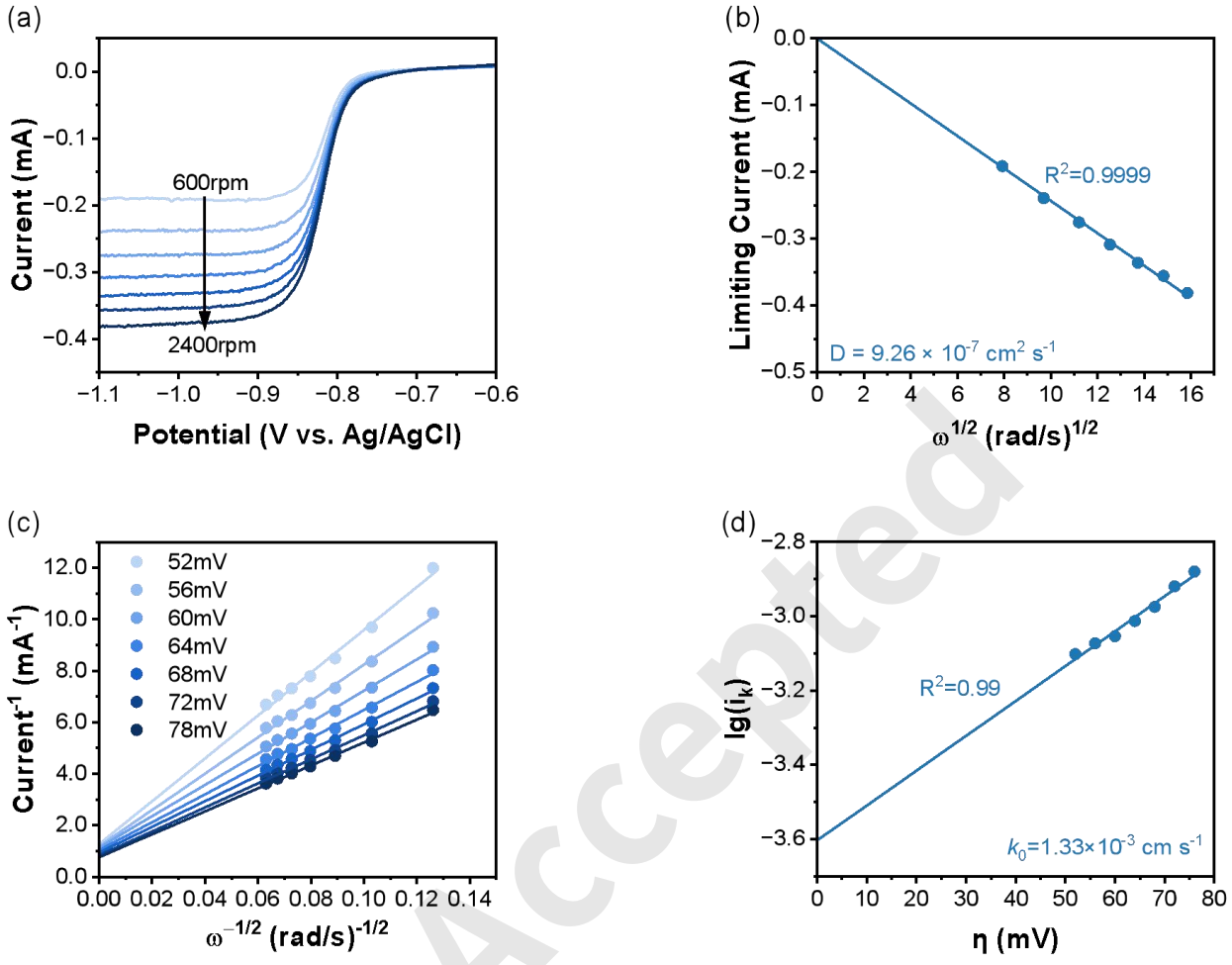

Figure S38 Electrochemical analysis of **26AQS** reduction kinetics via RDE. (a) LSVs recorded in 1 M NaOH at rotation rates between 600 and 2400 rpm. (b) Levich plot represented the limiting current as a function of the square root of rotation rate. (c) Koutecky-Levich plots depicting the reciprocal current against the inverse square root of rotation rate. (d) Tafel plot constructed from the kinetic data.

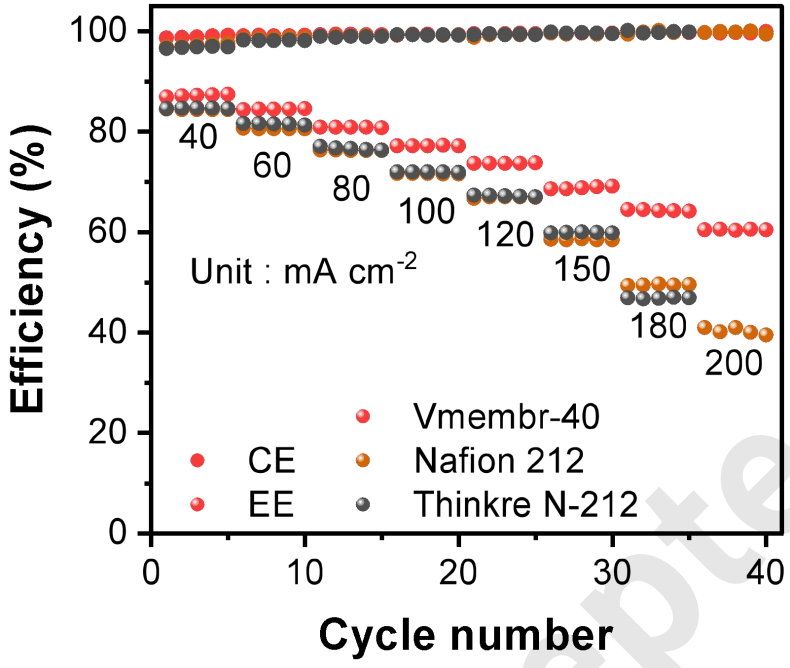

Figure S39 Coulombic and energy efficiencies, specific capacities of 0.05 M **15AQS**||$Na_4[Fe(CN)_6]$ AORFB evaluated at various current densities: 40 - 200 mA cm^{-2} with different membranes

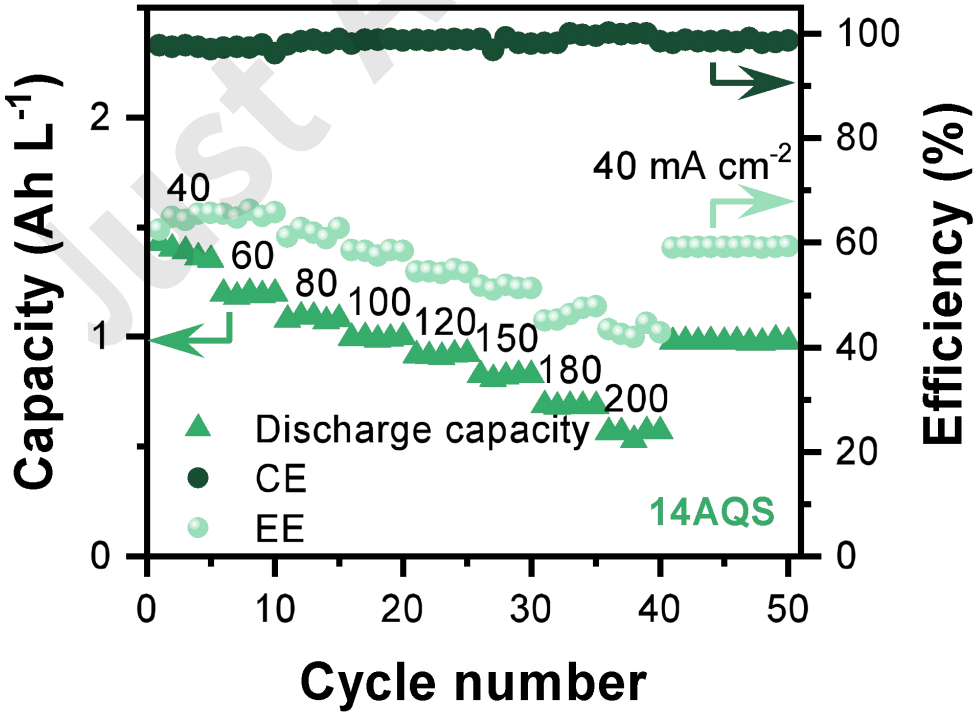

Figure S40 Coulombic and energy efficiencies, specific capacities of **14AQS**||$Na_4[Fe(CN)_6]$ AORFB evaluated at various current densities: 40 - 200 mA cm^{-2}.

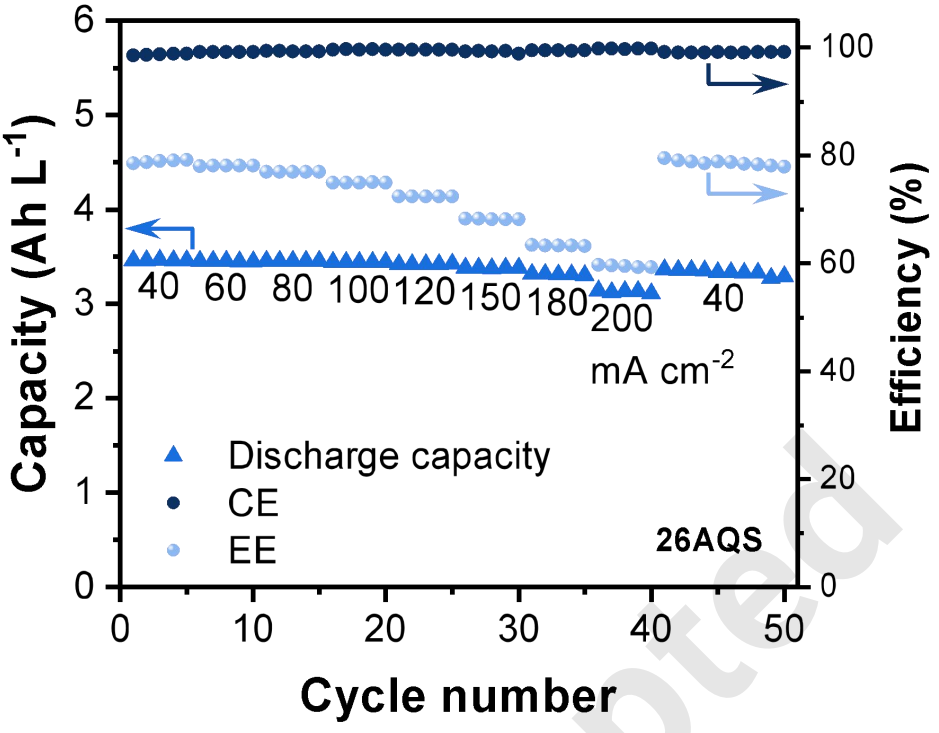

Figure S41 Coulombic and energy efficiencies, specific capacities of **26AQS**||$Na_4[Fe(CN)_6]$ AORFB evaluated at various current densities: 40 - 200 mA cm^{-2}.

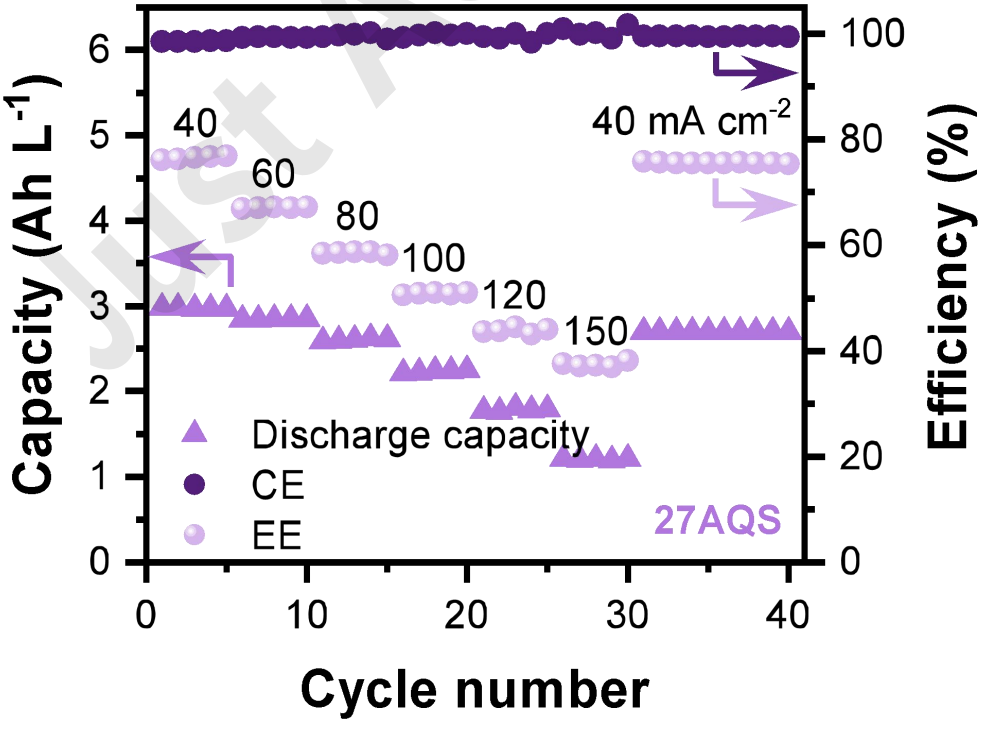

Figure S42 Coulombic and energy efficiencies, specific capacities of **27AQS**||$Na_4[Fe(CN)_6]$ AORFB evaluated at various current densities: 40 - 200 mA cm^{-2}.

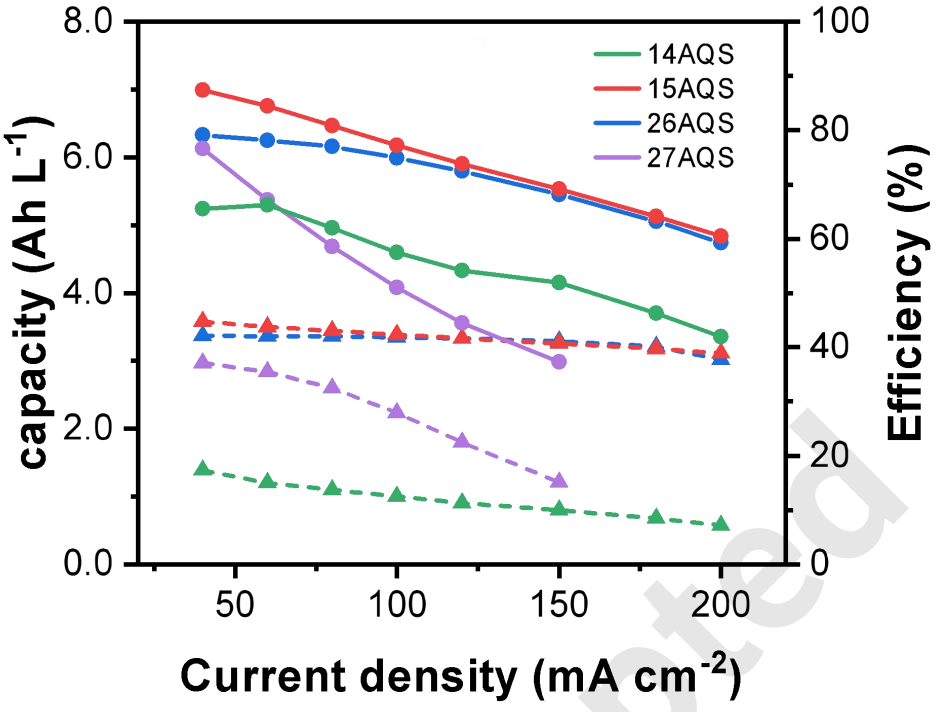

Figure S43 Energy efficiency and capacity utilization of the 0.1 M AQs||$Na_4[Fe(CN)_6]$ AORFB at various current density (40 to 200 mA cm^{-2}).

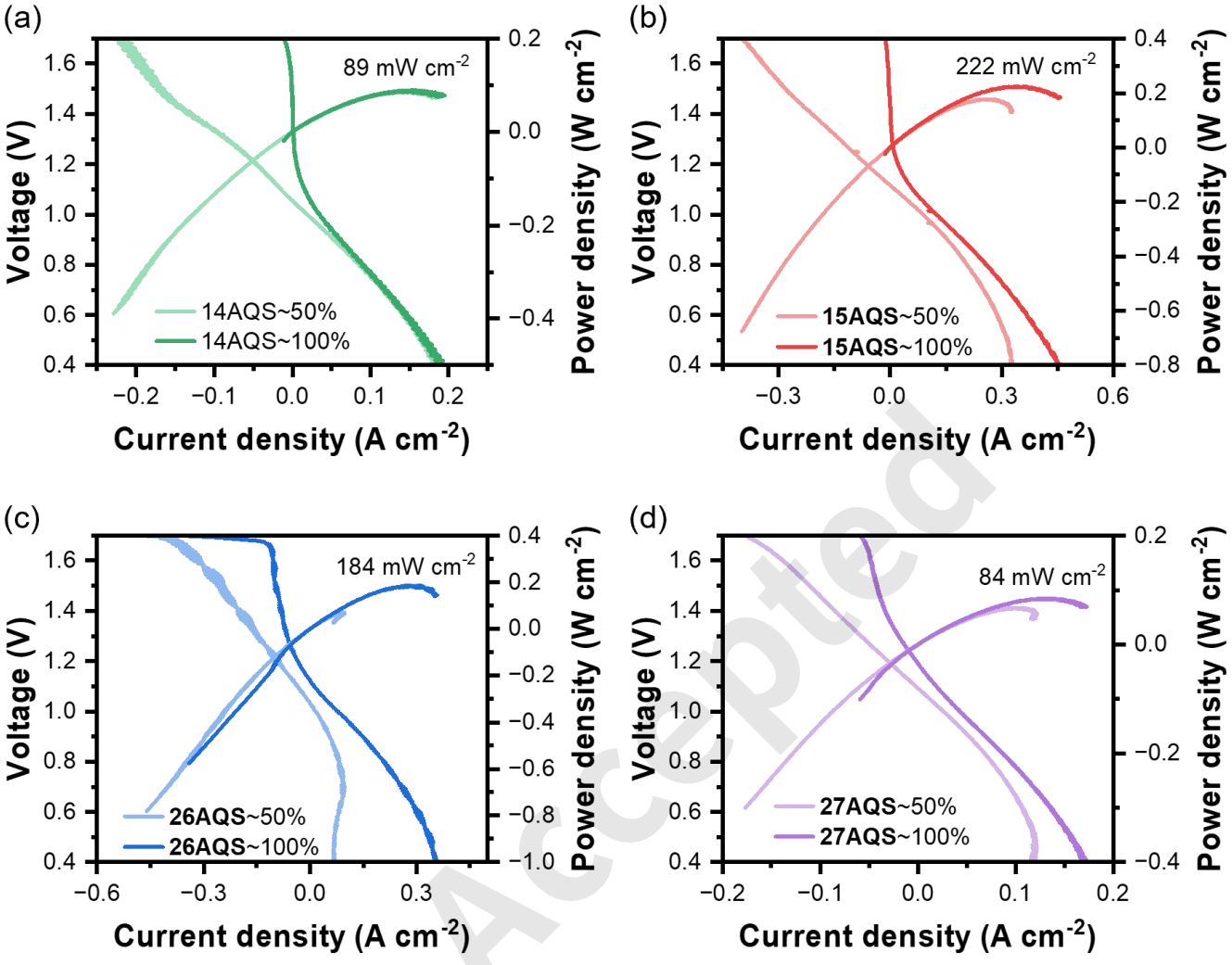

Figure S44 Polarization and power density curves of 0.1 M AQs||$Na_4[Fe(CN)_6]$ AORFBs collected at SOCs of 50% and 100%. (a) **14AQS**; (b) **15AQS;** (c) **26AQS**; (d) **27AQS**.

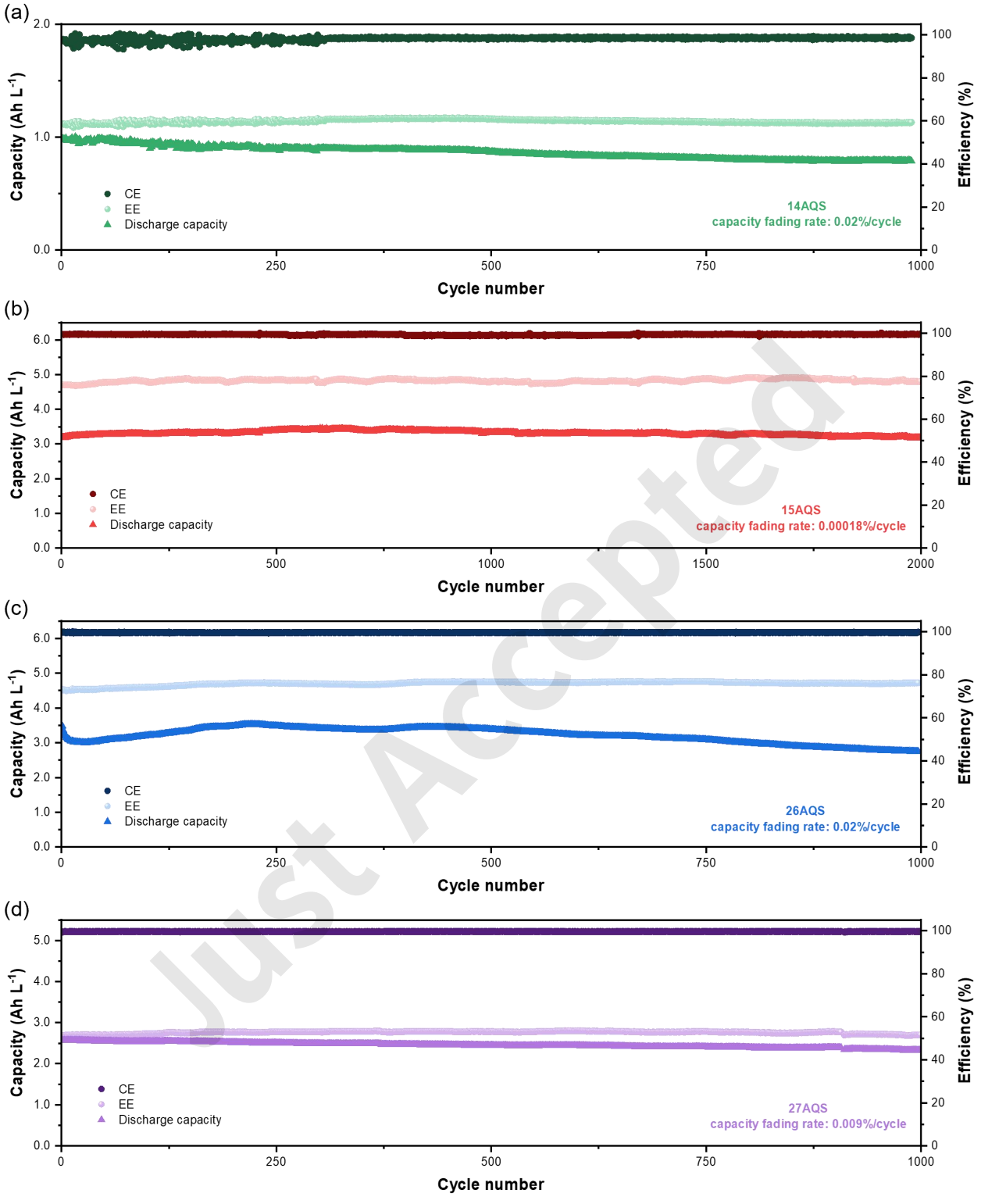

Figure S45 Cycling performances of 0.1 M AQs||$Na_4[Fe(CN)_6]$ AORFBs in 1.0 M NaOH solutions at a current density of 100 mA cm^{-2} ranging from 1.7 to 0.4 V. (a) **14AQS**; (b) **15AQS;** (c) **26AQS**; (d) **27AQS**.

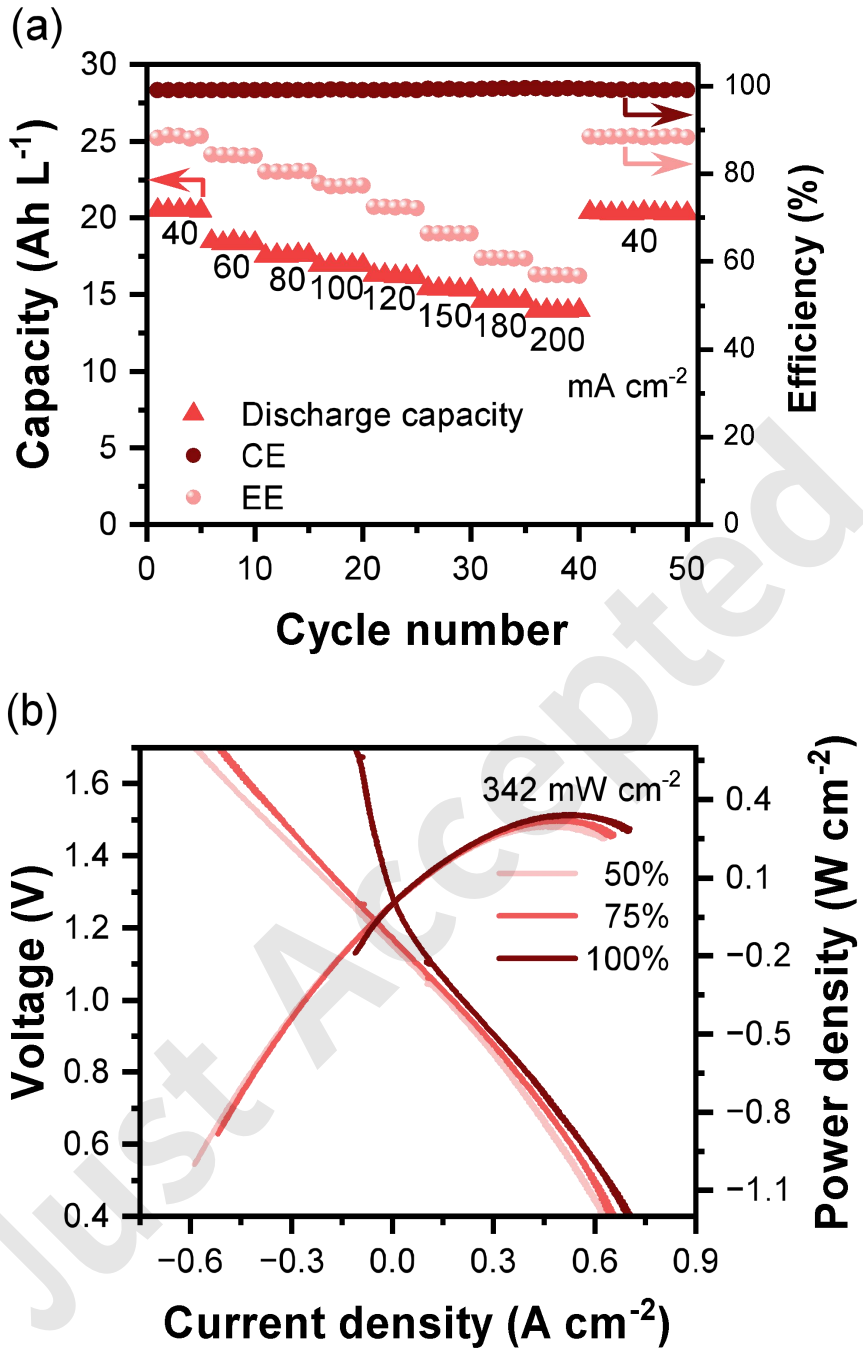

Figure S46 (**a**) Coulombic and energy efficiencies, specific capacities of 0.5 M **15AQS**||$Na_4[Fe(CN)_6]$ AORFB evaluated at various current densities; (**b**) Polarization and power density curves of 0.5 M **15AQS**||$Na_4[Fe(CN)_6]$ AORFB.

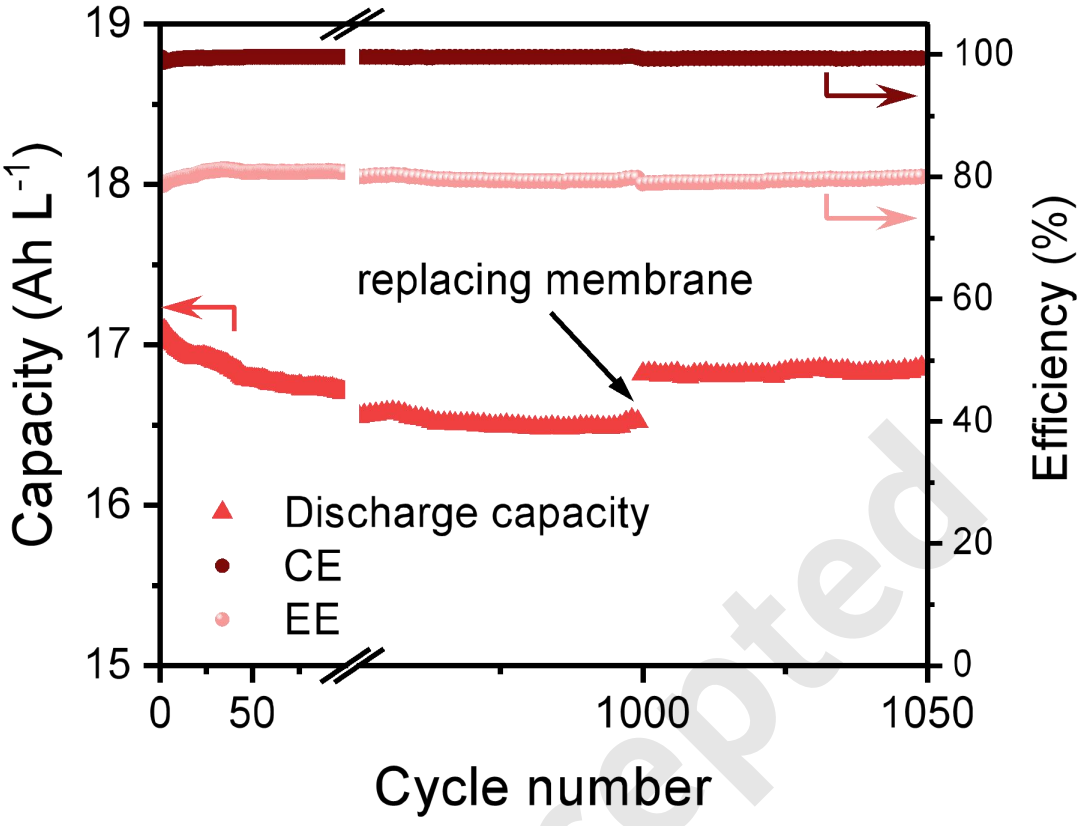

Figure S47 Cycling performances of 0.5 M **15AQS**||$Na_4[Fe(CN)_6]$ AORFBs in 1.0 M NaOH solutions at a current density of 100 mA cm^{-2} ranging from 1.7 to 0.4 V with replacing the membrane (Vmembr-40) after the 1000th cycles.

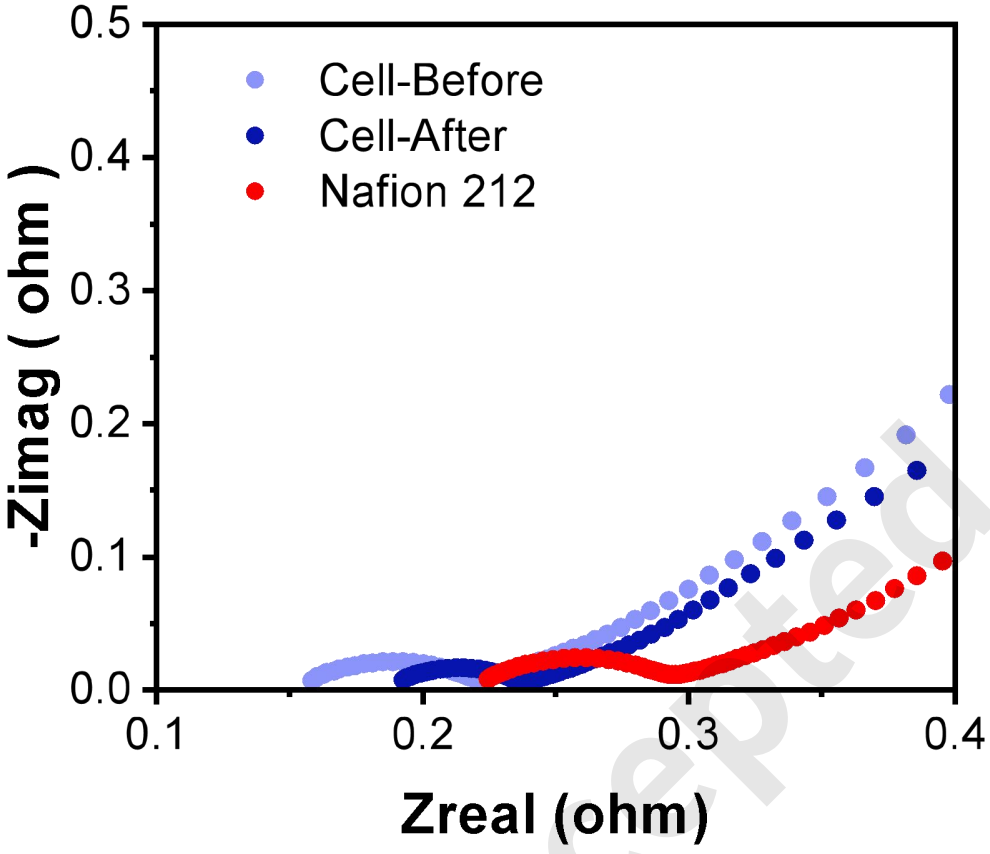

Figure S48 Nyquist plots of the 0.5 M **15AQS**||$Na_4[Fe(CN)_6]$ AORFB using the Vmembr-40 membrane before and after cycling, compared with that using a Nafion-212 membrane.

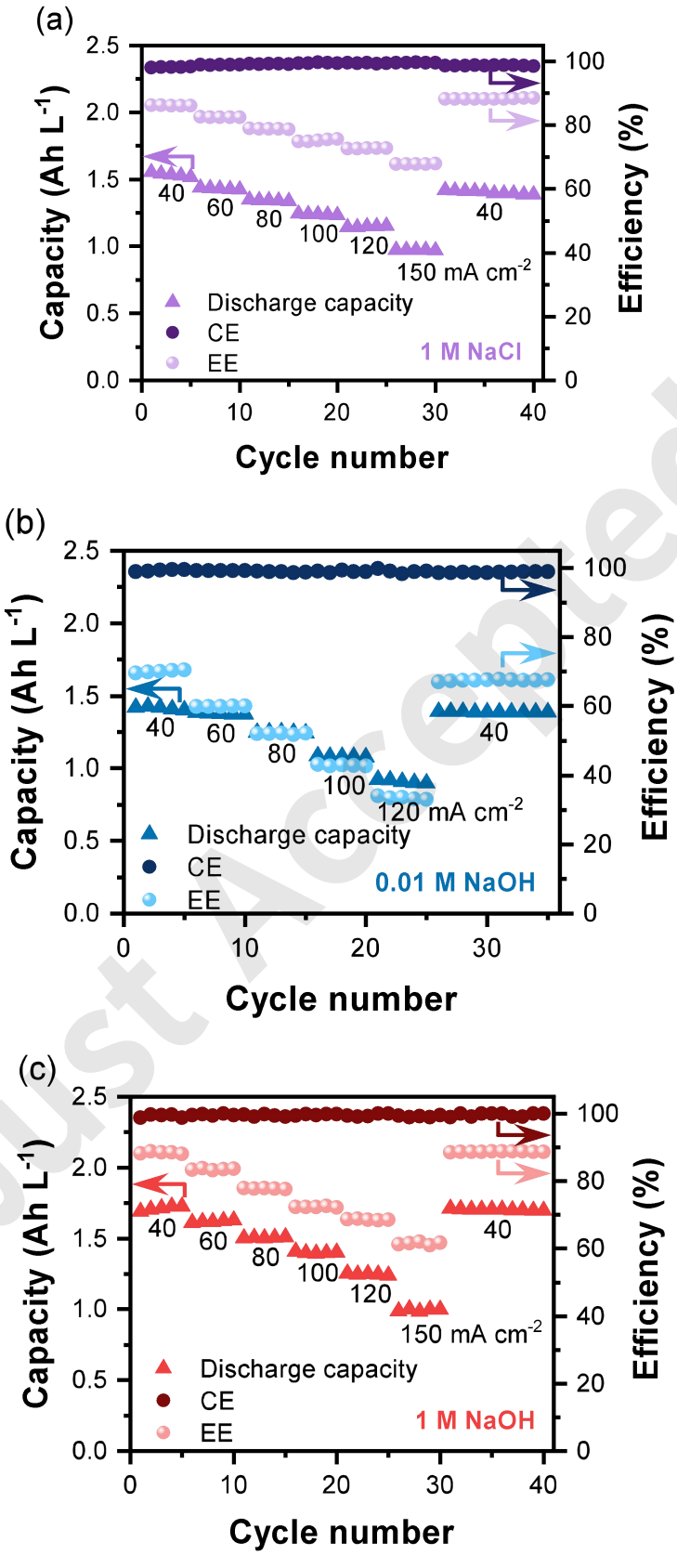

Figure S49 Coulombic and energy efficiencies, capacities of 0.05 M **15AQS**||$Na_4[Fe(CN)_6]$ AORFBs in different electrolyte solutions.

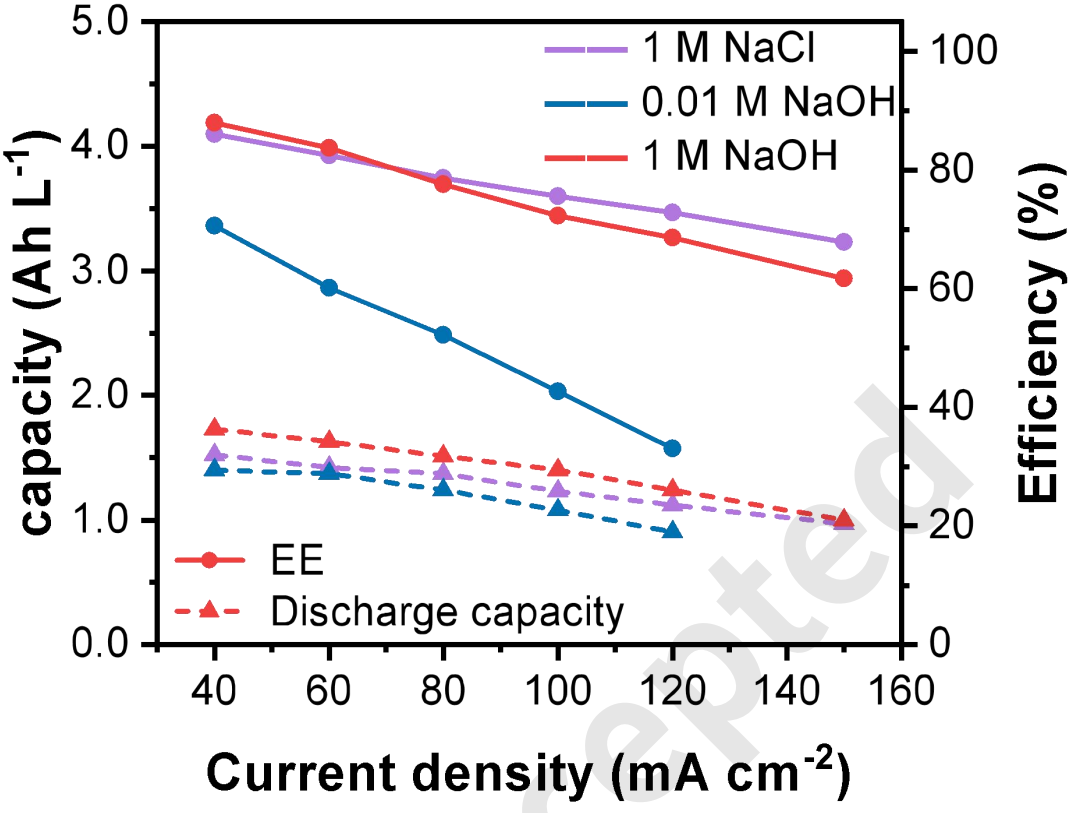

Figure S50 Energy efficiency and capacity utilization of the 0.05 M **15AQS**||$Na_4[Fe(CN)_6]$ AORFB at various current density (40 to 150 mA cm^{-2}) in different electrolyte solutions.

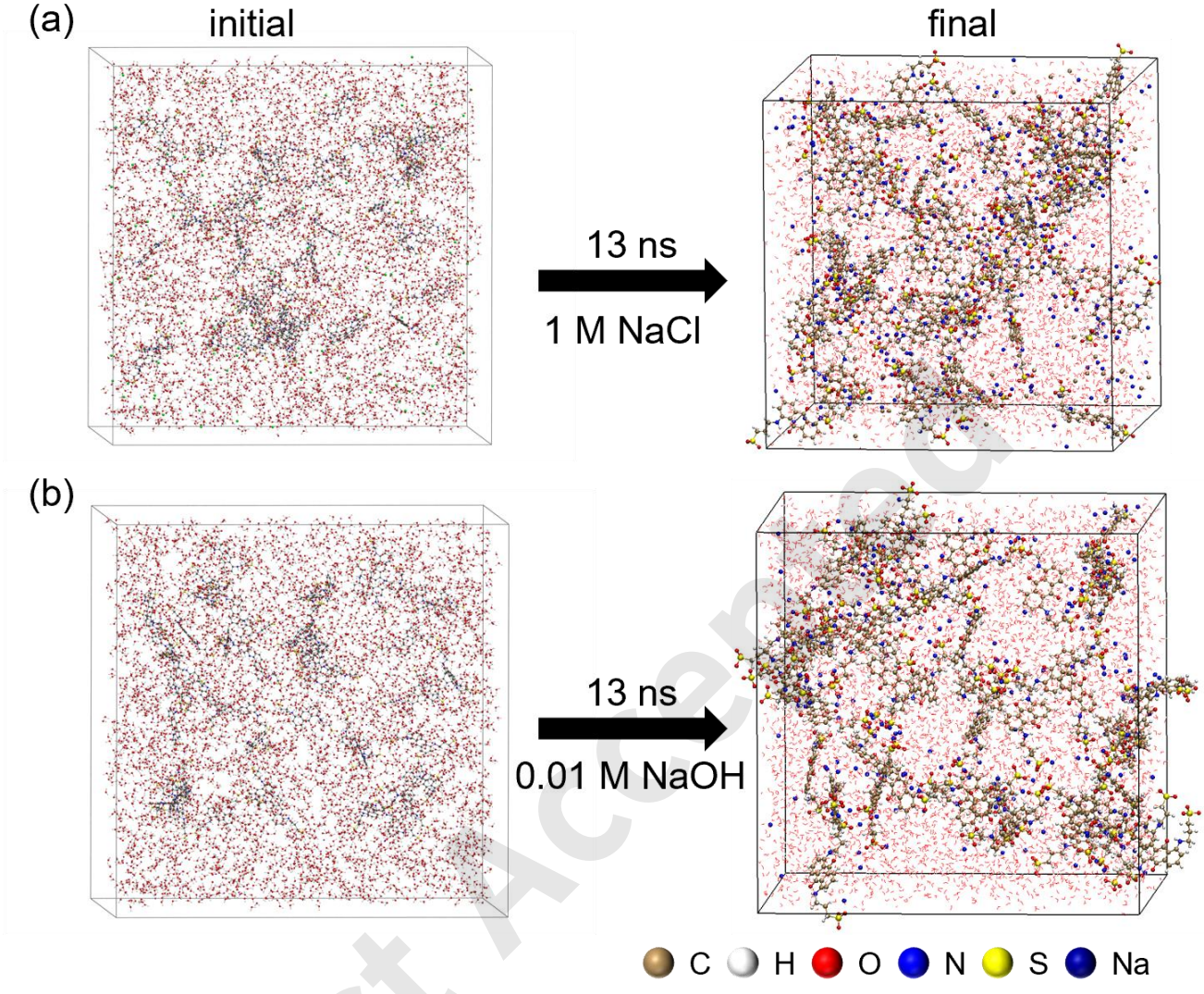

Figure S51 MD simulation snapshots and the hydration schematic diagrams of **15AQS** in different electrolyte solution. (a) 1 M NaCl; (b) 0.01 M NaOH.

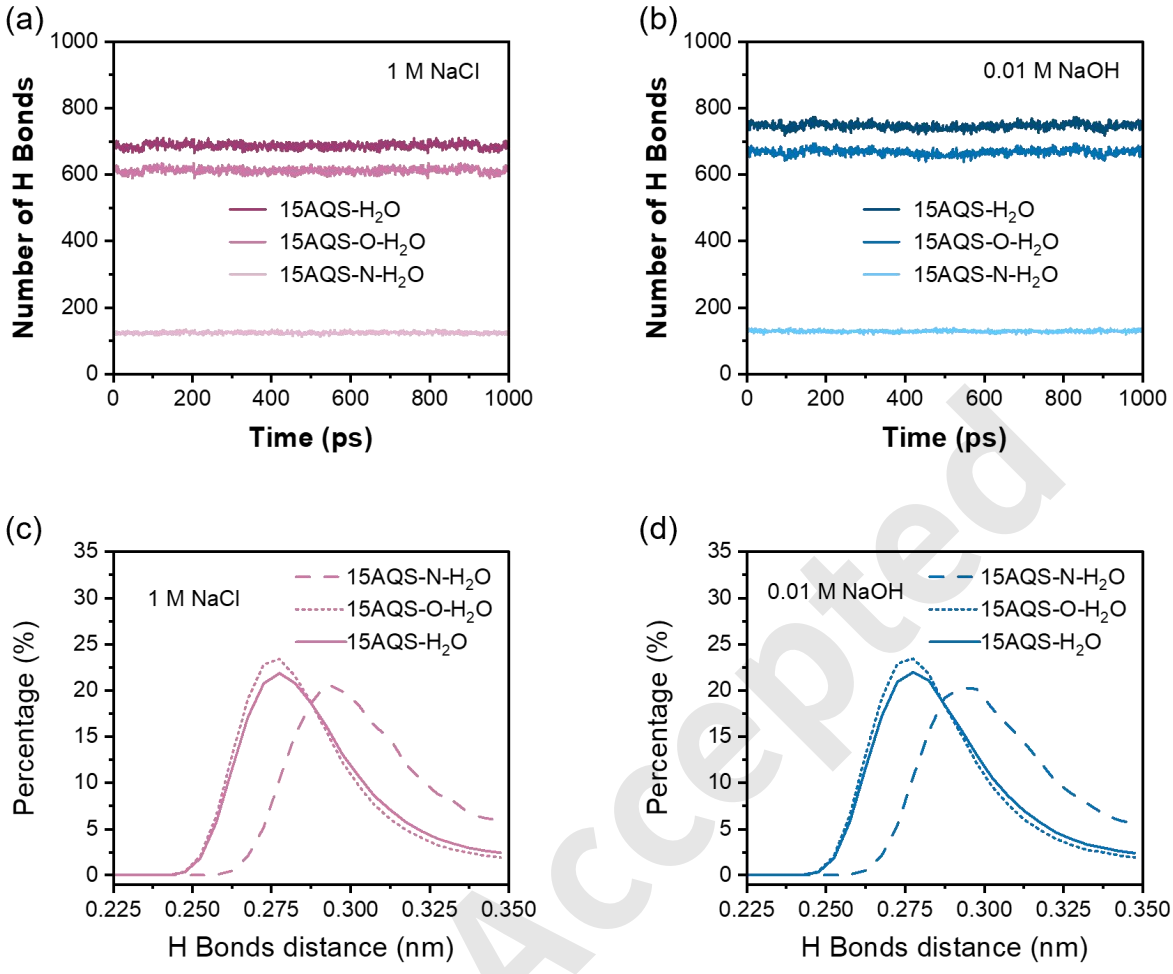

Figure S52 Results from MD simulations show the time evolution and optimized count of hydrogen bonds formed around the**15AQS** and the distribution of H-bonding distances in different electrolyte solution. (a), (c)1 M NaCl; (b), (d)0.01 M NaOH.

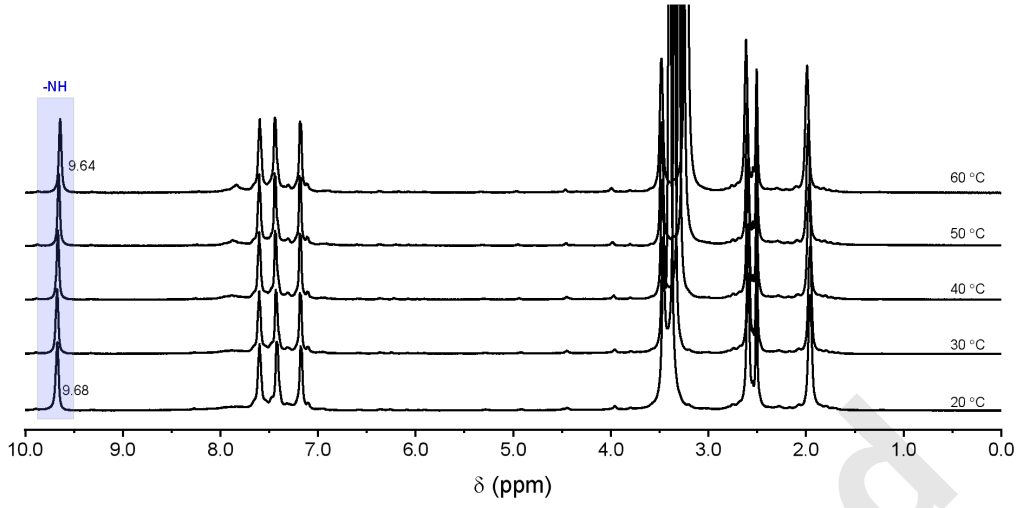

Figure S53 Variable-temperature ^{1}H NMR spectra of **15AQS** in the temperature range of 20-60°C.

Plausible reaction mechanism of 15AQS negolytes during charge-discharge cycles.

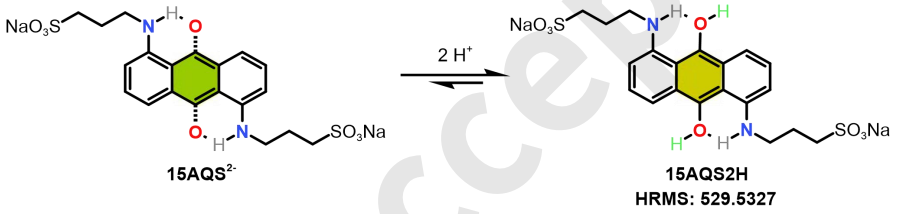

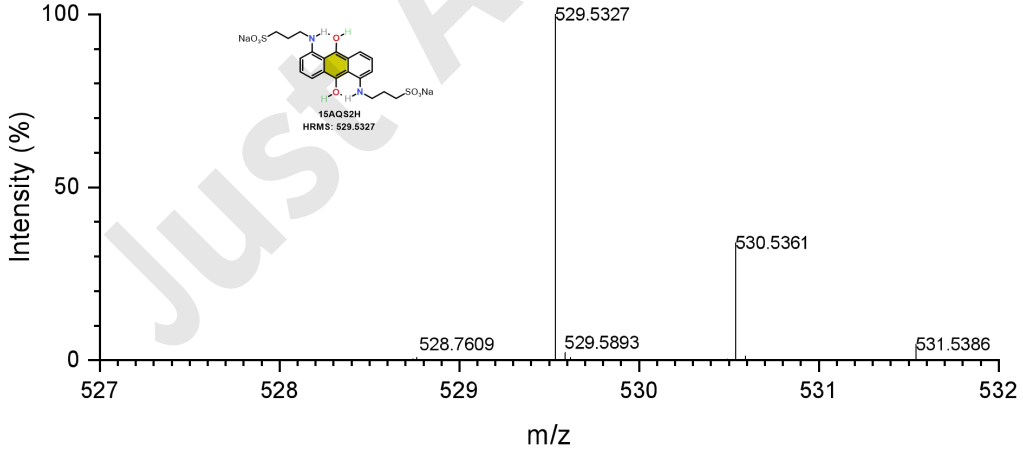

Figure S54 HRMS (ESI) $Na_2C_{20}H_{23}O_8N_2S_2$ $[M+H]^+$ found: 529.5327.

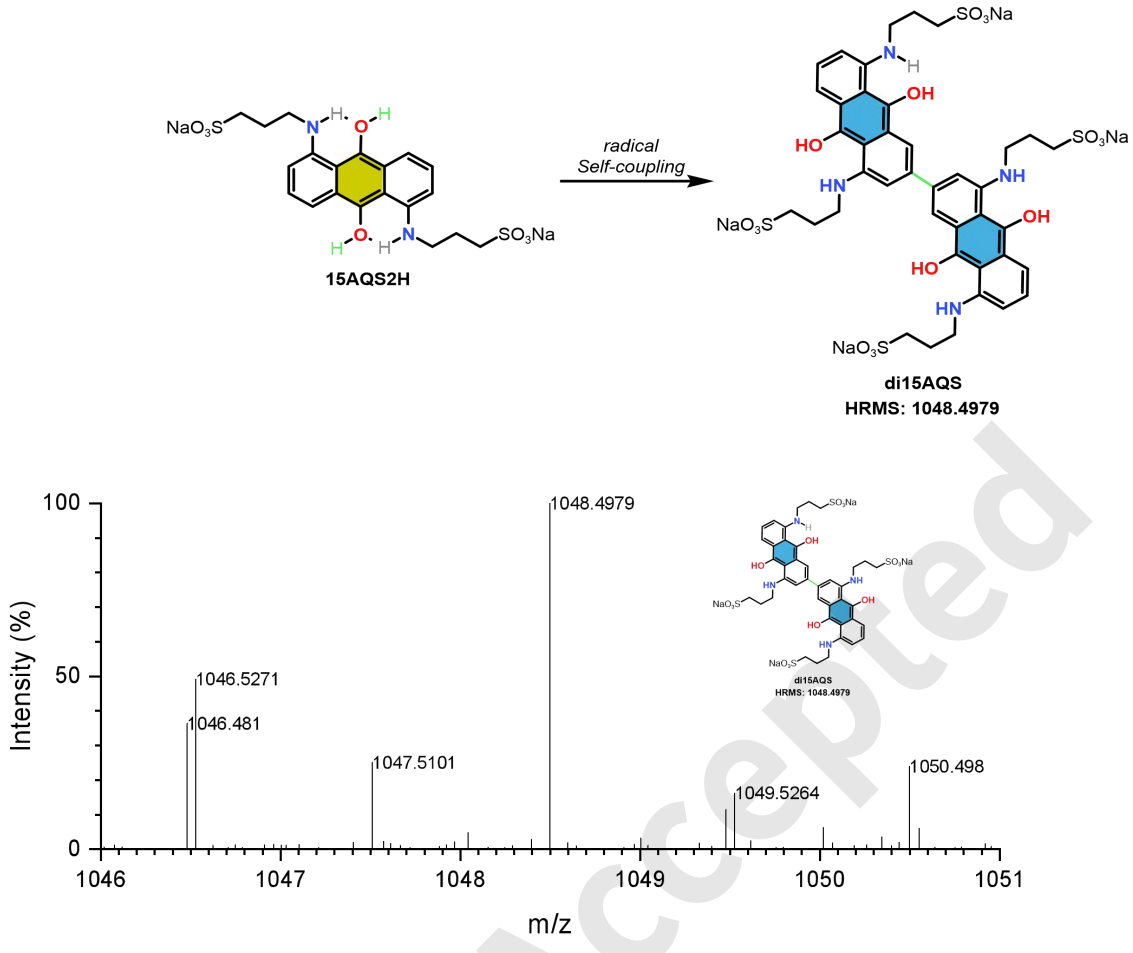

Figure S55 HRMS (ESI) $Na_4C_{40}H_{36}O_{16}N_4S_4$ $[M+H]^+$ found: 1048.4979.

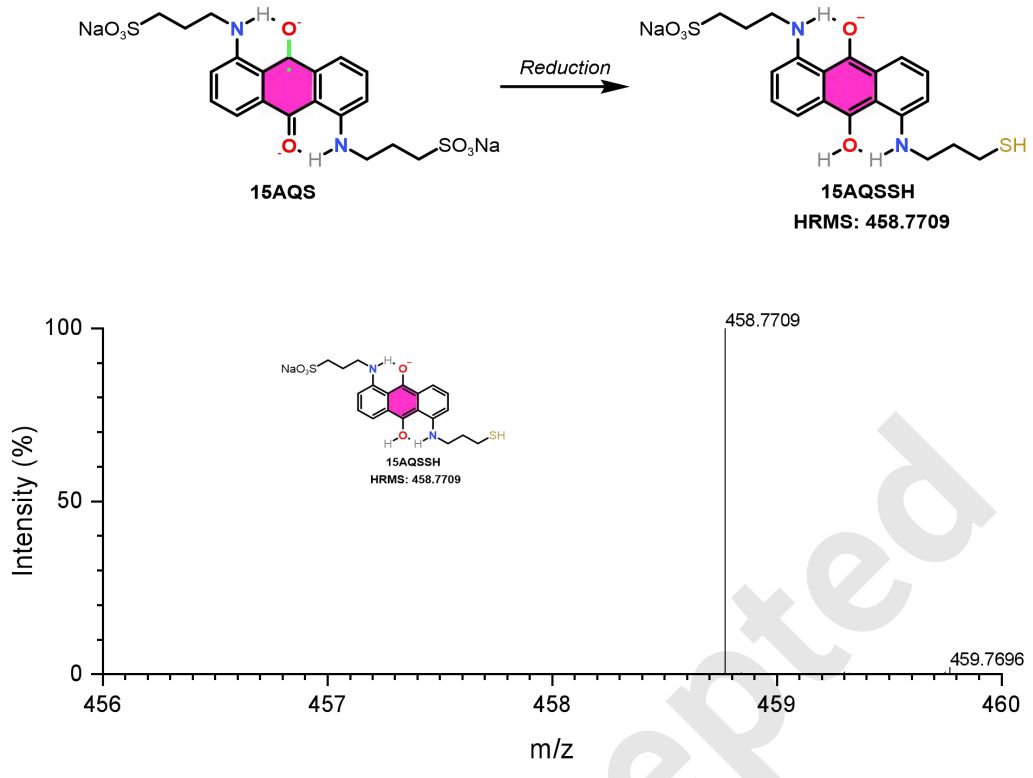

Figure S56 HRMS (ESI) $NaC_{20}H_{22}O_5N_2S_2$ $[M]^-$ found: 458.7709.

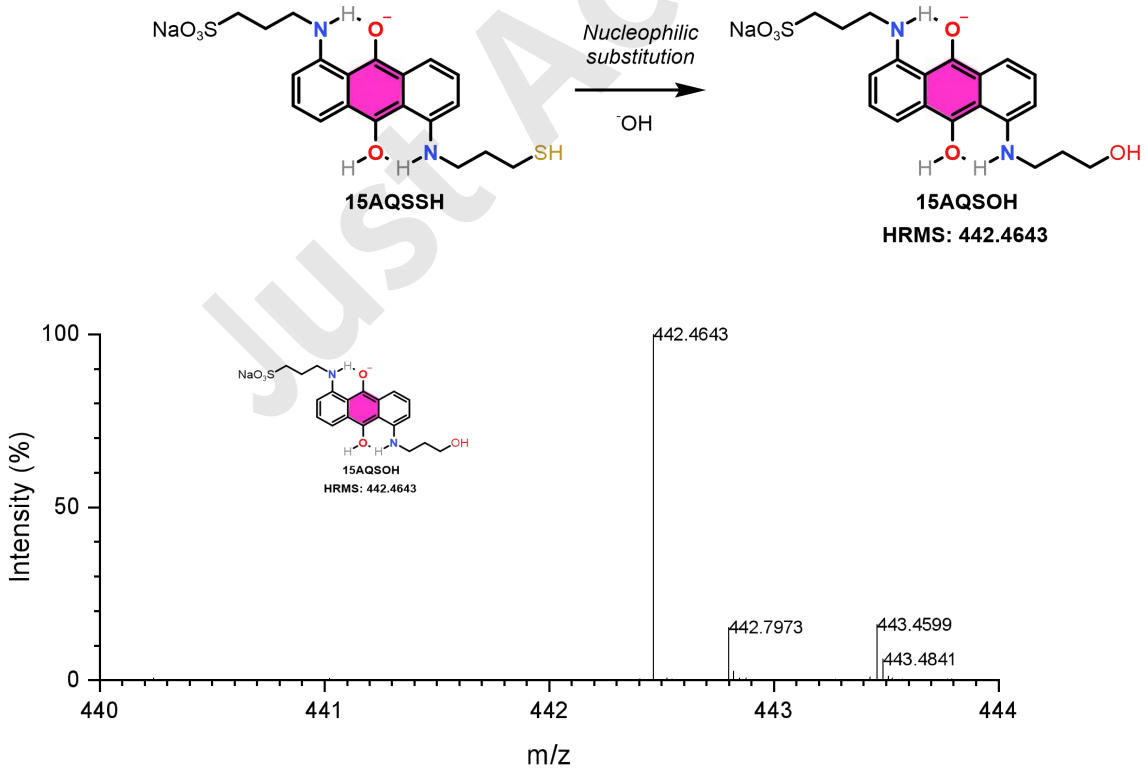

Figure S57 HRMS (ESI) $NaC_{20}H_{22}O_6N_2S$ $[M]^-$ found: 442.4643.

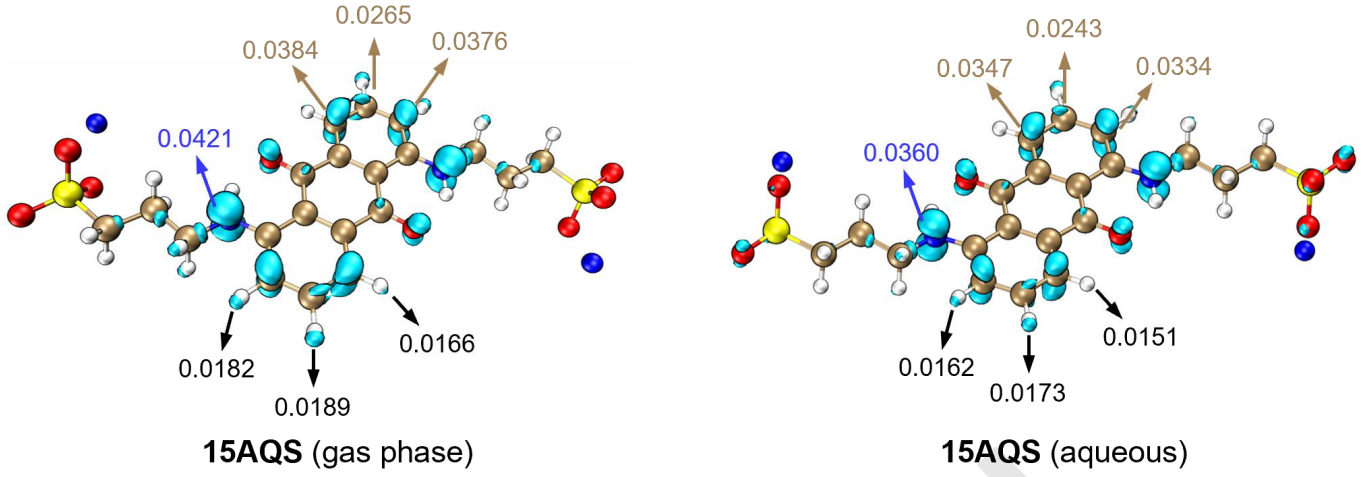

Figure S58 CFF calculations of **15AQS** in the gas phase and aqueous solution.

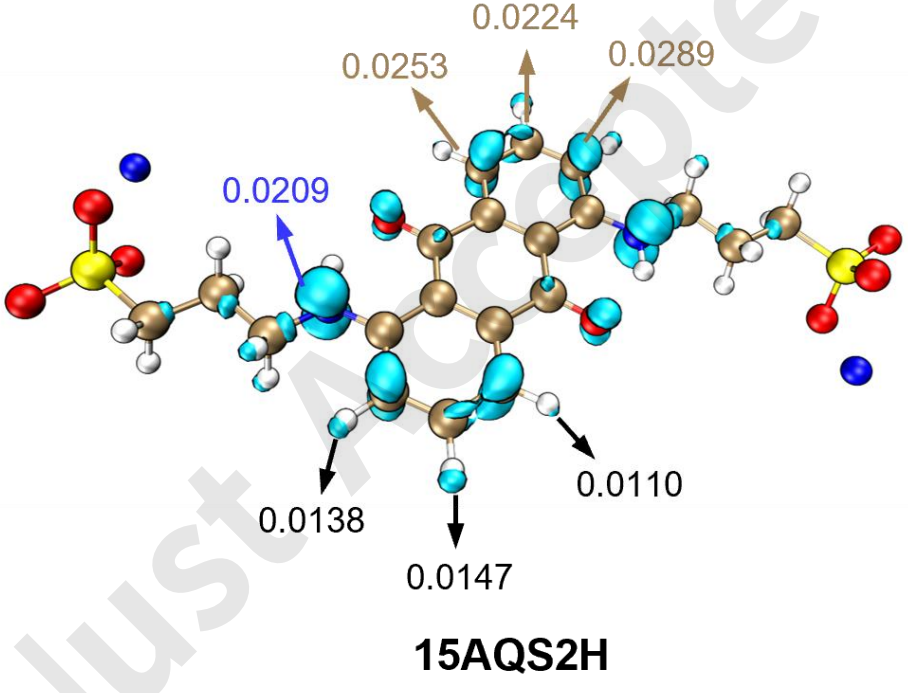

Figure S59 CFF calculations of **15AQS2H** in the aqueous solution.

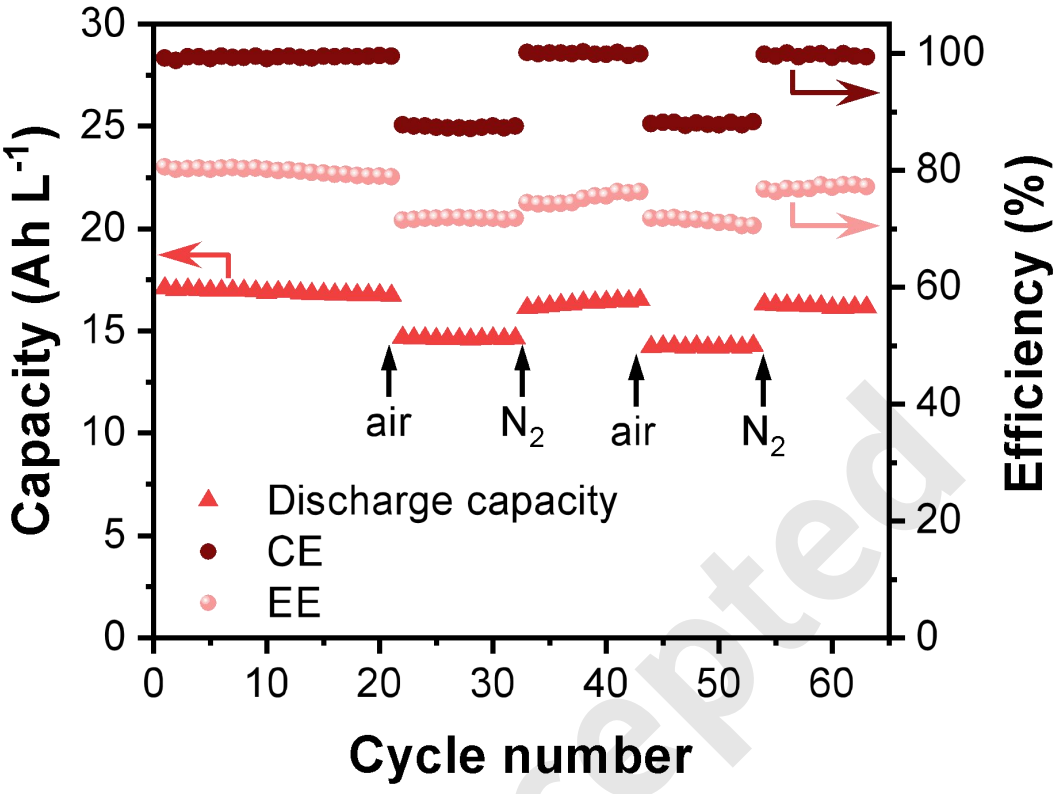

Figure S60 Cycling performances of 0.5 M **15AQS**||$Na_4[Fe(CN)_6]$ AORFBs in 1.0 M NaOH solutions at a current density of 100 mA cm^{-2} ranging from 1.7 to 0.4 V with replacing the atmosphere with air after the 20th and 42th cycles, and replacing the atmosphere with N_2 after the 32th and 54th cycles.

AQs	△E (eV)	$\triangle E_{1e}$ (eV)	$\triangle E_{2e}$ (eV)	Dipole Moment (D)	Hardness (η)	Softness (σ)	Electronegativity (χ)
14AQ	2.55	1.73	0.36	6.72	1.28	0.78	4.14
14AQS	2.34	1.48	0.42	25.40	1.17	0.85	4.07
15AQ	3.12	2.09	0.57	0.002	1.56	0.64	4.40
15AQS	2.76	1.90	0.28	0.003	1.38	0.72	4.39
26AQ	3.01	2.05	0.56	1.82	1.51	0.66	4.46
26AQS	2.90	1.92	0.46	9.05	1.45	0.69	4.32
27AQ	2.91	1.97	0.58	3.83	1.46	0.69	4.47
27AQS	2.74	1.78	0.55	5.86	1.37	0.73	4.33

Table. S1 HOMO and LUMO energy values of AQ and AQs in different valence states.

	15AQS	**26AQS**
D	1.22×10^{-6} cm^2 s^{-1}	9.26×10^{-7} cm^2 s^{-1}
k_0	4.38×10^{-3} cm s^{-1}	1.33×10^{-3} cm s^{-1}

Table. S2 The values of the diffusion coefficient (D) and the rate constant (k_0) for **15AQS** and **26AQS**, as determined from rotating disk electrode (RDE) measurements.

14AQ				
Center Number	Atomic Number	Coordinates (Angstroms)		
		X	Y	Z
1	6	-3.367246	0.677716	0.000072
2	6	-2.148073	1.426427	0.000097
3	6	-0.919118	0.724799	0.000031
4	6	-0.919231	-0.72505	-0.000073
5	6	-2.148534	-1.426275	-0.000101
6	6	-3.367448	-0.677106	-0.000054
7	6	0.325377	1.462732	-0.00011
8	6	0.3254	-1.462951	0.000038
9	6	1.593663	-0.702667	0.00003
10	6	1.593668	0.702509	-0.000069
11	6	2.813169	1.393223	-0.000081
12	1	2.80351	2.475115	-0.000134
13	6	4.014434	0.699554	-0.000023
14	6	4.014433	-0.699712	0.00004
15	6	2.813166	-1.393377	0.000074
16	1	-4.304041	1.223755	0.000138
17	1	-4.304425	-1.222836	-0.000104
18	1	4.952263	1.242165	-0.000019
19	1	4.952261	-1.242326	0.000056
20	1	2.803505	-2.475272	0.00013
21	8	0.369805	-2.718905	0.000177
22	8	0.369368	2.718696	-0.000087
23	7	-2.247144	-2.77272	-0.000409
24	1	-3.15835	-3.205074	0.000773
25	1	-1.397195	-3.321522	0.000612

26	7	-2.245806	2.772947	0.000404
27	1	-3.15671	3.205925	-0.000738
28	1	-1.395521	3.321223	-0.000632

14AQ$^-$

Center Number	Atomic Number	Coordinates (Angstroms)		
		X	Y	Z
1	6	3.357904	-0.691804	0.000515
2	6	2.162978	-1.426562	0.00073
3	6	0.911041	-0.728834	0.000055
4	6	0.911028	0.728795	-0.000262
5	6	2.162918	1.426579	-0.000723
6	6	3.357878	0.691881	-0.000294
7	6	-0.327743	-1.464059	-0.00051
8	6	-0.32773	1.464029	0.000142
9	6	-1.56932	0.709893	0.000153
10	6	-1.569323	-0.709908	-0.000318
11	6	-2.807931	-1.392752	-0.000468
12	1	-2.800065	-2.475067	-0.000822
13	6	-4.003693	-0.705432	-0.000139
14	6	-4.003692	0.705416	0.000363
15	6	-2.80793	1.392737	0.000507
16	1	4.298799	-1.232124	0.001
17	1	4.298749	1.232241	-0.000614
18	1	-4.942694	-1.247244	-0.000247
19	1	-4.942693	1.247227	0.00062
20	1	-2.800061	2.47505	0.000862
21	8	-0.379615	2.754054	0.00095
22	8	-0.379709	-2.754078	-0.000871

23	7	2.23459	2.794062	-0.00226
24	1	3.135472	3.243607	0.001306
25	1	1.363612	3.309786	0.000609
26	7	2.23478	-2.794036	0.002257
27	1	3.135708	-3.243494	-0.001095
28	1	1.363856	-3.309845	-0.000748

14AQ^{2-}

Center Number	Atomic Number	Coordinates (Angstroms)		
		X	Y	Z
1	6	3.349001	-0.703959	-0.056108
2	6	2.173707	-1.421106	-0.087845
3	6	0.901488	-0.73298	-0.005543
4	6	0.901488	0.732986	0.005519
5	6	2.17371	1.421107	0.087847
6	6	3.349002	0.703955	0.05613
7	6	-0.328853	-1.466711	0.072832
8	6	-0.328856	1.466712	-0.072875
9	6	-1.545084	0.718486	-0.043105
10	6	-1.545083	-0.718487	0.043088
11	6	-2.80167	-1.390244	0.087672
12	1	-2.797525	-2.471152	0.153795
13	6	-3.993832	-0.709455	0.044677
14	6	-3.993834	0.709452	-0.044648
15	6	-2.801673	1.390242	-0.087665
16	1	4.292899	-1.236726	-0.124647
17	1	4.2929	1.236718	0.124689
18	1	-4.933745	-1.250072	0.076179
19	1	-4.933747	1.250068	-0.076132

20	1	-2.79753	2.47115	-0.153789
21	8	-0.379808	2.78935	-0.186345
22	8	-0.379793	-2.789346	0.186339
23	7	2.223106	2.817778	0.285211
24	1	3.044954	3.244259	-0.123929
25	1	1.341607	3.245803	-0.001933
26	7	2.223095	-2.817779	-0.285202
27	1	3.044934	-3.244264	0.123952
28	1	1.34159	-3.245796	0.001933

15AQ

Center Number	Atomic Number	Coordinates (Angstroms)		
		X	Y	Z
1	6	-3.300256	-1.7706	0.000054
2	6	-3.742377	-0.468678	0.000065
3	6	-2.826928	0.613748	0.000016
4	6	-1.427511	0.326392	-0.000044
5	6	-1.004995	-1.030868	-0.000061
6	6	-1.92841	-2.062714	-0.000009
7	6	-0.440934	1.392211	-0.000084
8	6	1.004996	1.03087	-0.000038
9	6	1.427511	-0.32639	-0.00006
10	6	0.440935	-1.392209	-0.000143
11	6	1.928412	2.062715	0.000032
12	6	3.300258	1.770598	0.000089
13	6	3.742377	0.468676	0.000076
14	6	2.826927	-0.613748	0.000001
15	8	0.766268	-2.596172	0.000022
16	8	-0.766265	2.596174	-0.000014

17	7	3.315677	-1.874037	-0.00002
18	7	-3.315684	1.874035	0.000027
19	1	-4.021033	-2.579797	0.000092
20	1	-4.802828	-0.243181	0.000113
21	1	-1.585701	-3.08746	-0.000023
22	1	1.585704	3.087461	0.000045
23	1	4.021036	2.579795	0.000147
24	1	4.802828	0.243177	0.00012
25	1	2.671505	-2.651754	-0.000095
26	1	4.313074	-2.021837	0.000002
27	1	-2.671515	2.651754	0.000011
28	1	-4.313081	2.021831	0.000107

15AQ$^-$

Center Number	Atomic Number	Coordinates (Angstroms)		
		X	Y	Z
1	6	3.288105	1.78113	0.000112
2	6	3.732687	0.459765	0.000124
3	6	2.822591	-0.60668	0.000016
4	6	1.408361	-0.331849	-0.000102
5	6	0.982614	1.035257	-0.00011
6	6	1.934184	2.073132	-0.000003
7	6	0.431598	-1.39468	-0.000194
8	6	-0.982614	-1.035257	-0.000085
9	6	-1.408361	0.331848	-0.000102
10	6	-0.431598	1.39468	-0.000223
11	6	-1.934184	-2.073132	0.000038
12	6	-3.288105	-1.78113	0.000139
13	6	-3.732687	-0.459765	0.000126

14	6	-2.822591	0.60668	0.000011
15	8	-0.766359	2.635538	-0.000012
16	8	0.766358	-2.635538	0.000076
17	7	-3.29409	1.885914	0.000006
18	7	3.294091	-1.885914	0.000006
19	1	4.01565	2.585583	0.000196
20	1	4.793946	0.234893	0.000211
21	1	1.591749	3.098346	-0.000011
22	1	-1.591749	-3.098346	0.000049
23	1	-4.01565	-2.585583	0.00023
24	1	-4.793946	-0.234893	0.000206
25	1	-2.616545	2.637929	-0.000129
26	1	-4.287208	2.053095	0.000054
27	1	2.616545	-2.637929	-0.000049
28	1	4.287208	-2.053094	0.000154

15AQ^{2-}

Center Number	Atomic Number	Coordinates (Angstroms)		
		X	Y	Z
1	6	3.276255	1.795857	0.000031
2	6	3.725892	0.456772	0.000033
3	6	2.820059	-0.597953	-0.000009
4	6	1.389547	-0.341417	-0.000037
5	6	0.956755	1.040486	-0.00004
6	6	1.93437	2.083559	-0.000006
7	6	0.428533	-1.400796	-0.000036
8	6	-0.956755	-1.040486	-0.000005
9	6	-1.389547	0.341417	-0.000026
10	6	-0.428533	1.400797	-0.000055

11	6	-1.93437	-2.083558	0.000036
12	6	-3.276254	-1.795857	0.000052
13	6	-3.725892	-0.456773	0.00003
14	6	-2.820059	0.597953	-0.000007
15	8	-0.771993	2.686547	-0.000058
16	8	0.771994	-2.686547	0.00012
17	7	-3.275273	1.893065	-0.000021
18	7	3.275271	-1.893066	-0.000046
19	1	4.006889	2.598841	0.000061
20	1	4.78816	0.23312	0.000057
21	1	1.589715	3.108789	-0.000003
22	1	-1.589714	-3.108789	0.00005
23	1	-4.006888	-2.598841	0.000082
24	1	-4.78816	-0.233121	0.000043
25	1	-2.563125	2.619946	-0.000072
26	1	-4.264437	2.078825	-0.000043
27	1	2.563123	-2.619946	-0.000046
28	1	4.264435	-2.078826	0.00007

26AQ

Center Number	Atomic Number	Coordinates (Angstroms)		
		X	Y	Z
1	6	-3.537792	-1.256325	0.005678
2	6	-3.7639	0.1372	0.002913
3	6	-2.650118	0.999836	-0.003285
4	6	-1.359286	0.497238	-0.006802
5	6	-1.13598	-0.898384	-0.005995
6	6	-2.250914	-1.752681	0.001065
7	6	-0.214327	1.455487	-0.008197

8	6	1.135986	0.898398	-0.005999
9	6	1.35928	-0.497225	-0.006858
10	6	0.214327	-1.455467	-0.008285
11	6	2.25093	1.752682	0.001087
12	6	3.537803	1.256312	0.005678
13	6	3.763896	-0.137215	0.002903
14	6	2.650105	-0.999838	-0.003351
15	8	0.419754	-2.676689	-0.010319
16	8	-0.419753	2.676713	-0.010394
17	7	5.031913	-0.64133	-0.032634
18	7	-5.031919	0.641301	-0.032662
19	1	-4.386964	-1.930107	0.013764
20	1	-2.090022	-2.823215	0.005513
21	1	2.090051	2.823218	0.005538
22	1	4.386982	1.930085	0.013743
23	1	5.165677	-1.617821	0.186918
24	1	5.79949	-0.026719	0.196593
25	1	-5.165709	1.617781	0.186913
26	1	-5.799505	0.026672	0.196485
27	1	2.808574	-2.070956	-0.003047
28	1	-2.808602	2.070952	-0.002958

$26AQ^-$

Center Number	Atomic Number	Coordinates (Angstroms)		
		X	Y	Z
1	6	3.520103	1.260961	0.005903
2	6	3.753388	-0.138324	0.008627
3	6	2.661926	-0.997335	0.006817
4	6	1.339478	-0.51215	0.00478

5	6	1.108937	0.895488	0.00277
6	6	2.235789	1.751093	0.001488
7	6	0.227158	-1.453087	0.001654
8	6	-1.108937	-0.895488	-0.00277
9	6	-1.339478	0.51215	-0.00478
10	6	-0.227158	1.453087	-0.001654
11	6	-2.235789	-1.751093	-0.001488
12	6	-3.520103	-1.260961	-0.005903
13	6	-3.753388	0.138324	-0.008627
14	6	-2.661926	0.997335	-0.006817
15	8	-0.428881	2.716052	-0.003252
16	8	0.428881	-2.716052	0.003252
17	7	5.058246	-0.620507	0.071204
18	7	-5.058246	0.620507	-0.071204
19	1	4.36759	1.938166	0.004466
20	1	2.826552	-2.068249	0.00548
21	1	2.071869	2.821486	-0.004591
22	1	-2.071869	-2.821486	0.004591
23	1	-4.36759	-1.938166	-0.004466
24	1	-2.826552	2.068249	-0.00548
25	1	5.760791	0.003326	-0.304078
26	1	5.177211	-1.571245	-0.253607
27	1	-5.760791	-0.003326	0.304078
28	1	-5.177211	1.571245	0.253607

$26AQ^{2-}$

Center Number	Atomic Number	Coordinates (Angstroms)		
		X	Y	Z
1	6	3.505485	1.269619	0.009168

2	6	3.744037	-0.137435	0.009995
3	6	2.66773	-0.994325	0.005184
4	6	1.317775	-0.528094	0.004951
5	6	1.080612	0.900003	0.002434
6	6	2.222914	1.752751	0.001979
7	6	0.235451	-1.457467	0.002227
8	6	-1.080612	-0.900003	-0.002434
9	6	-1.317775	0.528094	-0.004951
10	6	-0.235451	1.457467	-0.002227
11	6	-2.222914	-1.752751	-0.001979
12	6	-3.505485	-1.269619	-0.009168
13	6	-3.744037	0.137435	-0.009995
14	6	-2.66773	0.994325	-0.005184
15	8	-0.439679	2.769569	-0.00374
16	8	0.439679	-2.769569	0.00374
17	7	5.075034	-0.60181	0.081538
18	7	-5.075034	0.60181	-0.081538
19	1	4.351896	1.949435	0.011058
20	1	2.839259	-2.065159	0.001894
21	1	2.056459	2.823448	-0.00411
22	1	-2.056459	-2.823448	0.00411
23	1	-4.351896	-1.949435	-0.011058
24	1	-2.839259	2.065159	-0.001894
25	1	5.732891	0.009755	-0.387527
26	1	5.181976	-1.551584	-0.254346
27	1	-5.732891	-0.009755	0.387527
28	1	-5.181976	1.551584	0.254346
27AQ				

Center Number	Atomic Number	Coordinates (Angstroms)		
		X	Y	Z
1	6	3.686263	0.889455	0.000991
2	6	2.48813	1.577689	-0.000885
3	6	1.258848	0.903683	0.001448
4	6	1.271916	-0.507809	0.002781
5	6	2.47245	-1.204139	0.005116
6	6	3.701706	-0.520777	0.005724
7	6	0	1.662253	-0.000008
8	6	0	-1.277107	-0.000043
9	6	-1.271916	-0.507809	-0.002814
10	6	-1.258848	0.903683	-0.001462
11	6	-2.488131	1.577688	0.000897
12	1	-2.4917	2.660237	0.006359
13	6	-3.686263	0.889455	-0.000966
14	6	-3.701707	-0.520777	-0.00571
15	6	-2.47245	-1.204139	-0.00513
16	1	4.626983	1.428506	-0.002856
17	1	-4.626983	1.428505	0.002904
18	1	-2.462139	-2.287106	-0.005249
19	8	0	-2.506995	0.000015
20	8	0	2.905387	-0.000008
21	7	4.884354	-1.210967	0.05597
22	1	4.866644	-2.187752	-0.201139
23	1	5.725349	-0.714732	-0.202877
24	7	-4.884355	-1.210967	-0.055942
25	1	-4.866641	-2.187755	0.201153
26	1	-5.725346	-0.714734	0.202921

27	1	2.46214	-2.287106	0.005221
28	1	2.4917	2.660237	-0.006334

27AQ$^-$

Center Number	Atomic Number	Coordinates (Angstroms)		
		X	Y	Z
1	6	-3.674941	0.894311	-0.004745
2	6	-2.48066	1.577413	-0.000917
3	6	-1.23799	0.906803	-0.002681
4	6	-1.242007	-0.519872	-0.003963
5	6	-2.473766	-1.204941	-0.005664
6	6	-3.68539	-0.524038	-0.008035
7	6	0	1.664633	-0.000265
8	6	0	-1.274438	-0.00016
9	6	1.242007	-0.519872	0.003765
10	6	1.23799	0.906803	0.002456
11	6	2.48066	1.577413	0.000923
12	1	2.483412	2.66046	-0.004822
13	6	3.674941	0.894311	0.00494
14	6	3.68539	-0.524038	0.008213
15	6	2.473765	-1.204941	0.005652
16	1	-4.617693	1.431011	-0.003208
17	1	4.617693	1.431011	0.003551
18	1	2.470525	-2.288385	0.004168
19	8	0	-2.556442	-0.000169
20	8	-0.000001	2.939469	0.000068
21	7	-4.896955	-1.203419	-0.07092
22	1	-4.869367	-2.162982	0.24817
23	1	-5.692716	-0.696915	0.294572

24	7	4.896944	-1.20342	0.071281
25	1	4.869407	-2.16298	-0.247823
26	1	5.692762	-0.696912	-0.294083
27	1	-2.470525	-2.288385	-0.004169
28	1	-2.483411	2.660459	0.004814

27AQ^{2-}

Center Number	Atomic Number	Coordinates (Angstroms)		
		X	Y	Z
1	6	3.665923	0.899279	0.009412
2	6	2.474142	1.577489	0.003433
3	6	1.214971	0.915928	0.003269
4	6	1.213303	-0.532709	0.004225
5	6	2.475405	-1.205815	0.003998
6	6	3.673393	-0.527971	0.009409
7	6	0	1.672819	-0.00003
8	6	0	-1.279434	0.00003
9	6	-1.213303	-0.53271	-0.004205
10	6	-1.214971	0.915928	-0.003285
11	6	-2.474142	1.577489	-0.00346
12	1	-2.480716	2.661157	0.001326
13	6	-3.665923	0.899279	-0.009423
14	6	-3.673393	-0.527971	-0.009394
15	6	-2.475405	-1.205815	-0.003966
16	1	4.609751	1.435327	0.011945
17	1	-4.609751	1.435327	-0.011969
18	1	-2.481861	-2.289937	0.000375
19	8	0	-2.617032	-0.000061
20	8	0	2.990835	0.000026

21	7	4.910153	-1.198197	0.07956
22	1	4.868304	-2.154128	-0.252599
23	1	5.663424	-0.69761	-0.376885
24	7	-4.910153	-1.198198	-0.079537
25	1	-4.868305	-2.154124	0.25264
26	1	-5.663425	-0.697604	0.376896
27	1	2.481861	-2.289937	-0.000312
28	1	2.480716	2.661157	-0.001381

Table. S3 XYZ Coordinates of the optimized structures for various AQ (SMD = water), used for calculating molecular orbital energies, electrostatic potential (ESP), and Fukui functions calculations.

14AQS				
Center Number	Atomic Number	Coordinates (Angstroms)		
		X	Y	Z
1	6	0.678447	-1.07618	-0.418422
2	6	-0.678492	-1.076162	-0.418471
3	6	-1.432777	0.129159	-0.261614
4	6	-0.724064	1.356118	-0.119839
5	6	0.724064	1.3561	-0.11979
6	6	1.432756	0.129119	-0.261506
7	6	-1.458361	2.593062	0.023122
8	6	-0.702353	3.854538	0.146869
9	6	0.702394	3.854527	0.146863
10	6	1.45838	2.593028	0.023224
11	6	-1.393323	5.068963	0.26532
12	6	-0.699822	6.264175	0.381292
13	6	0.699908	6.264163	0.381295
14	6	1.393386	5.068938	0.26532
15	8	2.718048	2.639031	0.043859
16	8	-2.718029	2.639087	0.043678
17	7	2.779628	0.058987	-0.255132
18	7	-2.77965	0.059059	-0.255393
19	6	-3.556063	-1.16419	-0.402702
20	6	-5.041704	-0.841472	-0.286979
21	6	-5.865422	-2.1096	-0.465018
22	16	-7.633212	-1.823046	-0.262647
23	8	-7.853761	-1.36684	1.158638
24	8	-8.303291	-3.163062	-0.43461

25	8	-8.051123	-0.819474	-1.272408
26	6	3.556054	-1.164208	-0.402831
27	6	5.041678	-0.841537	-0.28675
28	6	5.865435	-2.109594	-0.465105
29	16	7.633217	-1.823022	-0.262681
30	8	8.303341	-3.16299	-0.434821
31	8	8.051102	-0.819303	-1.272308
32	8	7.853726	-1.366981	1.158667
33	11	9.084816	-3.252525	1.759571
34	11	-9.084892	-3.252392	1.759573
35	1	1.20284	-2.013469	-0.540177
36	1	-1.202905	-2.013437	-0.540251
37	1	-1.242229	7.197816	0.471492
38	1	1.242332	7.197793	0.471499
39	1	2.475201	5.060085	0.263731
40	1	3.257002	0.950784	-0.148832
41	1	-3.257019	0.950809	-0.148673
42	1	-3.350452	-1.629301	-1.37259
43	1	-3.274816	-1.884884	0.37144
44	1	-5.241261	-0.400564	0.692886
45	1	-5.317769	-0.108299	-1.048515
46	1	-5.754164	-2.533584	-1.464706
47	1	-5.609551	-2.870872	0.27395
48	1	3.274691	-1.885212	0.370972
49	1	3.350596	-1.628927	-1.372945
50	1	5.31786	-0.108086	-1.047978
51	1	5.241078	-0.400982	0.693304
52	1	5.609587	-2.871058	0.273672

53	1	5.754192	-2.533332	-1.464899
54	1	-2.475138	5.060132	0.263711

14AQS$^-$

Center Number	Atomic Number	Coordinates (Angstroms)		
		X	Y	Z
1	6	0.694305	-1.066963	0.028459
2	6	-0.694353	-1.066956	0.028477
3	6	-1.431537	0.121421	0.103467
4	6	-0.727484	1.377748	0.117953
5	6	0.72746	1.377736	0.117963
6	6	1.4315	0.121406	0.103448
7	6	-1.46004	2.619517	0.100522
8	6	-0.708695	3.862736	0.10316
9	6	0.708733	3.86272	0.103154
10	6	1.460047	2.619482	0.10059
11	6	-1.392811	5.100071	0.102745
12	6	-0.705035	6.295985	0.104
13	6	0.705127	6.295969	0.103978
14	6	1.392876	5.10004	0.10271
15	8	2.749333	2.676403	0.074329
16	8	-2.74933	2.676489	0.074613
17	7	2.80399	0.071317	0.18125
18	7	-2.804028	0.071334	0.181254
19	6	-3.557234	-1.125542	-0.146257
20	6	-5.052672	-0.825535	-0.112285
21	6	-5.844811	-2.077842	-0.46304
22	16	-7.627615	-1.822265	-0.407553
23	8	-7.987522	-1.461313	1.012681

24	8	-8.255719	-3.156996	-0.725132
25	8	-7.970873	-0.760454	-1.385958
26	6	3.557201	-1.125553	-0.146274
27	6	5.052638	-0.82554	-0.112281
28	6	5.84479	-2.077815	-0.463118
29	16	7.627591	-1.822246	-0.407489
30	8	8.255724	-3.156927	-0.725218
31	8	7.97091	-0.760297	-1.385724
32	8	7.987415	-1.461489	1.012817
33	11	9.204783	-3.405101	1.392908
34	11	-9.204675	-3.405009	1.393064
35	1	1.212097	-2.01524	-0.014709
36	1	-1.212155	-2.015227	-0.014693
37	1	-1.246849	7.234955	0.105382
38	1	1.246963	7.234927	0.105347
39	1	2.475074	5.092023	0.10239
40	1	3.244526	0.978817	0.043126
41	1	-3.24455	0.978834	0.043071
42	1	-3.28058	-1.506466	-1.139505
43	1	-3.332589	-1.921735	0.571138
44	1	-5.332053	-0.475562	0.884547
45	1	-5.281988	-0.028142	-0.823922
46	1	-5.636804	-2.423864	-1.477309
47	1	-5.650235	-2.893345	0.236002
48	1	3.332549	-1.921755	0.571109
49	1	3.280557	-1.506464	-1.139529
50	1	5.281947	-0.028098	-0.823865
51	1	5.332014	-0.475629	0.884574

52	1	5.65017	-2.893389	0.235829
53	1	5.636844	-2.423732	-1.477434
54	1	-2.475009	5.092078	0.102432

14AQS^{2-}

Center Number	Atomic Number	Coordinates (Angstroms)		
		X	Y	Z
1	6	-0.682418	-1.360545	-0.51714
2	6	0.731141	-1.285877	-0.585842
3	6	1.389643	-0.075118	-0.575731
4	6	0.638091	1.154374	-0.355363
5	6	-0.822675	1.075478	-0.275434
6	6	-1.459357	-0.226006	-0.434389
7	6	1.314721	2.402983	-0.166079
8	6	0.513129	3.570181	0.032781
9	6	-0.919065	3.4916	0.115713
10	6	-1.604692	2.2424	0.005232
11	6	1.12726	4.847406	0.182118
12	6	0.391863	5.98908	0.390896
13	6	-1.024217	5.911689	0.469504
14	6	-1.649273	4.695109	0.338981
15	8	-2.9218	2.213244	0.189833
16	8	2.639736	2.520964	-0.142536
17	7	-2.855861	-0.301528	-0.546744
18	7	2.769753	-0.009569	-0.811274
19	6	3.598494	-1.165483	-0.515915
20	6	5.073676	-0.775282	-0.547757
21	6	5.949629	-1.98504	-0.250334
22	16	7.706956	-1.587472	-0.216748

23	8	8.079188	-1.0407	-1.545568
24	8	8.428991	-2.867883	0.12592
25	8	7.926321	-0.610826	0.912482
26	6	-3.533525	-1.531294	-0.172447
27	6	-5.04021	-1.296469	-0.113297
28	6	-5.767395	-2.564666	0.313412
29	16	-7.556162	-2.351242	0.377681
30	8	-8.137662	-3.641159	0.824023
31	8	-7.833443	-1.206858	1.321358
32	8	-8.004903	-1.935622	-1.001911
33	11	-8.502519	0.25033	-0.367978
34	11	9.226855	-2.076118	2.167357
35	1	-1.151534	-2.333014	-0.596515
36	1	1.290256	-2.204377	-0.710873
37	1	0.888684	6.947768	0.494552
38	1	-1.607751	6.811655	0.631409
39	1	-2.728693	4.633512	0.3997
40	1	-3.268583	0.555859	-0.16662
41	1	3.128468	0.890718	-0.48041
42	1	3.354941	-1.592614	0.470048
43	1	3.420963	-1.959806	-1.249227
44	1	5.324686	-0.367915	-1.530019
45	1	5.257429	0.006608	0.19438
46	1	5.734613	-2.416239	0.729166
47	1	5.846404	-2.762784	-1.009641
48	1	-3.322661	-2.321024	-0.90113
49	1	-3.181085	-1.90422	0.802651
50	1	-5.253688	-0.493003	0.597409

51	1	-5.396078	-0.976641	-1.096281
52	1	-5.601182	-3.388821	-0.38308
53	1	-5.479937	-2.885909	1.316385
54	1	2.206737	4.904598	0.123829

15AQS

Center Number	Atomic Number	Coordinates (Angstroms)		
		X	Y	Z
1	6	-2.436477	-2.888154	-0.00028
2	6	-1.222408	-3.537413	-0.000474
3	6	-0.018777	-2.821255	-0.000266
4	6	-0.043301	-1.435768	0.000051
5	6	-1.274377	-0.728372	0.000178
6	6	-2.504487	-1.469689	0.000119
7	6	1.26567	-0.721337	0.000299
8	6	1.274421	0.728425	0.000139
9	6	0.043345	1.43582	-0.00001
10	6	-1.265628	0.721388	0.000263
11	6	2.504533	1.469742	0.000037
12	6	2.436525	2.888205	-0.000421
13	6	1.222455	3.537465	-0.000633
14	6	0.018823	2.82131	-0.000386
15	8	-2.31928	1.393103	0.000491
16	8	2.31932	-1.393054	0.000572
17	7	-3.705835	-0.853259	0.000438
18	7	3.705881	0.853311	0.000389
19	6	4.986488	1.54363	-0.000087
20	6	6.117996	0.522104	0.000131
21	6	7.465133	1.231622	-0.000109

22	16	8.856458	0.08577	-0.000017
23	8	10.09268	0.905399	0.00005
24	8	8.713032	-0.788821	1.220777
25	8	8.71319	-0.78886	-1.220787
26	6	-4.986437	-1.543591	-0.000095
27	6	-6.117959	-0.52208	0.000164
28	6	-7.465069	-1.231642	-0.000237
29	16	-8.856453	-0.085847	-0.000112
30	8	-10.092639	-0.905513	-0.000331
31	8	-8.713198	0.788578	1.220825
32	8	-8.713092	0.78902	-1.220698
33	11	-8.226397	2.713404	0.000311
34	11	8.226049	-2.713468	-0.000068
35	1	-3.351665	-3.46305	-0.000386
36	1	-1.200484	-4.621047	-0.000771
37	1	0.928625	-3.340489	-0.000353
38	1	3.351714	3.463103	-0.00056
39	1	1.200532	4.6211	-0.000983
40	1	-0.928576	3.340546	-0.000483
41	1	-3.683505	0.16073	0.000441
42	1	3.683548	-0.160678	0.000511
43	1	5.068052	2.18756	-0.882151
44	1	5.068338	2.188236	0.881461
45	1	6.032801	-0.114798	0.884361
46	1	6.032693	-0.115287	-0.883739
47	1	7.60186	1.851367	-0.88814
48	1	7.60198	1.85165	0.887709
49	1	-5.067982	-2.187476	-0.882197

50	1	-5.068287	-2.188245	0.881416
51	1	-6.032829	0.114737	0.88446
52	1	-6.032629	0.115403	-0.883638
53	1	-7.601711	-1.85129	-0.88835
54	1	-7.60198	-1.851767	0.887502

15AQS$^-$

Center Number	Atomic Number	Coordinates (Angstroms)		
		X	Y	Z
1	6	-2.414278	-2.89231	-0.225199
2	6	-1.180574	-3.545991	-0.238343
3	6	0.004584	-2.833656	-0.214924
4	6	-0.012356	-1.425115	-0.172616
5	6	-1.257077	-0.721755	-0.158499
6	6	-2.483164	-1.489947	-0.190195
7	6	1.266305	-0.722297	-0.140275
8	6	1.258029	0.719239	-0.08883
9	6	0.0133	1.422663	-0.088267
10	6	-1.265502	0.719385	-0.108664
11	6	2.483679	1.487499	-0.051007
12	6	2.415288	2.889739	-0.057686
13	6	1.18163	3.544186	-0.064697
14	6	-0.003489	2.831728	-0.071548
15	8	-2.356629	1.40153	-0.082272
16	8	2.357297	-1.404701	-0.16333
17	7	-3.689844	-0.859114	-0.193829
18	7	3.68987	0.854267	0.006477
19	6	4.963813	1.535453	-0.114295
20	6	6.09844	0.521711	-0.008665

21	6	7.447362	1.207142	-0.179593
22	16	8.829684	0.069628	0.032351
23	8	10.074	0.846926	-0.185222
24	8	8.714759	-0.509917	1.420785
25	8	8.638107	-1.051924	-0.958226
26	6	-4.962887	-1.5469	-0.115098
27	6	-6.094463	-0.527491	-0.036281
28	6	-7.441368	-1.232854	0.045784
29	16	-8.82185	-0.079794	0.162375
30	8	-10.062461	-0.890217	0.23189
31	8	-8.589073	0.770761	1.386527
32	8	-8.754615	0.817379	-1.049005
33	11	-8.122434	2.701756	0.173181
34	11	8.084125	-2.626328	0.665572
35	1	-3.326522	-3.472409	-0.246535
36	1	-1.158898	-4.63015	-0.267648
37	1	0.955079	-3.347535	-0.224985
38	1	3.327457	3.470268	-0.048177
39	1	1.160311	4.628737	-0.063732
40	1	-0.953938	3.345833	-0.072368
41	1	-3.641834	0.153231	-0.107589
42	1	3.639706	-0.155222	-0.110474
43	1	5.031681	2.073306	-1.069551
44	1	5.069883	2.282994	0.6791
45	1	6.050407	0.03186	0.967457
46	1	5.973965	-0.246192	-0.77687
47	1	7.569794	1.631562	-1.177697
48	1	7.60578	1.992996	0.561439

49	1	-5.106539	-2.189595	-0.99181
50	1	-4.994403	-2.200598	0.765864
51	1	-5.951215	0.102688	0.845582
52	1	-6.06573	0.117121	-0.918633
53	1	-7.644007	-1.83671	-0.840785
54	1	-7.519838	-1.866566	0.931183

15AQS^{2-}

Center Number	Atomic Number	Coordinates (Angstroms)		
		X	Y	Z
1	6	2.577728	-2.721889	-0.380782
2	6	1.417003	-3.485717	-0.198578
3	6	0.17701	-2.850714	-0.046579
4	6	0.097735	-1.451886	-0.076832
5	6	1.258444	-0.688055	-0.25915
6	6	2.498459	-1.323059	-0.411025
7	6	-1.142251	-0.816893	0.075243
8	6	-1.221548	0.581929	0.044952
9	6	-0.060872	1.345764	-0.137548
10	6	1.179132	0.710773	-0.289575
11	6	-2.461527	1.216906	0.197175
12	6	-2.540862	2.615728	0.166717
13	6	-1.380202	3.379568	-0.015895
14	6	-0.140204	2.744587	-0.168006
15	8	2.363506	1.490194	-0.475746
16	8	-2.326635	-1.596316	0.261341
17	7	3.716039	-0.521866	-0.602028
18	7	-3.678965	0.415644	0.388831
19	6	-4.831896	1.133905	-0.173082

20	6	-6.107256	0.294455	0.027891
21	6	-7.315151	1.04688	-0.560698
22	16	-8.78924	0.076593	-0.328296
23	8	-9.94194	0.794603	-0.889961
24	8	-8.637448	-1.216118	-1.010632
25	8	-9.03483	-0.180664	1.303394
26	6	4.868557	-1.240321	-0.039499
27	6	6.144151	-0.400984	-0.239423
28	6	7.351507	-1.153684	0.349933
29	16	8.825907	-0.183538	0.118941
30	8	9.97806	-0.901845	0.68135
31	8	9.043213	0.043182	-1.316711
32	8	8.65299	1.285278	0.894558
33	11	10.359337	2.408017	0.627285
34	11	-10.74078	-1.303593	1.572399
35	1	3.524498	-3.206727	-0.496804
36	1	1.477526	-4.553754	-0.175511
37	1	-0.709227	-3.433911	0.09258
38	1	-3.48762	3.10055	0.282895
39	1	-1.440777	4.447598	-0.039178
40	1	0.745988	3.327797	-0.307398
41	1	3.61254	0.357715	-0.137672
42	1	-3.575632	-0.463955	-0.075526
43	1	-4.942435	2.075105	0.323732
44	1	-4.674446	1.29876	-1.218516
45	1	-5.996723	-0.646739	-0.468934
46	1	-6.264663	0.129598	1.073331
47	1	-7.425672	1.988086	-0.063893

48	1	-7.157777	1.211717	-1.606146
49	1	4.710394	-1.40534	1.005802
50	1	4.97933	-2.181442	-0.536408
51	1	6.302341	-0.235954	-1.284718
52	1	6.033373	0.540136	0.25749
53	1	7.193294	-1.31874	1.395221
54	1	7.462298	-2.09479	-0.147003

26AQS

Center Number	Atomic Number	Coordinates (Angstroms)		
		X	Y	Z
1	6	-3.756066	-0.366121	-0.04772
2	6	-3.35123	-1.719639	-0.138116
3	6	-2.008706	-2.041198	-0.145014
4	6	-1.010779	-1.057196	-0.065196
5	6	-1.413426	0.298961	0.022858
6	6	-2.754035	0.63	0.032184
7	6	0.395493	-1.436306	-0.071526
8	6	1.406469	-0.34029	0.008775
9	6	1.004485	1.015835	0.09044
10	6	-0.402841	1.394722	0.105422
11	6	2.74805	-0.67012	-0.00296
12	6	3.749203	0.326538	0.063637
13	6	3.344358	1.680081	0.135697
14	6	2.001387	2.001234	0.152009
15	8	-0.766407	2.578006	0.18192
16	8	0.760394	-2.620131	-0.141724
17	7	-5.061688	-0.00547	-0.041744
18	7	5.058646	-0.037946	0.073453

19	6	6.158498	0.906109	-0.070735
20	6	7.490294	0.166497	-0.023266
21	6	8.636464	1.136129	-0.278295
22	16	10.254036	0.350764	-0.152587
23	8	11.264094	1.379243	-0.50146
24	8	10.386877	-0.170772	1.257008
25	8	10.250399	-0.831744	-1.08918
26	6	-6.173416	-0.943907	-0.062073
27	6	-7.493503	-0.183467	-0.0227
28	6	-8.664461	-1.156622	-0.032751
29	16	-10.260619	-0.319363	0.006696
30	8	-11.304025	-1.372531	0.00463
31	8	-10.27949	0.545826	1.242365
32	8	-10.316587	0.587068	-1.198112
33	1	-4.092328	-2.504666	-0.201604
34	1	-1.7115	-3.080192	-0.213422
35	1	4.084227	2.46752	0.17848
36	1	1.703988	3.040798	0.209566
37	1	-5.275209	0.974799	0.076794
38	1	5.259395	-1.004696	-0.14466
39	1	6.068255	1.455778	-1.015767
40	1	6.117033	1.640455	0.738211
41	1	7.608232	-0.307618	0.954462
42	1	7.49748	-0.619742	-0.783111
43	1	8.596729	1.559774	-1.283329
44	1	8.655592	1.950773	0.448389
45	1	-6.123701	-1.558181	-0.967031
46	1	-6.108276	-1.622856	0.795593

47	1	-7.530214	0.432227	0.879999
48	1	-7.555002	0.482332	-0.887517
49	1	-8.682027	-1.768773	-0.936428
50	1	-8.660332	-1.813026	0.83939
51	1	3.041833	-1.710785	-0.066555
52	1	-3.047617	1.670312	0.101585
53	11	-10.225978	2.549256	0.055064
54	11	10.306033	-2.411973	0.621451

26AQS$^-$

Center Number	Atomic Number	Coordinates (Angstroms)		
		X	Y	Z
1	6	-3.742431	-0.278065	-0.359454
2	6	-3.346251	-1.639652	-0.434637
3	6	-2.012929	-1.978239	-0.371313
4	6	-0.995349	-1.008651	-0.231087
5	6	-1.388955	0.362831	-0.155295
6	6	-2.753268	0.693319	-0.216994
7	6	0.3924	-1.411842	-0.161125
8	6	1.384257	-0.354795	-0.012856
9	6	0.991186	1.017018	0.05735
10	6	-0.396602	1.420177	-0.010878
11	6	2.74828	-0.685779	0.056714
12	6	3.737382	0.28517	0.200017
13	6	3.342315	1.647769	0.260794
14	6	2.009474	1.986878	0.192231
15	8	-0.745369	2.649627	0.051593
16	8	0.741274	-2.641213	-0.224619
17	7	-5.07597	0.094962	-0.464744

18	7	5.069412	-0.090653	0.323929
19	6	6.141434	0.845683	-0.006498
20	6	7.490621	0.142567	0.088534
21	6	8.616138	1.101347	-0.276718
22	16	10.246046	0.344348	-0.137181
23	8	11.240725	1.371691	-0.5315
24	8	10.397043	-0.125098	1.288819
25	8	10.250533	-0.871486	-1.031067
26	6	-6.140902	-0.860245	-0.168533
27	6	-7.489391	-0.149572	-0.150497
28	6	-8.608133	-1.149242	0.11093
29	16	-10.230077	-0.371965	0.225572
30	8	-11.220193	-1.459591	0.416762
31	8	-10.17822	0.602687	1.37637
32	8	-10.440043	0.41651	-1.043344
33	1	-4.090665	-2.417538	-0.541392
34	1	-1.728827	-3.021791	-0.427063
35	1	4.086928	2.425964	0.363689
36	1	1.726043	3.030994	0.240365
37	1	-5.256143	1.020594	-0.095674
38	1	5.244354	-1.026515	-0.021819
39	1	6.009082	1.261645	-1.01464
40	1	6.120744	1.682608	0.694829
41	1	7.633488	-0.230134	1.105912
42	1	7.501884	-0.716178	-0.589164
43	1	8.544269	1.445889	-1.309928
44	1	8.645134	1.969717	0.384337
45	1	-6.151449	-1.640224	-0.933977

46	1	-5.972591	-1.355218	0.797373
47	1	-7.483356	0.61701	0.630256
48	1	-7.65397	0.348611	-1.108901
49	1	-8.6955	-1.883198	-0.692421
50	1	-8.476491	-1.676464	1.057817
51	1	3.035909	-1.729177	-0.000283
52	1	-3.041509	1.736135	-0.153233
53	11	-10.350847	2.487185	0.017181
54	11	10.310066	-2.386832	0.737106

26AQS^{2-}

Center Number	Atomic Number	Coordinates (Angstroms)		
		X	Y	Z
1	6	3.710505	0.293417	-0.470507
2	6	3.294174	1.65432	-0.58628
3	6	1.967058	1.981121	-0.467072
4	6	0.949602	1.012041	-0.233057
5	6	1.365663	-0.370682	-0.117404
6	6	2.755219	-0.671619	-0.233249
7	6	-0.417814	1.411723	-0.118576
8	6	-1.365602	0.370606	0.11669
9	6	-0.949543	-1.01211	0.232365
10	6	0.417894	-1.411792	0.117931
11	6	-2.755153	0.67155	0.232473
12	6	-3.710467	-0.293484	0.469703
13	6	-3.294132	-1.654386	0.585502
14	6	-1.967001	-1.981181	0.466353
15	8	0.7865	-2.681957	0.227307
16	8	-0.786423	2.681904	-0.227893

17	7	5.065213	-0.060743	-0.657606
18	7	-5.065119	0.06074	0.656716
19	6	-6.092895	-0.839821	0.123591
20	6	-7.460798	-0.171604	0.203844
21	6	-8.544375	-1.102697	-0.323981
22	16	-10.179636	-0.344287	-0.30548
23	8	-11.141667	-1.361077	-0.796323
24	8	-10.448438	0.104688	1.109686
25	8	-10.106991	0.88512	-1.178206
26	6	6.092784	0.839586	-0.123576
27	6	7.460802	0.171628	-0.20398
28	6	8.544117	1.102574	0.324649
29	16	10.179471	0.344351	0.306369
30	8	11.14125	1.361092	0.797793
31	8	10.106716	-0.885322	1.178734
32	8	10.448747	-0.104195	-1.108834
33	1	4.024919	2.431733	-0.77235
34	1	1.671693	3.019818	-0.554598
35	1	-4.024867	-2.431809	0.771542
36	1	-1.67164	-3.019876	0.553908
37	1	5.22387	-1.006161	-0.325488
38	1	-5.223855	1.006039	0.324333
39	1	-5.880922	-1.118517	-0.918482
40	1	-6.106842	-1.761529	0.708485
41	1	-7.67528	0.09608	1.241414
42	1	-7.445249	0.750678	-0.385033
43	1	-8.372825	-1.387584	-1.363862
44	1	-8.637049	-2.007412	0.279797

45	1	6.106733	1.761718	-0.707799
46	1	5.880499	1.117482	0.918642
47	1	7.445274	-0.751021	0.384325
48	1	7.675539	-0.09538	-1.241668
49	1	8.636898	2.007596	-0.278651
50	1	8.372182	1.386934	1.364612
51	1	-3.067765	1.705795	0.136136
52	1	3.067837	-1.705864	-0.13693
53	11	10.270996	-2.371809	-0.605514
54	11	-10.270535	2.372092	0.605791

27AQS

Center Number	Atomic Number	Coordinates (Angstroms)		
		X	Y	Z
1	6	-3.672707	3.324576	0.236079
2	6	-3.892635	1.927884	0.300474
3	6	-2.774426	1.074775	0.224735
4	6	-1.491803	1.596293	0.097537
5	6	-1.277866	2.988266	0.035606
6	6	-2.398389	3.83269	0.107233
7	6	-0.345988	0.651306	0.024341
8	6	1.016475	1.229336	-0.117743
9	6	1.201432	2.630502	-0.17956
10	6	0.06824	3.558993	-0.106869
11	6	2.100507	0.371545	-0.186143
12	6	3.416345	0.867492	-0.319407
13	6	3.598573	2.267669	-0.376399
14	6	2.508092	3.116515	-0.308953
15	8	0.239089	4.791247	-0.164424

16	8	-0.51994	-0.565408	0.080054
17	7	-5.159498	1.446551	0.453917
18	7	4.459038	-0.003936	-0.408263
19	6	5.8544	0.406879	-0.334517
20	6	6.760408	-0.818046	-0.378514
21	6	8.220917	-0.393433	-0.306325
22	16	9.353329	-1.795845	-0.316254
23	8	10.742204	-1.219453	-0.203507
24	8	9.079501	-2.604521	0.927771
25	8	9.127017	-2.556387	-1.56987
26	6	-5.499203	0.040468	0.278121
27	6	-7.002558	-0.155696	0.435599
28	6	-7.362877	-1.620446	0.228938
29	16	-9.129863	-1.934332	0.396001
30	8	-9.327751	-3.402027	0.112928
31	8	-9.536239	-1.535913	1.766321
32	8	-9.830642	-1.149362	-0.685278
33	1	-2.899139	0.002363	0.265018
34	1	4.592418	2.682834	-0.473608
35	1	2.665775	4.186663	-0.353602
36	1	-5.906533	2.108905	0.293118
37	1	4.259189	-0.970134	-0.187834
38	1	6.084908	1.068089	-1.174866
39	1	6.038798	0.974296	0.586103
40	1	6.522035	-1.475469	0.462163
41	1	6.579637	-1.373443	-1.301782
42	1	8.511398	0.217637	-1.163087
43	1	8.444899	0.152738	0.611802

44	1	-5.178004	-0.312513	-0.709978
45	1	-4.969245	-0.557345	1.024607
46	1	-7.311015	0.167605	1.432492
47	1	-7.528167	0.463086	-0.296989
48	1	-7.100534	-1.970228	-0.771038
49	1	-6.885195	-2.26679	0.967777
50	1	1.941096	-0.698877	-0.136482
51	1	-2.251531	4.90394	0.056994
52	11	-10.581156	-3.03823	-1.82237
53	11	11.153458	-2.158284	1.890467
54	1	-4.525891	3.99201	0.287234

27AQS$^-$

Center Number	Atomic Number	Coordinates (Angstroms)		
		X	Y	Z
1	6	-3.660367	3.335447	0.286475
2	6	-3.875956	1.93437	0.409002
3	6	-2.777547	1.08247	0.350333
4	6	-1.466746	1.579277	0.17635
5	6	-1.26067	2.984503	0.051164
6	6	-2.392068	3.831276	0.112776
7	6	-0.353769	0.648338	0.117
8	6	0.973711	1.20481	-0.0953
9	6	1.17043	2.613671	-0.221148
10	6	0.060777	3.547104	-0.14636
11	6	2.084041	0.347553	-0.180807
12	6	3.375486	0.830647	-0.395713
13	6	3.564382	2.232703	-0.50959
14	6	2.483225	3.08376	-0.423332

15	8	0.241071	4.805495	-0.256781
16	8	-0.532952	-0.61551	0.242583
17	7	-5.167966	1.47676	0.612282
18	7	4.431611	-0.055393	-0.535484
19	6	5.813909	0.380455	-0.361404
20	6	6.747844	-0.822994	-0.425064
21	6	8.197046	-0.377756	-0.281834
22	16	9.354378	-1.759562	-0.303699
23	8	10.731573	-1.163358	-0.151457
24	8	9.072795	-2.603422	0.91524
25	8	9.164831	-2.49361	-1.579113
26	6	-5.499402	0.076219	0.375875
27	6	-7.003175	-0.140382	0.501164
28	6	-7.344085	-1.600945	0.237393
29	16	-9.109884	-1.941488	0.353129
30	8	-9.279959	-3.405991	0.034697
31	8	-9.55666	-1.577869	1.720757
32	8	-9.796075	-1.144258	-0.728866
33	1	-2.9091	0.013594	0.435958
34	1	4.554684	2.63888	-0.66612
35	1	2.641314	4.151534	-0.512383
36	1	-5.878098	2.122573	0.2899
37	1	4.244021	-0.970698	-0.145679
38	1	6.073934	1.084288	-1.15583
39	1	5.948983	0.904245	0.594594
40	1	6.492233	-1.522787	0.375933
41	1	6.611624	-1.340081	-1.377623
42	1	8.507419	0.269951	-1.104088

43	1	8.379538	0.136908	0.663342
44	1	-5.159425	-0.244866	-0.618503
45	1	-4.978484	-0.545444	1.108662
46	1	-7.333042	0.144434	1.502897
47	1	-7.523723	0.49811	-0.218436
48	1	-7.055727	-1.915189	-0.76724
49	1	-6.875643	-2.266696	0.964859
50	1	1.929715	-0.720795	-0.085193
51	1	-2.2441	4.899605	0.014718
52	11	-10.496348	-3.02301	-1.91604
53	11	11.128253	-2.168742	1.916589
54	1	-4.513893	4.003984	0.32735

27AQS^{2-}

Center Number	Atomic Number	Coordinates (Angstroms)		
		X	Y	Z
1	6	3.628524	3.335379	-0.203949
2	6	3.863559	1.930083	-0.344161
3	6	2.789902	1.066835	-0.299857
4	6	1.443971	1.528103	-0.132357
5	6	1.218254	2.95092	0.008096
6	6	2.355403	3.807609	-0.032966
7	6	0.370518	0.593405	-0.096141
8	6	-0.938362	1.127119	0.094294
9	6	-1.166483	2.5503	0.229493
10	6	-0.090756	3.495255	0.189873
11	6	-2.070814	0.259802	0.149686
12	6	-3.356321	0.720922	0.345555
13	6	-3.571711	2.127201	0.468798

14	6	-2.505076	2.989655	0.408702
15	8	-0.298002	4.790648	0.320579
16	8	0.577081	-0.719331	-0.232482
17	7	5.184465	1.510396	-0.560645
18	7	-4.431188	-0.181936	0.490267
19	6	-5.72204	0.173348	-0.107727
20	6	-6.712521	-0.973178	0.06407
21	6	-8.042657	-0.624159	-0.590463
22	16	-9.29964	-1.891886	-0.343725
23	8	-10.550958	-1.385139	-1.017665
24	8	-8.790695	-3.161254	-0.91954
25	8	-9.568714	-1.97465	1.138802
26	6	5.530013	0.113427	-0.326143
27	6	7.035748	-0.090741	-0.454124
28	6	7.39247	-1.54812	-0.193357
29	16	9.160598	-1.872273	-0.319192
30	8	9.347418	-3.335393	-0.002809
31	8	9.597328	-1.503839	-1.688979
32	8	9.84557	-1.069315	0.759633
33	1	2.942765	0.001233	-0.396351
34	1	-4.571204	2.515165	0.618688
35	1	-2.681365	4.054576	0.505622
36	1	5.854047	2.144587	-0.140162
37	1	-4.152253	-1.110138	0.189753
38	1	-6.117103	1.061864	0.386926
39	1	-5.615931	0.414878	-1.175288
40	1	-6.304684	-1.881417	-0.388538
41	1	-6.8601	-1.167586	1.129245

42	1	-8.473892	0.289744	-0.17733
43	1	-7.952473	-0.515149	-1.672889
44	1	5.193503	-0.219433	0.666891
45	1	5.014809	-0.51086	-1.060853
46	1	7.361326	0.198597	-1.45599
47	1	7.552612	0.551567	0.264981
48	1	7.113034	-1.866297	0.812588
49	1	6.926513	-2.218002	-0.918702
50	1	-1.905257	-0.807029	0.046381
51	1	2.19403	4.87354	0.07737
52	11	10.562766	-2.941216	1.945574
53	11	-11.746649	-1.170684	0.972187
54	1	4.474142	4.015571	-0.232632

Table. S4 XYZ Coordinates of the optimized structures for various AQs (SMD = water), used for calculating molecular orbital energies, electrostatic potential (ESP), and Fukui functions calculations.

15AQS2H				
Center Number	Atomic Number	Coordinates (Angstroms)		
		X	Y	Z
1	6	2.46333	2.83254	0.112753
2	6	1.234739	3.51906	0.077618
3	6	0.043689	2.845667	0.050403
4	6	0.026112	1.417502	0.045146
5	6	1.271682	0.684604	0.056313
6	6	2.518586	1.444209	0.117943
7	6	-1.195739	0.715995	0.008967
8	6	-1.271624	-0.684405	-0.057257
9	6	-0.026047	-1.417292	-0.046192
10	6	1.195803	-0.715778	-0.010011
11	6	-2.518501	-1.444014	-0.118684
12	6	-2.463237	-2.832334	-0.113612
13	6	-1.234641	-3.518858	-0.078753
14	6	-0.043598	-2.845444	-0.051634
15	8	2.377866	-1.438782	-0.016861
16	8	-2.377811	1.43897	0.01571
17	7	3.731635	0.807311	0.21492
18	7	-3.731613	-0.8071	-0.215352
19	6	-4.991029	-1.512801	-0.051645
20	6	-6.143943	-0.515194	-0.076524
21	6	-7.473057	-1.231832	0.119313
22	16	-8.877266	-0.101435	0.102577
23	8	-10.09758	-0.916337	0.319147
24	8	-8.635788	0.921071	1.185597
25	8	-8.857473	0.613274	-1.225682

26	6	4.99115	1.512921	0.051793
27	6	6.143972	0.515207	0.076882
28	6	7.473214	1.23171	-0.11859
29	16	8.877295	0.10117	-0.101643
30	8	10.097738	0.916008	-0.317897
31	8	8.857185	-0.613651	1.22651
32	8	8.635952	-0.921204	-1.184823
33	11	8.255243	-2.668128	0.307819
34	11	-8.255938	2.667949	-0.306812
35	1	3.380084	3.403507	0.142313
36	1	1.241119	4.603182	0.064755
37	1	-0.873728	3.416896	-0.002256
38	1	-3.379989	-3.403311	-0.142953
39	1	-1.24101	-4.602981	-0.066041
40	1	0.873842	-3.416649	0.00085
41	1	2.243962	-2.296155	-0.438791
42	1	-2.243883	2.296466	0.437385
43	1	3.735207	-0.176256	-0.008984
44	1	-3.735095	0.176346	0.009099
45	1	-5.1187	-2.241717	-0.858209
46	1	-5.005803	-2.07463	0.892238
47	1	-6.001171	0.222362	0.718205
48	1	-6.144751	0.016067	-1.031719
49	1	-7.67249	-1.952904	-0.675546
50	1	-7.525539	-1.743095	1.082218
51	1	5.006296	2.074883	-0.892003
52	1	5.118608	2.241733	0.858499
53	1	6.144478	-0.016139	1.032032

54	1	6.001297	-0.222243	-0.717969
55	1	7.525927	1.743044	-1.081442
56	1	7.672507	1.952743	0.676347

Table. S5 XYZ Coordinates of the optimized structures of **15AQS2H** (SMD = water), used for Fukui functions calculations.

14AQS				
Center Number	Atomic Number	Coordinates (Angstroms)		
		X	Y	Z
1	6	-0.70547	-1.19489	-0.8757
2	6	0.705163	-1.19499	-0.87572
3	6	1.434627	-0.01352	-0.6535
4	6	0.695407	1.309162	-0.40458
5	6	-0.69537	1.309275	-0.40456
6	6	-1.43478	-0.01332	-0.65346
7	6	1.471349	2.615639	-0.15872
8	6	0.701596	3.927232	0.0881
9	6	-0.70106	3.927364	0.088119
10	6	-1.47107	2.615901	-0.15868
11	6	1.402199	5.119915	0.312553
12	6	0.701289	6.312585	0.536997
13	6	-0.70025	6.312724	0.537017
14	6	-1.40141	5.120192	0.312594
15	8	-2.72947	2.612935	-0.15925
16	8	2.729745	2.612439	-0.15933
17	7	-2.77218	-0.04145	-0.65887
18	7	2.772021	-0.04176	-0.65893
19	6	3.479593	-1.30803	-0.89722
20	6	4.82897	-1.28949	-0.1553

21	6	5.570342	-2.61601	-0.40494
22	16	7.130031	-2.59448	0.452561
23	8	8.056985	-1.32429	-0.10982
24	8	7.837542	-3.86034	0.214332
25	8	6.894509	-2.42862	1.893651
26	6	-3.47979	-1.30771	-0.89715
27	6	-4.82917	-1.28919	-0.15525
28	6	-5.57049	-2.61574	-0.40488
29	16	-7.1302	-2.5943	0.452583
30	8	-7.83762	-3.86022	0.214383
31	8	-6.89474	-2.42836	1.893674
32	8	-8.05724	-1.3242	-0.10988
33	11	-7.06563	0.450303	0.22398
34	11	7.065232	0.45012	0.224099
35	1	-1.23044	-2.11119	-1.04806
36	1	1.23	-2.11136	-1.0481
37	1	1.236269	7.223257	0.708381
38	1	-1.23504	7.223505	0.708412
39	1	-2.47141	5.120512	0.312647
40	1	-3.2906	0.798948	-0.50083
41	1	3.290484	0.798612	-0.50089
42	1	2.885593	-2.12182	-0.53692
43	1	3.651097	-1.42881	-1.94645
44	1	5.422929	-0.47568	-0.5156
45	1	4.657468	-1.16874	0.893944
46	1	4.976413	-3.42983	-0.04462
47	1	5.741827	-2.73677	-1.45418
48	1	-3.65129	-1.42849	-1.94639

49	1	-2.88579	-2.1215	-0.53684
50	1	-4.65769	-1.16841	0.893995
51	1	-5.42315	-0.4754	-0.51557
52	1	-5.74194	-2.73654	-1.45412
53	1	-4.97653	-3.42953	-0.04452
54	1	2.472199	5.120015	0.312581

15AQS

Center Number	Atomic Number	Coordinates (Angstroms)		
		X	Y	Z
1	6	2.951918	2.355145	-6.5E-05
2	6	3.570236	1.121171	0.000031
3	6	2.824529	-0.06007	0.000029
4	6	1.438668	0.006012	-4.1E-05
5	6	0.767385	1.251106	-0.00011
6	6	1.539215	2.459416	-0.00016
7	6	0.690604	-1.28735	-6.3E-05
8	6	-0.76739	-1.25111	-0.00011
9	6	-1.43867	-0.00601	-4.1E-05
10	6	-0.6906	1.287354	-6.3E-05
11	6	-1.53922	-2.45942	-0.00016
12	6	-2.95192	-2.35515	-6.5E-05
13	6	-3.57024	-1.12117	0.000031
14	6	-2.82453	0.060071	0.000029
15	8	-1.33053	2.349828	-8.2E-05
16	8	1.330529	-2.34983	-8.2E-05
17	7	0.936576	3.670982	-0.00034
18	7	-0.93658	-3.67098	-0.00034
19	6	-1.62526	-4.94598	-0.00013

20	6	-0.5963	-6.0733	-4.6E-05
21	6	-1.24678	-7.44877	0.000155
22	16	-0.02365	-8.78566	0.000151
23	8	-0.76739	-10.0444	0.000339
24	8	0.844704	-8.54598	-1.21757
25	8	0.844999	-8.54583	1.217611
26	6	1.625258	4.945977	-0.00013
27	6	0.596297	6.073302	-4.6E-05
28	6	1.24678	7.448774	0.000155
29	16	0.023652	8.785656	0.000151
30	8	0.767385	10.04435	0.000339
31	8	-0.8447	8.545983	-1.21757
32	8	-0.845	8.545831	1.217611
33	11	-2.6847	8.289875	0.000009
34	11	2.6847	-8.28988	0.000009
35	1	3.550914	3.255325	-0.00011
36	1	4.653388	1.072433	0.000102
37	1	3.300026	-1.03047	0.000064
38	1	-3.55091	-3.25533	-0.00011
39	1	-4.65339	-1.07243	0.000102
40	1	-3.30003	1.03047	0.000064
41	1	-0.07934	3.64226	-0.00037
42	1	0.079335	-3.64226	-0.00037
43	1	-2.2721	-5.03163	0.882968
44	1	-2.27221	-5.03187	-0.88313
45	1	0.04013	-5.97871	-0.8845
46	1	0.04023	-5.97849	0.884317
47	1	-1.85777	-7.62006	0.888193

48	1	-1.85793	-7.62025	-0.88774
49	1	2.272101	5.031631	0.882968
50	1	2.272206	5.031867	-0.88313
51	1	-0.04013	5.97871	-0.8845
52	1	-0.04023	5.978488	0.884317
53	1	1.857766	7.62006	0.888193
54	1	1.857927	7.620245	-0.88774

26AQS

Center Number	Atomic Number	Coordinates (Angstroms)		
		X	Y	Z
1	6	-3.76836	0.215342	-0.26198
2	6	-3.42364	1.583042	-0.19236
3	6	-2.09465	1.964772	-0.14043
4	6	-1.06315	1.020097	-0.1529
5	6	-1.40434	-0.34742	-0.22
6	6	-2.7314	-0.73676	-0.2734
7	6	0.337665	1.468538	-0.09447
8	6	1.392741	0.406131	-0.11791
9	6	1.051804	-0.96131	-0.18432
10	6	-0.34963	-1.41019	-0.23342
11	6	2.720289	0.79554	-0.07341
12	6	3.757281	-0.15581	-0.09483
13	6	3.412703	-1.52288	-0.16763
14	6	2.083318	-1.90544	-0.20823
15	8	-0.65382	-2.59597	-0.28315
16	8	0.642017	2.653655	-0.03053
17	7	-5.07173	-0.19746	-0.32866
18	7	5.062291	0.260095	-0.02492

19	6	6.201614	-0.61713	-0.21964
20	6	7.5019	0.171179	-0.09174
21	6	8.718037	-0.72525	-0.28813
22	16	10.26093	0.209696	-0.13909
23	8	11.37193	-0.80144	-0.31488
24	8	10.21992	1.273564	-1.1447
25	8	10.31878	0.692921	1.295929
26	6	-6.21596	0.683136	-0.19544
27	6	-7.51089	-0.12258	-0.24579
28	6	-8.73277	0.778243	-0.11687
29	16	-10.2677	-0.18114	-0.14238
30	8	-11.3834	0.824919	0.032368
31	8	-10.2912	-0.92753	-1.4019
32	8	-10.2409	-1.04058	1.105692
33	1	-4.19743	2.339025	-0.18189
34	1	-1.826	3.012633	-0.08785
35	1	4.186319	-2.2785	-0.19489
36	1	1.814834	-2.95315	-0.26438
37	1	-5.2429	-1.18888	-0.27554
38	1	5.226054	1.246733	-0.15268
39	1	6.177717	-1.41109	0.535926
40	1	6.15475	-1.10749	-1.20327
41	1	7.52895	0.970402	-0.83819
42	1	7.552561	0.640322	0.894301
43	1	8.77022	-1.52128	0.456566
44	1	8.747755	-1.16855	-1.2852
45	1	-6.16053	1.24243	0.749643
46	1	-6.20915	1.422344	-1.00619

47	1	-7.56979	-0.67295	-1.1882
48	1	-7.52182	-0.85618	0.566017
49	1	-8.7386	1.337172	0.820423
50	1	-8.81828	1.478812	-0.94953
51	1	2.942979	1.855202	-0.019
52	1	-2.95404	-1.79652	-0.32609
53	11	-12.1765	-0.22109	1.829893
54	11	12.28088	-0.28888	1.6515

27AQS

Center Number	Atomic Number	Coordinates (Angstroms)		
		X	Y	Z
1	6	-3.6925	3.320677	-0.06615
2	6	-3.90683	1.932541	0.099887
3	6	-2.78711	1.087717	0.149219
4	6	-1.50117	1.610276	0.040947
5	6	-1.29438	2.990243	-0.12196
6	6	-2.41596	3.83047	-0.17407
7	6	-0.34955	0.663682	0.097896
8	6	1.019087	1.247926	-0.00794
9	6	1.203705	2.635944	-0.16759
10	6	0.060559	3.572204	-0.23835
11	6	2.109511	0.394103	0.054828
12	6	3.422594	0.889233	-0.03618
13	6	3.603548	2.279959	-0.18904
14	6	2.508514	3.126072	-0.25537
15	8	0.228388	4.779262	-0.38582
16	8	-0.51996	-0.53903	0.22664
17	7	-5.18291	1.447273	0.223635

18	7	4.483888	0.016848	0.001154
19	6	5.865857	0.442446	0.126848
20	6	6.788511	-0.772	0.175047
21	6	8.248382	-0.35766	0.310249
22	16	9.343567	-1.79785	0.365249
23	8	10.74653	-1.24242	0.468979
24	8	8.914019	-2.62411	1.495634
25	8	9.225433	-2.46433	-0.99051
26	6	-5.50808	0.032943	0.244953
27	6	-7.02116	-0.15841	0.285989
28	6	-7.39498	-1.63392	0.351122
29	16	-9.19008	-1.86305	0.313032
30	8	-9.41447	-3.35769	0.368688
31	8	-9.74881	-1.10498	1.43443
32	8	-9.63925	-1.39421	-1.05696
33	1	-2.88939	0.018872	0.272818
34	1	4.600727	2.694464	-0.25333
35	1	2.644651	4.193996	-0.37312
36	1	-5.93685	2.085731	0.025821
37	1	4.277003	-0.91934	0.313878
38	1	6.128116	1.068109	-0.73403
39	1	6.007876	1.058541	1.027478
40	1	6.523467	-1.40887	1.024146
41	1	6.661955	-1.36639	-0.73351
42	1	8.585854	0.250468	-0.53075
43	1	8.43998	0.182646	1.239173
44	1	-5.09039	-0.47155	-0.63809
45	1	-5.05004	-0.43328	1.125372

46	1	-7.43832	0.354913	1.155949
47	1	-7.47373	0.28437	-0.60677
48	1	-6.99846	-2.1997	-0.49362
49	1	-7.06351	-2.10245	1.279453
50	1	1.927147	-0.66791	0.173799
51	1	-2.25176	4.893223	-0.3009
52	11	-10.567	-3.35779	-1.53293
53	11	11.41202	-2.31527	-1.36398
54	1	-4.54866	3.986625	-0.10442

Table. S3 XYZ Coordinates of the optimized structures for various AQs, used for calculating molecular orbital energies, electrostatic potential (ESP), and Fukui functions calculations.

	Power Density (W cm^{-2})	EE (%) (x mA cm^{-2})	Cycle Life	Solubility (M)	Voltage (V)	fade rate
This work	**0.342**	**80 (100)**	**1000**	**1.6 (H_2O)** **0.99 (1 M NaOH)**	**-0.85 (Ag/AgCl)**	**0.03 % day^{-1}**
2,6-DBEAQ[17]	0.24	80 (100)	350	0.6 (pH 12)	-0.515 (SHE)	0.04% day^{-1}
2,6-DHAQ[18]	0.45	84 (100)	100	0.6 (1 M KOH)	-0.67 (SHE)	0.1% $cycle^{-1}$
AQ-1,8-3E-OH[19]	0.22	85 (50)	250	2.24 (H_2O)	-0.43 (SHE)	0.5% day^{-1}
2,6-DPPEAQ[20]	0.16	65 (100)	460	0.75 (pH 9)	-0.49 (SHE)	0.00036% $cycle^{-1}$ 0.014% day^{-1}
$AQDS(NH_4)_2$[21]	0.092	70 (60)	300	1.9 (H_2O)	-0.2 (NHE)	0
1,6-DPAP[22]	0.103	83 (20)	90	1 (H_2O)	-0.56 (SHE)	0.000002% $cycle^{-1}$ 0.0015% day^{-1}
Lawsone[23]		74 (10)	260		-0.7 (Ag/AgCl)	0.0079% $cycle^{-1}$
PEG12-AQ[24]	0.12		180		-0.64 (Ag/AgCl)	0.02% $cycle^{-1}$
DAEAQ[25]	0.34	81 (100)	500	0.99 (1 M KOH)	-0.62 (SHE)	0.24% day^{-1}
1-DPAQCl[26]	0.134	50 (100)	100	1.44 (H_2O)	-0.7 (Ag/AgCl)	
1,8-BDPAQCl2[27]	0.042	45 (100)	200	1.07 (H_2O)	-0.55 (NHE)	0.048% $cycle^{-1}$ 0.88% day^{-1}
2,6-D2PEAQ[28]	0.16	70 (100)	200	2.0 (pH 7)	-0.445 (SHE)	0.02% day^{-1}
Cys-AE[29]	0.215	80 (100)	812	0.78 (1 M KOH)	-0.51 (SHE)	0.0130% day^{-1}
1,2-DHAQ-2[30]	0.066	72 (40)	19 (day)		-0.66 (SHE)	0.73% day^{-1}
2,6-N-TSAQ[31]	0.18	85 (40)	900	0.45 (H_2O) 0.4 (1 M NaOH)	-0.62 (SHE)	0.00024% $cycle^{-1}$ 0.025% day^{-1}
1,4-BDEAQCl2[32]	0.006	84 (10)	100	1.2 (H_2O)	-0.554 (SHE)	
Cys-DHAQ[33]	0.29	83 (100)	890	0.63 (1 M KOH)	-0.692 (Ag/AgCl)	0.00025% $cycle^{-1}$ 0.011% day^{-1}
1,8-DHAQDS[34]	0.29		100		-0.175 (Ag/AgCl)	

Table. S6 performance comparison of **15AQS** in this work with other representative anthraquinone derivatives for AORFBs from the previous literature.

References

[1] Perry, P. J., Reszka, A. P., Wood, A. A., Read, M. A., Gowan, S. M., Dosanjh, H. S., Trent, J. O., Jenkins, T. C., Kelland, L. R., Neidle, S. Human Telomerase Inhibition by Regioisomeric Disubstituted Amidoanthracene-9,10-diones. *J. Med. Chem.* **1998**, *41*, 4873–4884.

[2] Frisch, M. J.; Trucks, G. W.; Schlegel, H. B.; Scuseria, G. E.; Robb, M. A.; Cheeseman, J. R.; Scalmani, G.; Barone, V.; Mennucci, B.; Petersson, G. A.; Nakatsuji, H.; Caricato, M.; Li, X.; Hratchian, H. P.; Izmaylov, A. F.; Bloino, J.; Zheng, G.; Sonnenberg, J. L.; Hada, M.; Ehara, M.; Toyota, K.; Fukuda, R.; Hasegawa, J.; Ishida, M.; Nakajima, T.; Honda, Y.; Kitao, O.; Nakai, H.; Vreven, T.; Montgomery, J. A.; Peralta, J. J. E.; Ogliaro, F.; Bearpark, M.; Heyd, J. J.; Brothers, E.; Kudin, K. N.; Taroverov, V. N.; Keith, T.; Kobayashi, R.; Normand, J.; Raghavachari, K.; Rendell, A.; Burant, J. C.; Iyengar, S. S.; Tomasi, J.; Cossi, M.; Rega, N.; Millam, J. M.; Klene, M.; Knox, J. E.; Cross, J. B.; Bakken, V.; Adamo, C.; Jaramillo, J.; Gomperts, R.; Stratmann, R. E.; Yazyev, O.; Austin, A. J.; Cammi, R.; Pomelli, C.; Ochterski, J. W.; Martin, R. L.; Morokuma, K.; Zakrzewski, V. G.; Voth, G. A.; Salvador, P.; Dannenberg, J. J.; Dapprich, S.; Daniels, A. D.; Farkas, O.; Foresman, J. B.; Ortiz, J. V.; Cioslowski, J.; Fox, D. J. Gaussian, Inc., Wallingford CT, **2019**.

[3] Krishnan, R.; Binkley, J. S.; Seeger, R.; Pople, J. A. Self - consistent molecular orbital methods. XX. A basis set for correlated wave functions. *J. Chem. Phys.* **1980**, *72*, 650–654.

[4] Weigend, F.; Ahlrichs, R. Balanced basis sets of split valence, triple zeta valence and quadruple zeta valence quality for H to Rn: Design and assessment of accuracy. *Phys. Chem. Chem. Phys.* **2005**, *7*, 3297–3305.

[5] Xu, S.; He, T.; Li, J.; Huang, Z.; Hu, C. Enantioselective synthesis of D-lactic acid via chemocatalysis using MgO: Experimental and molecular-based rationalization of the triose's reactivity and preliminary insights with raw biomass. *Appl. Catal. B: Environ.* **2021**, *292*, 120145.

[6] Wadt, W. R.; Hay, P. J. Ab initio effective core potentials for molecular calculations. Potentials for main group elements Na to Bi. *J. Chem. Phys.* **1985**, *82*, 284–298.

[7] Hay, P. J.; Wadt, W. R. Ab initio effective core potentials for molecular calculations. Potentials for the transition metal atoms Sc to Hg. *J. Chem. Phys.* **1985**, *82*, 270–283.

[8] Hay, P. J.; Wadt, W. R. Ab initio effective core potentials for molecular calculations. Potentials for K to Au including the outermost core orbitals. *J. Chem. Phys.* **1985**, *82*, 299–310.

[9] Martínez, L.; Andrade, R.; Birgin, E. G.; Martínez, J. M. PACKMOL: A package for building initial configurations for molecular dynamics simulations. *J. Comput. Chem.* **2009**, *30*, 2157–2164.

[10] Marenich, A. V.; Cramer, C. J.; Truhlar, D. G. Performance of SM6, SM8, and SMD on the SAMPL1 Test Set for the Prediction of Small-Molecule Solvation Free Energies. *J. Phys. Chem. B* **2009**, *113*, 4538–4543.

[11] Jorgensen, W. L.; Maxwell, D. S.; Tirado-Rives, J. Development and Testing of the OPLS All-Atom Force Field on Conformational Energetics and Properties of Organic Liquids. *J. Am. Chem. Soc.* **1996**, *118*, 11225–11236.

[12] Kaminski, G. A.; Friesner, R. A.; Tirado-Rives, J.; Jorgensen, W. L. Evaluation and Reparametrization of the OPLS-AA Force Field for Proteins via Comparison with Accurate Quantum Chemical Calculations on Peptides. *J. Phys. Chem. B* **2001**, *105*, 6474–6487.

[13] Robertson, M. J.; Qian, Y.; Robinson, M. C.; Tirado-Rives, J.; Jorgensen, W. L. Development and Testing of the OPLS-AA/M Force Field for RNA. *J. Chem. Theory Comput.* **2019**, *15*, 2734–2742.

[14] Wang, C.; Li, W.; Liao, K.; Wang, Z.; Wang, Y.; Gong, K. AuToFF Program, Vesrion 1.0. Hzwtech. Shanghai **2023**, see https://cloud.hzwtech.com/web/product-service?id=36.

[15] Abraham, M. J.; Murtola, T.; Schulz, R.; Páll, S.; Smith, J. C.; Hess, B.; Lindahl, E. GROMACS: High performance molecular simulations through multi-level parallelism from laptops to supercomputers. *SoftwareX* **2015**, *1–2*, 19–25.

[16] Humphrey, W.; Dalke, A.; Schulten, K. VMD: Visual molecular dynamics. *J. Mol. Graph.* **1996**, *14*, 33–38.

[17] Kwabi, D. G.; Lin, K.; Ji, Y.; Kerr, E. F.; Goulet, M.-A.; De Porcellinis, D.; Tabor, D. P.; Pollack, D. A.; Aspuru-Guzik, A.; Gordon, R. G.; Aziz, M. J. Alkaline Quinone Flow Battery with Long Lifetime at pH 12. *Joule* **2018**, *2*, 1894–1906.

[18] Lin, K.; Chen, Q.; Gerhardt, M. R.; Tong, L.; Kim, S. B.; Eisenach, L.; Valle, A. W.; Hardee, D.; Gordon, R. G.; Aziz, M. J.; Marshak, M. P. Alkaline quinone flow battery. *Science* **2015**, *349*, 1529–1532.

[19] Jin, S.; Jing, Y.; Kwabi, D. G.; Ji, Y.; Tong, L.; De Porcellinis, D.; Goulet, M.-A.; Pollack, D. A.; Gordon, R. G.; Aziz, M. J. A Water-Miscible Quinone Flow Battery with High Volumetric Capacity and Energy Density. *ACS Energy Lett.* **2019**, *4*, 1342–1348.

[20] Ji, Y.; Goulet, M.-A.; Pollack, D. A.; Kwabi, D. G.; Jin, S.; De Porcellinis, D.; Kerr, E. F.; Gordon, R. G.; Aziz, M. J. A Phosphonate-Functionalized Quinone Redox Flow Battery at Near-Neutral pH with Record Capacity Retention Rate. *Adv. Energy Mater.* **2019**, *9*, 1900039.

[21] Hu, B.; Luo, J.; Hu, M.; Yuan, B.; Liu, T. L. A pH-Neutral, Metal-Free Aqueous Organic Redox Flow Battery Employing an Ammonium Anthraquinone Anolyte. *Angew. Chem. Int. Ed.* **2019**, *58*, 16629–16636.

[22] Pang, S.; Wang, X.; Wang, P.; Ji, Y. Biomimetic Amino Acid Functionalized Phenazine Flow Batteries with Long Lifetime at Near-Neutral pH. *Angew. Chem. Int. Ed.* **2021**, *60*, 5289–5298.

[23] Hu, P.; Lan, H.; Wang, X.; Yang, Y.; Liu, X.; Wang, H.; Guo, L. Renewable-lawsone-based sustainable and high-voltage aqueous flow battery. *Energy Storage Mater.* **2019**, *19*, 62–68.

[24] Chai, J.; Wang, X.; Lashgari, A.; Williams, C. K.; Jiang, J. A pH-Neutral, Aqueous Redox Flow Battery with a 3600-Cycle Lifetime: Micellization-Enabled High Stability and Crossover Suppression. *ChemSusChem* **2020**, *13*, 4069–4077.

[25] Wang, C.; Yu, B.; Liu, Y.; Wang, H.; Zhang, Z.; Xie, C.; Li, X.; Zhang, H.; Jin, Z. N-alkyl-carboxylate-functionalized anthraquinone for long-cycling aqueous redox flow batteries. *Energy Storage Mater.* **2021**, *36*, 417–426.

[26] Xia, L.; Huo, W.; Gao, H.; Zhang, H.; Chu, F.; Liu, H.; Tan, Z. Intramolecular hydrogen bonds induced high solubility for efficient and stable anthraquinone based neutral aqueous organic redox flow batteries. *J. Power Sources* **2021**, *498*, 229896.

[27] Xia, L.; Zhang, Y.; Wang, F.; Chu, F.; Yang, Y.; Li, H.; Tan, Z. A Low-Potential and Stable Bis-Dimethylamino-Substituted Anthraquinone for pH-Neutral Aqueous Redox Flow Batteries. *ChemElectroChem* **2022**, *9*, e202200224.

[28] Kerr, E. F.; Tang, Z.; George, T. Y.; Jin, S.; Fell, E. M.; Amini, K.; Jing, Y.; Wu, M.; Gordon, R. G.; Aziz, M. J. High Energy Density Aqueous Flow Battery Utilizing Extremely Stable, Branching-Induced High-Solubility Anthraquinone near Neutral pH. *ACS Energy Lett.* **2023**, *8*, 600–607.

[29] Liu, Y.; Wu, Z.; Zhang, P.; Wei, J.; Li, J.; Wang, H.; Wen, S.; Liang, J.; Chen, Y.; Dai, T.; Tie, Z.; Ma, J.; Wang, X.; Jin, Z. Artificial α-amino acid based on cysteine grafted natural aloe-emodin for aqueous organic redox flow batteries. *Nat. Commun.* **2025**, *16*, 2965.

[30] Maleki, M.; Imhanria, S.; Duguet, L.; Goulet, M.-A. Stability of Alizarin as a Low-Cost Anthraquinone for Aqueous Redox Flow Batteries. *J. Electrochem. Soc.* **2024**, *171*, 120537.

[31] Wu, M.; Bahari, M.; Jing, Y.; Amini, K.; Fell, E. M.; George, T. Y.; Gordon, R. G.; Aziz, M. J. Highly Stable, Low Redox Potential Quinone for Aqueous Flow Batteries. *Batter. Supercaps* **2022**, *5*, e202200009.

[32] Xu, L.; Wang, Q.; Guo, D.; Xu, J.; Cao, J. A quaternized anthraquinone derivative for pH-neutral aqueous organic redox flow batteries. *New J. Chem.* **2023**, *47*, 11216–11221.

[33] Zhang, P.; Liu, Y.; Wei, J.; Wu, Z.; Song, X.; Ding, G.; Wang, H.; Liang, J.; Tie, Z.; Jin, Z. An amphoteric and hydrogen-bond-rich artificial α-amino acid for highly durable aqueous redox flow batteries. *Nat. Commun.* **2025**, *16*, 4727.

[34] Lantz, A. W.; Shavalier, S. A.; Schroeder, W.; Rasmussen, P. G. Evaluation of an Aqueous Biphenol- and Anthraquinone-Based Electrolyte Redox Flow Battery. *ACS Appl. Energy Mater.* **2019**, *2*, 7893–7902.